University of Tromsø – The Arctic University of Norway
Department of Geology

Experimental investigation on the fabric evolution and strain localization of quartz with and without the presence of muscovite

—

Leif Tokle
Master thesis in Geology GEO-3900
May 2014

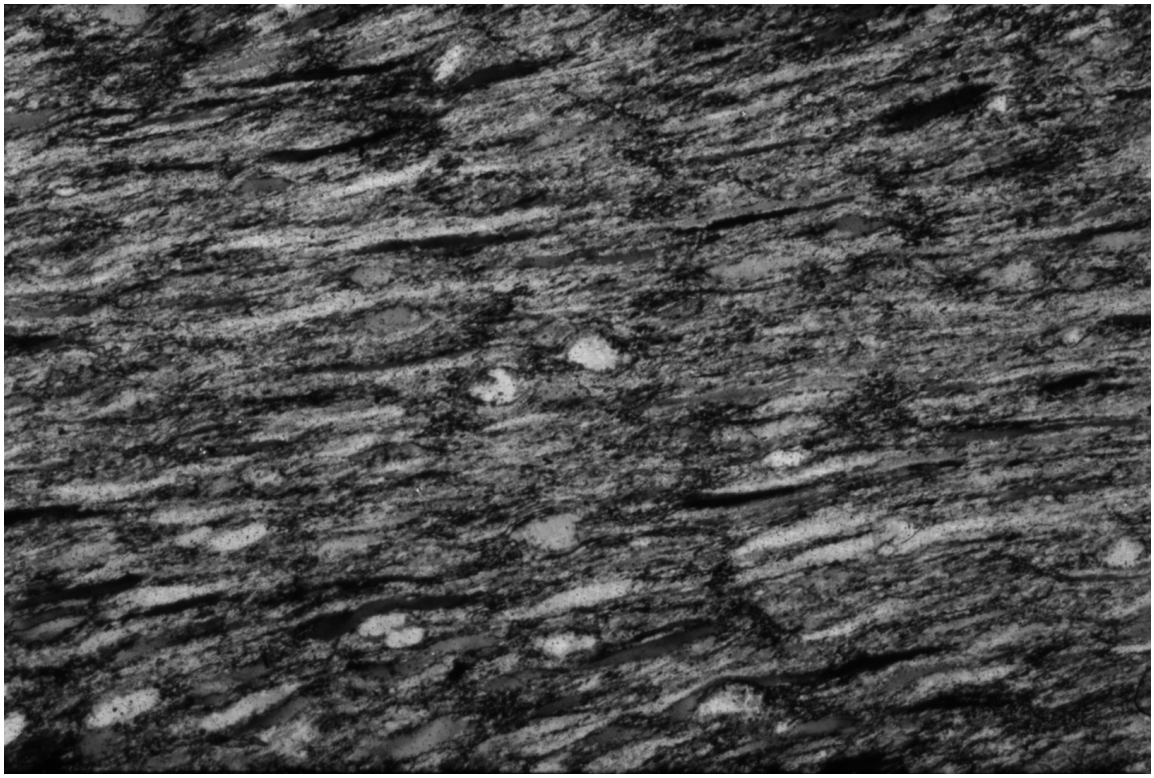

Acknowledgements
Working on these two projects has been a real enjoyment and thought provoking experience. I would firstly like to thank my advisor Holger Stünitz for his guidance during my time here in Tromsø as well as Greg Hirth for his assistance and insightful discussions.

Renee Heilbronner, Rüdiger Kilian, Sina Marti, Bettina Richter, and Lars Hansen have been extremely helpful with insightful discussions as well as assistance with various problems along the way. Thank You!

I would like to thank Willy Tschudin for processing all of the thin sections used in this thesis.

Finally, I would like to thank Tore Forthun and Holly Abbandonato for reading over my thesis and providing useful comments and edits.

Abstract
Deformation experiments of synthetic quartz–muscovite aggregates were performed to high shear strains at dislocation creep conditions in quartz. In previous studies, axial compression experiments were conducted on quartz aggregates to develop a better understanding of the relationship between flow strength and lattice preferred orientation with varying percentages of muscovite. Other analyses have shown a relationship between the topology of second phases and the aggregate strength of the material. When the second phase exceeds a threshold percent within the aggregate, it becomes the mechanically controlling phase. In the case of muscovite in a quartzite, when the muscovite becomes abundant enough to develop an interconnected framework throughout the aggregate it becomes the controlling phase of the aggregate. This study demonstrates that at a volume percent between 10% and 25% muscovite there is a mechanical transition between a quartz-dominanted and muscovite-dominanted aggregate. The development of C' shear bands in muscovite-present aggregates are interpreted as a weakening mechansim and aid in the redistribution of muscovite through processes such as dissolution–precipitation and recrystallization. In 100% quartz aggregates, strain localization is observed through geometrical softening where at the onset of recrystallization, c-axis orientations transition from prism [c] to rhomb <a>. Localization of strain is intrepreted as an increase in strain rate in the highest strained regions, which is consistent with the theory of the paleowattmeter where the recrystallized grain size is dependent on both stress and strain rate.

Keywords: Shear zone; Strain localization; Quartz; Muscovite

Content

CHAPTER 1: Introduction to shear zones

1.1 General aspects of shear zones

Ductile shear zones are the result of strain localization over a variety of P, T, $\dot{\varepsilon}$ conditions and a wide range of length scales (Ramsay 1980; White et al. 1980). Ductile shear zones, or shear zones are high strain structures within the Earth that provide physical evidence for processes that can lead to the transport of large rock masses over great distances, e.g. plate tectonics.

For these reasons the development of shear zones has been extensively studied. Natural and experimental studies of earth materials have provided evidence for mechanisms such as (1) grain size reduction (Braun et al 1999; Montesi and Hirth 2003, Précigout and Gueydan 2009), (2) crystallographic preferred orientation (CPO) (Poirier 1980, White et al. 1980, Tommasi et al 2009, Muto et al. 2011), (3) shear heating (Kameyama et al 1999, Kelemen and Hirth 2007,and Ogawa 1987), (4) phase mixing

(Linenkins et al. 2014 and Warren and Hirth 2006), and (5) the interconnection of the weak phase (Jordan 1987, 1988; Handy 1990, 1994, Tullis and Wenk 1994) to contribute to the development of shear zones and strain localization. While there have been many mechanisms proposed to contribute to the development of shear zones, we have chosen to focus our work on both the interconnection of the weak phase and the evolution of strain distribution in the setting of quartz-rich aggregates. Recent studies have demonstrated the importance of strain localization in micaceous-rich rocks at the meter- and kilometer-scale within the crust (Johnson et al. 2004, Gerbi et al. 2010). Understanding the mechanisms that localize strain and weaken rocks aggregates at the grain-scale will provide valuable insight into how weaker rocks influence large-scale tectonic processes.

Quartz is one of the most abundant minerals in the continental crust and is often found in many rock types. Quartz has been extensively studied in both natural and experimental settings, where experimental data on "wet quartz" is often modeled as the strength envelope of the continental crust (Bürgman and Dresen 2008; Rutter and Brodie 2004a,b). The mechanical behavior of quartz under various geologic conditions has been investigated but little work has been conducted on how secondary minerals affect the ductile deformation of quartz at continental crust conditions. One such secondary mineral is muscovite; muscovite is one of the most common secondary minerals found in association with quartz in the continental crust. Tullis and Wenk (1994) conducted coaxial deformation studies with different volume percentages of quartz and muscovite. Holyoke and Tullis (2006) performed shear experiments on natural gneiss, investigating mechanisms, which lead to the connectivity of weak phases, e.g. muscovite and biotite. Questions still remain, such as, how does muscovite affect quartz deformation at high shear strains? What effect does the volume percent of muscovite have on the CPO and SPO development of quartz at high strains? And, what effect does muscovite have on quartz recrystallization? Chapter 2 of this thesis examines the role muscovite plays in shear deformation of a quartz-rich aggregate at continental crust conditions.

The construction of end-member models for the development of shear zones and their use as recorders of the deformation history can be a useful tool in determining boundary conditions for weakening processes in a wide range of deformation scenarios. Hull (1988) proposed three end-member scenarios: where the thickness of the shear

zone grows over time (Type 1), the thickness of the shear zone decreases over time (Type 2), and the thickness of the shear remains the same over time (Type 3), figure 1.1. Means (1995) considers only Type 1 and Type 2. Changing the thickness of the shear zone over time will affect various kinematic parameters recorded in the microstructures. As illustrated in figure 1.1, the black line running through the cross-section of the top horizontal column represents the strain gradient throughout the shear zone. The thickness of the shear zone has an effect on the development of strain over time depending on whether the zone is increasing or decreasing. Ingles (1983; 1985) provide a theoretical approach to understanding the change in strain across a shear zone. If certain parameters are assumed, such as displacement rate of the shear zone, finite-strain trajectories can be constructed which allow the use of strain markers and passive markers to determine the evolution of structures in shear zones.

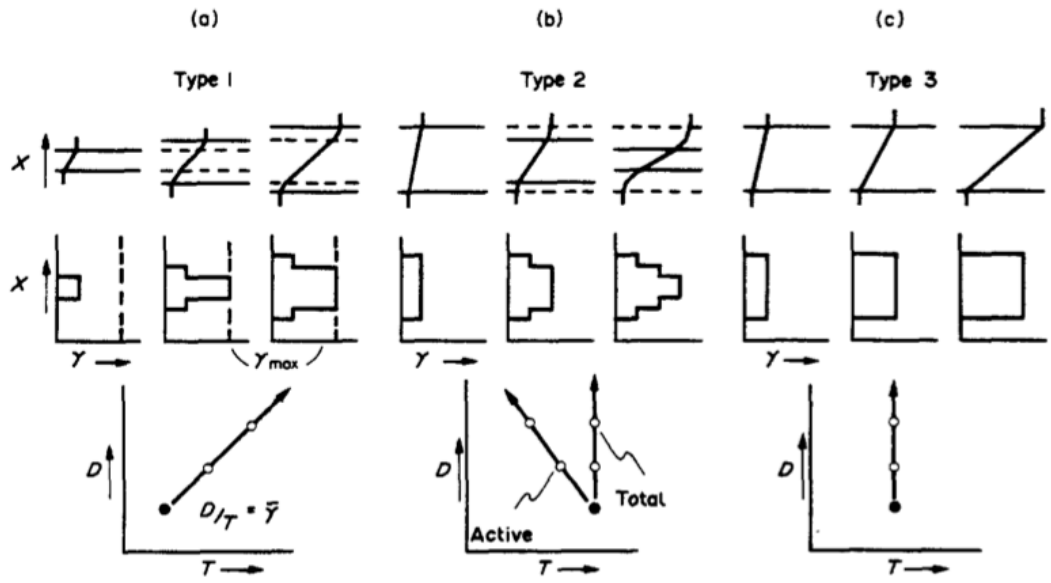

Figure 1.1. Schematic models describing end-member cases for the development of a shear zone over time. The top illustrations describe the thickness of the zone, the central illustrations describe the shear strain across the active and total zone, and the bottom illustration describes the displacement vs. time. (a) Type 1 where the thickness of the shear zone increases over time (b) Type 2 where the thickness of the shear zone decreases over time and (c) type 3 where the thickness of the shear zone remains the same over time (after figure 4 Hull 1988).

The stabilized or equilibrium grain size of minerals has become a parameter used to determine conditions of deformation through the recrystallized grain-size piezometer. Twiss (1977) proposed a relationship between the flow stress of a material and the recrystallized grain size observed in the same material. Equation 1 describes

this relationship that can be observed in many metals and ceramics as well as many different earth materials, where d is the recrystallized grain size, B is a constant, σ is the flow stress, and k (equation 2) is a value based on the ratio of total dislocation length in the boundary to the dislocation length within the grain interior, where ϕ is assumed to be ≥1 for grain boundaries to form (Twiss 1977).

$$d = B\sigma^{-k} \tag{1}$$

$$k = \frac{(2\phi - 1)}{\phi} \tag{2}$$

Stipp and Tullis (2003) used this theory to experimentally produce a recrystallized grain size piezometer for quartz at dislocation creep conditions. The results from this study allow for the approximate determination of flow stress in deforming quartz aggregates. In addition, the piezometer produced by Stipp and Tullis (2003) provides an approximate relationship in regards to the different quartz recrystallization mechanisms proposed by Hirth and Tullis (1992), figure 1.2.

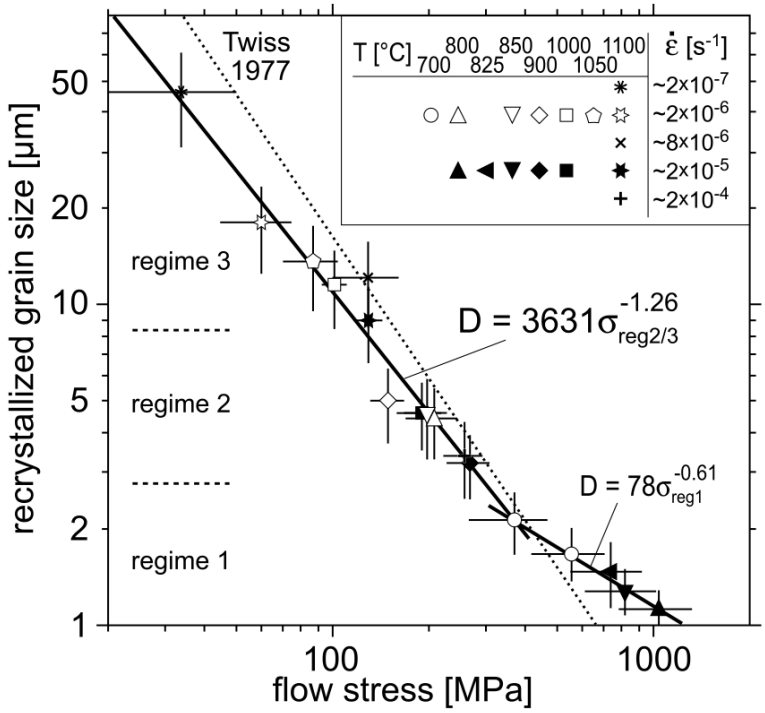

Figure 1.2. The least squares fit calibrations for the recrystallized grain size piezometer for quartz. Twiss 1977 flow is plotted as a dashed line using a shear modulus of 42 GPa, a Poisson ratio of 0.15 and a Burgers vector of 5 x 10^{-4} μm. The experiments performed in this study were conducted at a confining pressure of 1.5GPa (after figure 4 Stipp and Tullis 2003).

Austin and Evans (2007; 2009) proposed the paleowattmeter, which is a relationship, where the rate of grain size reduction is controlled by the dissipation rate of mechanical work per volume in the system, equation 3.

$$\dot{W} = \sigma\dot{\varepsilon} \qquad (3)$$

This relationship differs from the recrystallized grain size piezometer in that the paleowattmeter is dependent on both, flow stress of the system as well as the strain rate, whereas the piezometer is only stress dependent. For a more in-depth review of grain size evolution and the construction of the paleowattmeter see Austin and Evans (2009).

Using the paleowattermeter as a reference frame we propose to demonstrate end-member models for the development of strain localization in shear zones. This is presented in chapter 3 of this thesis.

1.2 Natural shear zones

Natural shear zones provide a snapshot into the deformation occurring at depth within the earth. Factors such as crystallographic preferred orientation (CPO), shape preferred orientation (SPO), mineral assemblages, and others are used to characterize the possible deformation conditions such as strain, strain rate, stress, temperature, pressure, fluid, and the geometry of deformation that the rock experienced at depth. This type of analysis is referred to as a fabric or microfabric analysis (Schmid and Handy 1991). Early work on natural quartzites focused on relationships between the symmetry of mineral fabrics and the symmetry of deformation (Brethé et al. 1979, Bossière & Vauchez 1978, Bouchez (1977; 1978), Burg & Laurent 1978, Eisbacher 1970, Lister & Price 1978, Lunardi & Baker 1975). Pole figure diagrams are a method of presenting measurements of certain crystallographic directions for different types of materials. Schmid & Casey (1986) constructed schematic relationships between natural quartzite CPO and deformation geometries of simple and pure shear deformation, figure 1.3.

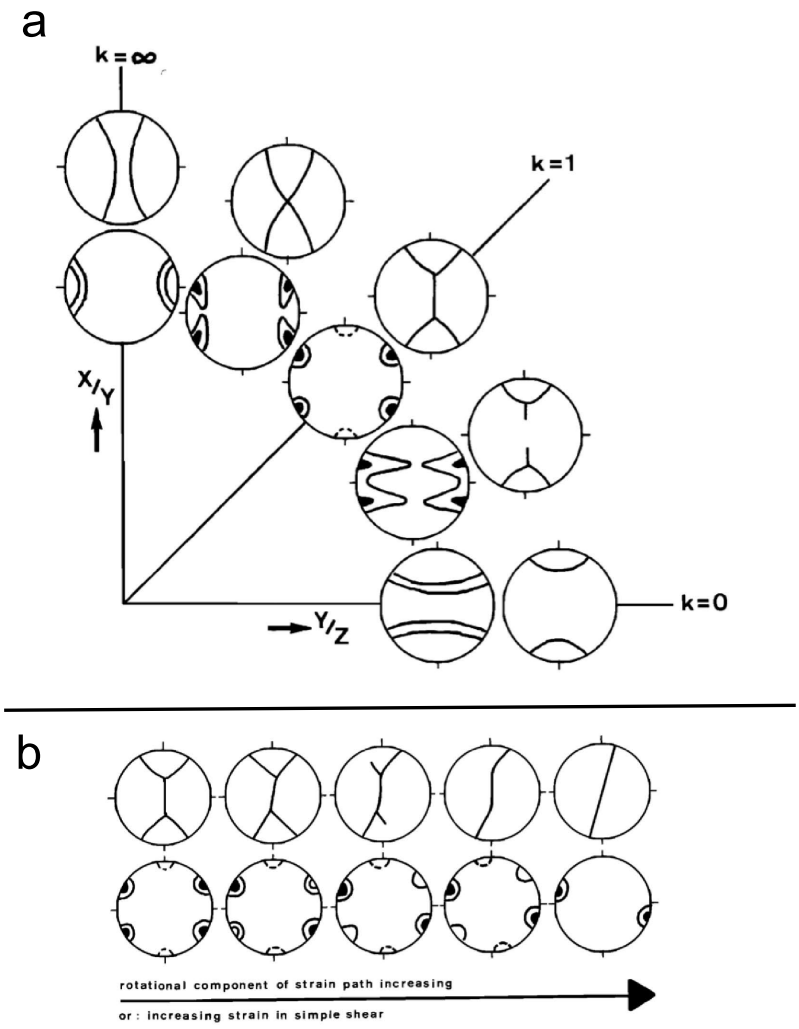

Figure 1.3 Commonly observed quartz CPOs; grey shaded regions represent c- axis domains while striped regions represent a-axis domains a) quartz pole figures plotted in a Flinn diagram depict c- and a-axis of quartz grains for coaxial deformation (after Schmid and Casey 1986; figure 15) b) quartz pole figures for increasing shear strain (modified after Schmid and Casey 1986; figure 14).

Many CPO analyses are typically conducted for monomineralic aggregates and, although it is fundamental in understanding the ideal CPO pattern for a particular material, natural observations demonstrate that most rocks are polymineralic (Herwegh et al. 2011). Several natural studies have provided evidence for heterogeneities in quartz CPO analyses, which lead to alterations of ideal monomineralic fabric patterns. These heterogeneities arise due to impurities within the rock, typically associated with phyllosilicates, feldspar clasts, pores, and initial arrangement of grains (Garcia Celma 1982, Hippertt 1994, Lisle 1985, Song & Ree 2007, Starkey & Cutforth 1977).

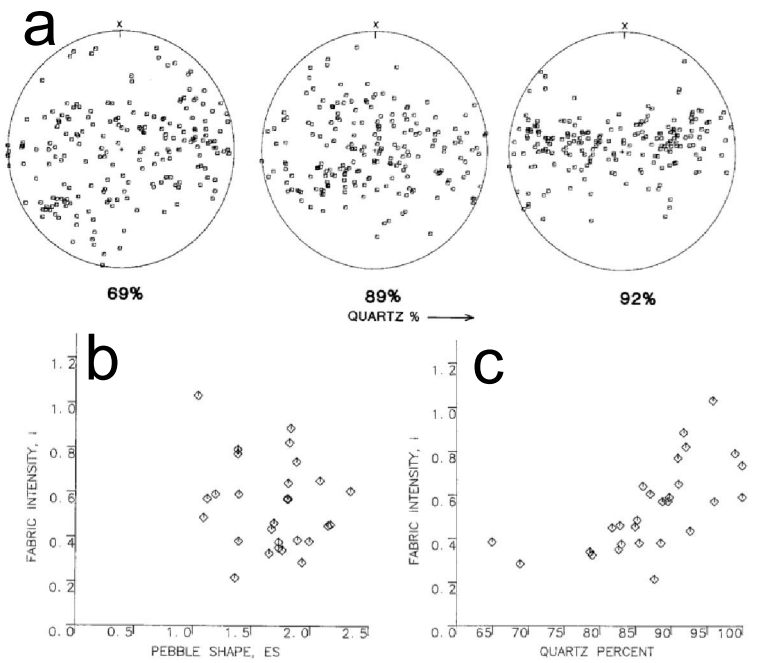

Figure 1.4 a) Three pole figures displaying the quartz c-axis orientations where the lower the percentage of quartz, the weaker the CPO (after Lisle 1985; figure 3) b) plot presenting the axial ratio of the individual clasts vs. the fabric intensity, no correlation found (after Lisle 1985; figure 4) c) plot presenting the quartz of quartz within individual clasts and the fabric intensity of each clast (modified after Lisle 1985; figure 5).

Phyllosilitcates, in particular, have been shown to alter the development of quartz CPO fabrics observed in nature (Lisle 1985). Phyllosilicates have been observed to pin quartz growth and rotational movement in quartz grains throughout deformation (Song & Ree 2007, Urai et al. 1986). Lisle (1985) measured the fabric intensity of different quartz clasts from a deformed conglomerate. This work demonstrated that with an increasing percentage of impurities within the clast, the CPO patterns became progressively less well defined and more randomly oriented (figure 1.4a,c). Lisle (1985) also plotted the axial ratio of quartz clasts vs. the fabric intensity and determined that there is no strict correlation between the shape of the individual clasts and their CPO (figure 1.4b). Starkey & Cutforth (1977) hypothesized that the presence of secondary minerals could change the deformation mechanism within quartz where grain boundary sliding and grain rotation would become the dominant mechanisms when secondary minerals are more abundant within the aggregate. Hippertt (1994) posits that there is a relationship between pore space in crystallographically orientated quartz grain boundaries that allow syn-deformational infiltration of fluids and subsequent muscovite precipitation into these pore spaces. This would allow for syn-deformation redistribution of muscovite throughout a deforming aggregate (figure 1.5).

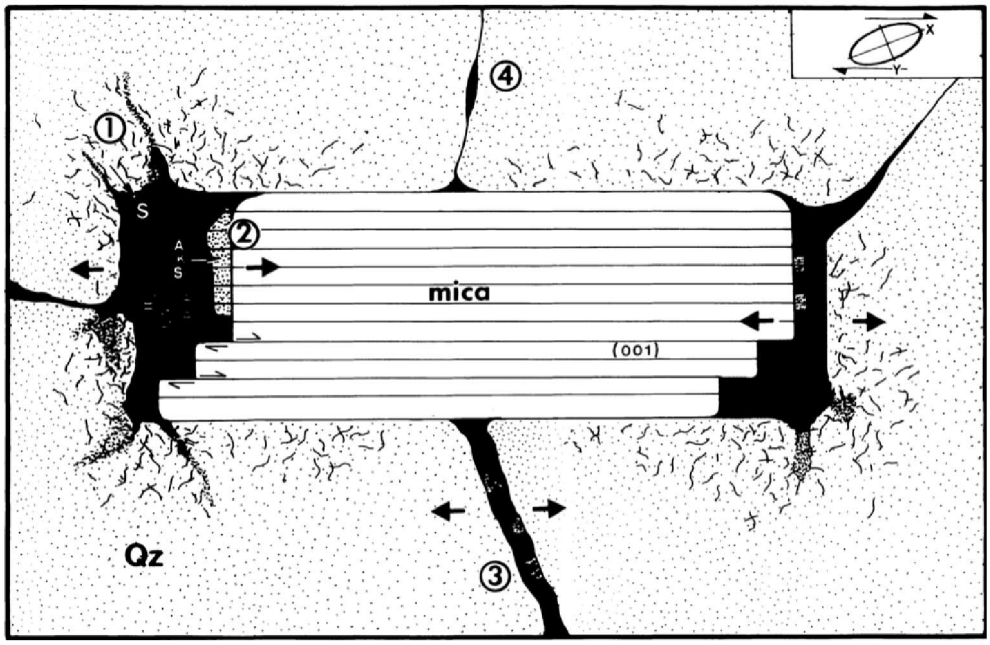

Figure 1.5 Schematic illustration of various processes observed in micacous-rich quartzites. 1) diffusion of mica grains into a neighboring quartz grain 2) recrystallization of mica when dilatant sites become available 3) Neorecrystallization at quartz grain boundaries and 4) isolated fluid gaps between quartz grains (after Hippertt 1994; figure 14).

1.3 Experimental approach

Crustal rocks found in nature are often polymineralic; to better understand the mechanical nature of polymineralic rocks at a variety of deformation conditions, experimental studies have been conducted on various rock suites to better understand the role in which different minerals play in the deformation of natural polymineralic rocks. Coaxial experiments have been conducted on a variety of mineral combinations to investigate the bulk strength of the aggregate with varying volume percentages of each phase, such as quartz-muscovite (Tullis and Wenk 1994), quartz-feldspar (Dell'angelo Tullis 1996), anhydrite-halite (Ross et al. 1987), and limestone-halite (Jordan 1988; Jordan 1987). Tullis and Wenk (1994) demonstrate that with increasing muscovite content the bulk strength of the aggregate decreases and at 50% muscovite and 50% quartz the bulk strength of the aggregate is approximately the same as pure muscovite at dislocation creep conditions in quartz. Increased muscovite content also corresponds to a decrease of the quartz fabric strength while the muscovite pins quartz grains at phase boundaries, arresting dynamic recrystallization. At volume percentages higher than 50% little to no recrystallization occurs within quartz.

Similar trends are observed in quartz-feldspar and halite-limestone aggregates, in which a mechanical transition occurs throughout the aggregate where the aggregate is initially supported by the load bearing framework phase. Transitions to interconnected weak phase layers occur when approximately 10-20% of the weak phase is present within the aggregate (Dell'Angelo and Tullis 1996; Jordan 1988; Jordan 1987). The volume percentage of the weak phase in the aggregate is often described as the most influential factor when discussing the bulk strength of polyphase aggregates, but other factors such as phase distribution, strength contrast between different phases, and grain size ratio between the different phases is also important (Handy 1994; Herwegh et al. 2011).

To produce higher strains and to better represent shear deformation observed in nature, shear and torsion experiments have been conducted on a variety of minerals. Gneiss samples were deformed using the shear geometry in a solid medium Griggs apparatus to investigate the mechanisms that promote and maintain shear zones (Holyoke and Tullis 2006), while the role of recrystallization and high temperature experiments were performed on Carrara marble in torsion (Barnhoorn et al. 2004, Pieri et al. 2001a, Pieri et al. 2001b). The gneiss experiments demonstrated that once a weak zone has localized deformation it will remain weaker than the host rock and strain partitioning will aid in the maintenance of the zone even if the shear zone becomes oriented in an unfavorable alignment. These experiments also discuss possible mineral reactions promoting new weak layers that assist in the maintenance of the shear zones, although these reactions are typically not seen in natural settings, but can be used as an analogue to reaction-based localization (Holyoke and Tullis 2006). The calcite experiments conducted by Baarnhorn et al. (2004), demonstrated that the process of recrystallization promotes the activation of different slip systems at different temperature ranges. Baarnhorn et al. (2004) also concluded that at large shear strains a secondary foliation develops due to continuous recrystallization which can overprint the original foliation and may lead to the misinterpretation of the geometry of the applied stress and strain in natural settings (Barnhoorn et al. 2004).

The experimental approach can be limited based on the material and the desired deformation conditions desired. For example, quartz is too strong to deform plastically in a torsion apparatus whereas calcite can be deformed in torsion to extremely high shear strains (γ>18) (Holyoke and Kronenberg 2010; Peiri et al. 2001a,b). This limits

plastic deformation in quartz to shear strains of 8, at the most in a Griggs apparatus in the shear geometry. Understanding deformation mechanisms that are observed in materials performed in experimental tests that are not applicable to a different material is important because these mechanisms or the minerals response to a change in mechanism provides insight into possible mechanisms for other minerals.

Hot pressed experiments have demonstrated that secondary phases can pin grain growth as either a point source or as a phase boundary (Olgaard and Evans 1988; 1986a,b). The Zener parameter is a method used to quantify the maximum grain size of the primary phase when secondary objects are present in the aggregate, figure 1.6. Alterations to the equation have been made based on the distribution geometry of the secondary phase (see Evans et al 2001), though the Zener parameter is typically used to describe isotropic secondary materials and may not accurately describe highly anisotropic materials such as phyllosilicates (Herwegh et al. 2011).

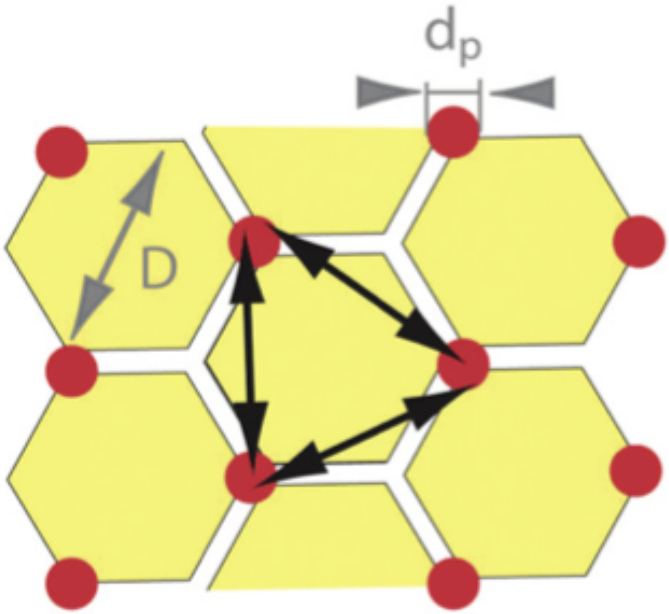

Figure 1.6 Schematic diagram illustrating the basic principles of the Zener parameter (figure after Herwegh et al 2011; figure 3).

Experimental investigations of fault rocks containing phyllosilicates have also been preformed at room temperature and 200 MPa confining pressure (Shea and Kronenberg 1993; 1992). Experiments were conducted to investigate the strength and role of anisotropy in mica schist and gneiss rocks with varying mica content. At these conditions, mica was deformed by dislocation slip and micro-kinking while the more competent phases deformed by cataclasis. Strength of these samples was largely

dependent on the concentrations, preferred orientations, and spatial arrangements of mica, so understanding how phyllosilicates distribute throughout an aggregate at ductile conditions has implications for understanding brittle and semi-brittle deformation. Room temperature rotary shear experiments were conducted on halite-muscovite aggregates to investigate the role of muscovite and other phyllosilicates in the mechanical evolution of fault rocks (Niemeijer and Spiers 2005). At sliding velocities below 0.5 μm s^{-1} muscovite developed into an anastomosing foliation and deformed by frictional sliding along the foliation plane (figure 1.7), while at sliding velocities above 0.5 μm s^{-1} velocity weakening behavior and cataclastic flow was observed.

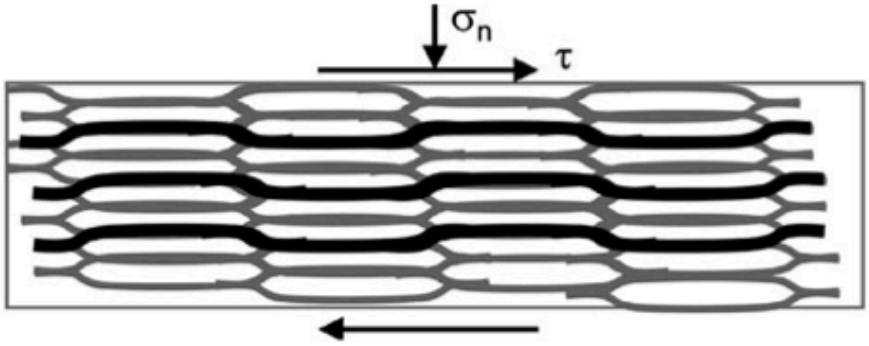

Figure 1.7 Schematic illustration describing the anastomosing foliation development of mica at sliding velocities below 0.5 μm s^{-1} (after figure 2a Niemeijer and Spiers 2005).

1.4 Modeling approach

Developing models to replicate deformation processes within earth materials is a difficult task. Many earth materials, e.g. quartz, olivine, calcite, halite, and ice to name a few, have fewer and asymmetrically disposed slip systems in comparison to fcc and bcc metals, which leads to high plastic anisotropy resulting in slip planes which are much more favored than others (Wenk et al. 1991). Two common types of models have been used to simulate fabric development in polycrystalline aggregates; models that consider purely geometrical considerations and models based on kinematic variables related to lattice rotation, stress, and strain.

Etchecopar (1977) produced a model of the CPO development in a polycrystalline aggregate of quartz. Several basic geometrical assumptions were used in the model, such as, i) each grain deformed homogeneously, ii) each grain has one dominate slip plane and can only slip in that plane, and iii) all grains deform independent of the neighboring grains. The model, for its simplicity, produces results that match natural CPO orientations observed in quartz at low shear strain. Etchecopar and Vassuers (1988)

redeveloped the 2-D model (Etchecopar 1977) to determine CPO development in a 3-D aggregate. The model again is solely based on the geometrical considerations of individual grains in a polycrystalline aggregate though in comparison to the 2-D model this model uses the basal and prism glide planes present in quartz. In comparison to the models discussed later in this section, this model is based on geometric factors such as minimization of gaps, overlaps and boundary sliding between grains, which means that there is an effect on neighboring grains, whereas most kinematic models (described later) assume that grains are isolated ellipses in a homogeneous matrix. It is assumed that processes such as, diffusion, recrystallization, flexuring, and twisting of grains are possible mechanisms that are absorbed into the process of removing gaps or overlaps observed between individual grains within the model.

The Taylor-Bishop-Hill theory and the viscoplastic self-consistent theory are two popular methods for modeling texture development in plastically deforming materials. The Taylor-Bishop-Hill theory assumes that the plastic strain in each grain is identical to the macroscopic strain, which means that deformation is assumed to be homogeneous for each increment of deformation within the given area (Molinari et al. 1987). The model also assumes that deformation only takes place by dislocation glide and that there are a discrete number of glide planes. The model also must obey a rigid-plastic flow law in relation to the resolved shear stress and strains in each glide system (Lister et al. 1978). Two further conditions of the Taylor-Bishop-Hill model are, the Von Mises criterion, which states that five linearly independent slip systems need to be activated to produce homogeneous deformation. The second condition is homogeneous strain, to ensure that grains remain in contact and that no "gaps" are developed during the deformation. These conditions reduce complications with the evolving stress state of the system, but have a negative side effect in that "hard" grains will deform at the same rate as "soft" grains, which is not representative of natural deformation (Lister et al. 1978). Although the Taylor-Bishop-Hill theory makes several major assumptions it has been used to simulate texture development for quartz (Lister et al. 1978), calcite (Lister 1978; Wagner et al. 1982), and halite (Chin and Mammel 1973; Siemes 1974).

The self-consistent theory was developed to model the plasticity of viscoplastic polycrystalline materials to large strains (Molinari et al. 1987). This theory neglects elastic strains and uses a non-linear relationship between the resolved shear stress and the microscopic shear strain rate from single crystal slip properties to predict texture

development. This theory models grains as individual ellipsoidal inclusions in a homogeneous matrix, similar to the Taylor-Bishop-Hill model. Assumptions made by this theory are that all potentially active slip systems and their critical resolved shear stresses, rate sensitivities, and hardening rates are known prior to deformation (Wenk et al. 1991). A negative side effect of this assumption is that in many cases information on various slip systems in unknown or not conclusive and approximations have to be implemented which cause further uncertainties and may prohibit various slip systems from becoming active throughout the model (Wenk et al. 1991). Similarly, as with the Taylor-Bishop-Hill theory, the self-consistent theory assumes all deformation occurs by intracrystalline slip. Successful application of the self-consistent theory has been used to study halite (Wenk et al. 1989a), quartz (Wenk et al. 1989b), olivine (Takeshita et al. 1990), calcite (Tomé et al. 1991).

Currently, these models have only dealt with single-phase aggregates. In two cases polyphase aggregates were modeled using a variation of the Taylor-Bishop-Hill model (Canova et al. 1992) and the self-consistent model (Wenk et al. 1991). Canova et al. 1992 modeled the texture development of a quartz-muscovite aggregate while Wenk et al. 1991 modeled a peridotite (olivine + enstatite). Both models produced similar relationships observed in experimental work where pure quartz or pure olivine produced a stronger CPO than in cases where there was muscovite or enstatite added. In both models there were significant limitations when it came to phase interactions due to restrictions on grain mobility.

Both the Taylor-Bishop-Hill and the viscoplastic self-consistent theories have been able to model texture development in earth materials with some success based on significant restrictions. One such restriction that is observed in nature is the process of recrystallization, which has been attributed as a significant process in the development of textures (Barnhoorn et al. 2004, Bouchez et al. 1983, Urai et al. 1986). Jessell (1988) produced a model to simulate fabric development in recrystallizing aggregates. The model is based on a Monte Carlo simulation for grain growth (see Anderson et al. 1984 for a more detailed description) where each grain is assigned a number from 1 to Q, where Q represents any integer greater than 1, with each number representing a different crystallographic orientation (figure 1.8).

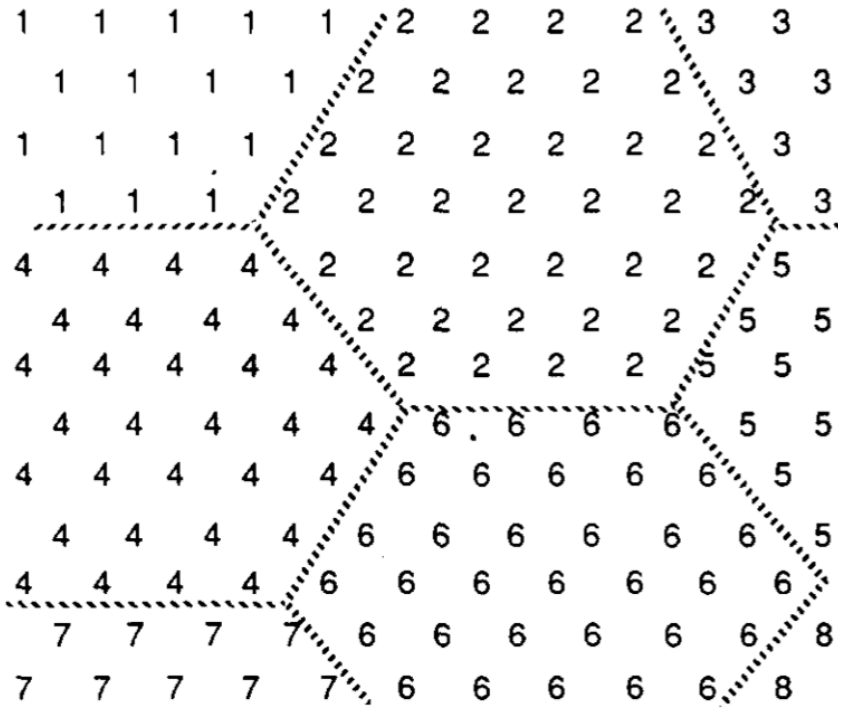

Figure 1.8 A Monte Carlo illustration for individual grains defined by a scalar number from 1 to Q where different numbers represent different crystallographic orientations (after figure 1 Jessell 1988).

Figure 1.9 compares the CPO of both simple shear and axial compression produced in this study to a model using the Talyor-Bishop-Hill model (Lister & Paterson 1979). Similar results are produced, where localization in shear is antithetic to the shear sense while in pure shear c-axes localizes around the poles in the orientation of compression, which agrees with natural and experimental results.

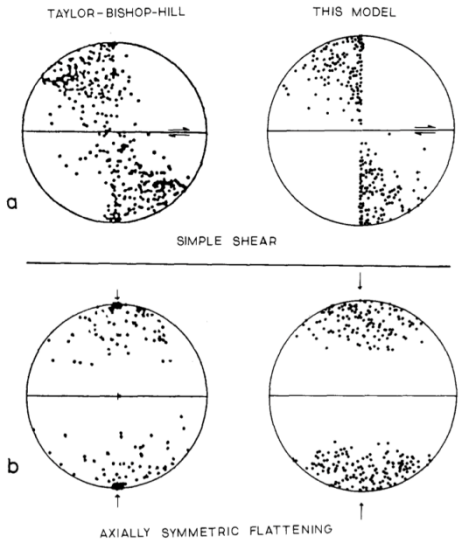

Figure 1.9 Pole figures representing a comparison between the Taylor-Bishop-Hill model presented by Lister and Paterson 1979 and Jessell 1988 Monte Carlo recrystallization model for simple shear and axial flattening (after figure 5 Jessell 1988).

1.5 Thesis outline

Chapters 2-3 of this thesis are written as independent papers in preparation to be submitted to internationally referenced earth science journals. Both chapters will each have their own specific sections such as introduction, methods, discussion, and conclusion dealing with the specific topics presented in each chapter, although overlap in various sections may occur due to the nature of their experimental approach. The format used to write the Reference section is based on the modern referencing scheme used by the Journal of Geophysical Research because this is one of the Journals we hope to publish in. Appendix A covers detailed descriptions on how to prepare and run an experiment in the Griggs apparatus and Appendix B provides extra data that is used to produce results discussed in the chapters.

CHAPTER 2: The effect of muscovite on the fabric evolution of quartz under general shear

2.1. Introduction

Ductile shear zones are high strain, localized zones observed in nature at a variety of length-scales and metamorphic conditions (Ramsey 1980). These zones weaken when the material exceeds its hardening capacity and softening mechanisms initiate (White et al. 1980). Understanding these softening mechanisms and how they initiate, development, and maintain localized deformation is fundamental in understanding the dynamics of ductile shear zones at depth. Poirier (1980) and White et al. (1980) discuss possible mechanisms for the development of shear zones, such as geometrical softening, reaction softening, pore fluid effects, and shear heating to name a few. All of these mechanisms except reaction softening concern deformation in monomineralic aggregates, though it is widely accepted that a large volume of the rocks within the earth are polymineralic (Herwegh et al. 2011). Handy (1990; 1994) discuss the importance of secondary phases as a source of weakening and their role in developing interconnected

weak phases within rock aggregates. In particular, variables between the different phases in polymineralic rocks, such as strength differences, spatial distribution, and volume percent are expected to be significantly influential in the strength of the bulk aggregate.

The mineral quartz is one of the most abundant minerals in the continental crust and is often found in many different rock types. Quartz has been extensively studied for these reasons at a variety of conditions where work from both natural and experimental settings has provided a vast database on the behavior of quartz. At midcrustal-scale conditions, quartz typically deforms by ductile processes where dislocation glide is active. Hirth and Tullis (1992) conducted coaxial experiments that outline the different recrystallization mechanisms observed in quartz while many studies have used crystallographic preferred orientation (CPO) textures of quartz to infer various deformation parameters, such as, active slip systems, shear sense indicators, paleo-stresses, and deformation geometries (Schmid and Casey 1986; Law 1990). Lisle (1985) investigated the role of secondary phases or particles in a naturally deformed conglomerate and investigated how these phases affected quartz CPO. The role of secondary phases and their influences on the bulk strength of rocks has become increasingly more important in understanding deformation at depth.

Experimental studies have previously investigated the role secondary phases have on the overall mechanical behavior of polymineralic rocks and the mechanical transition from load-bearing framework (LBF) supported aggregates to interconnected weak phase (IWP) supported aggregates, ranging from halite-calcite (Jordan 1987, 1988), mica-quartz/feldspar (Gottschalk et al., 1990; Shea and Kronenberg, 1992, 1993; Tullis and Wenk, 1994; Rawling et al. 2002), quartz-feldspar (Dell'Angelo, 1996), gneiss (Holyoke and Tullis, 2006a, b), camphor-octachloropropane (Bons and Cox, 1994), and muscovite/kaolinite-halite (Bos and Spiers 2001, 2002; Neimeijer and Spiers, 2005). A common feature observed in many of these studies shows the transition between LBF and IWP when the weaker secondary phase reached volume percentages between 15-20%. Of these experimental studies conducted at ductile conditions, coaxial geometries were used to deform the material, where only low strains can be accumulated in comparison to shear and torsion geometries. Even at low strains in coaxial deformation, a general trend is observed where as the volume percentage of the weaker increased, the fabric intensity of the stronger phase would decrease; in this case quartz (Tullis and

Wenk 1994; Dell'Angelo and Tullis 1996). General shear experiments conducted on natural gneiss samples showed mineral reactions and the interconnection of biotite grains as mechanisms that promote the transition from LBF to IWP (Holyoke and Tullis 2006). These experiments investigated aggregates with an approximate volume percentage of 10-13% biotite within the aggregate with an uncontrolled distribution of biotite. At these percentages, the aggregate is predicted to be in a transient state between LBF and IWP based on previous experiments preformed by Tullis and Wenk (1994). These experiments also do not consider how the mechanisms of mineral reactions or interconnection of biotite affect the fabric of the quartz within the gneiss as deformation evolves.

The aim of this study is to understand the role muscovite plays in the development of fabric evolution in quartz at dislocation creep conditions to high shear strains. Including pure quartz experiments conducted in this study, several other experimental studies have recently been conducted on quartz in the general shear geometry, which will allow further comparison to how muscovite can alter fabric in quartz and what this means for the application of fabric analysis on naturally deformed quartzites. A series of synthetic quartz-muscovite mixtures are deformed in a modified Griggs-type deformation apparatus.

2.2. Experimental Details

2.2.1. Starting Material

Experiments were prepared by homogeneously mixing Black Hills Quartzite (BHQ) and Black Hills Muscovite (BHM) powders, which were also used in experiments conducted by Tullis and Wenk (1994). The BHQ powder was sieved to a grain size of 63-100 μm while the BHM powder was sieved to a grain size of 45-73 μm. Four sets of powders were made with different percent volume ratios of muscovite to quartz with 0, 5, 10, 25% muscovite within the different mixtures. The sets of powders containing both muscovite and quartz were mixed in a 10 ml glass beaker under the presence of acetone in a BHQ+BHM+acetone slurry. The glass beaker is placed in an ultrasonic bath and the slurry is mixed until the acetone has completely evaporated and no visible clumps remain in the sample powders (de Ronde et al. 2005). This procedure prevents grain size and density sorting as well as mineral segregation prior to placement in the Pt jacket.

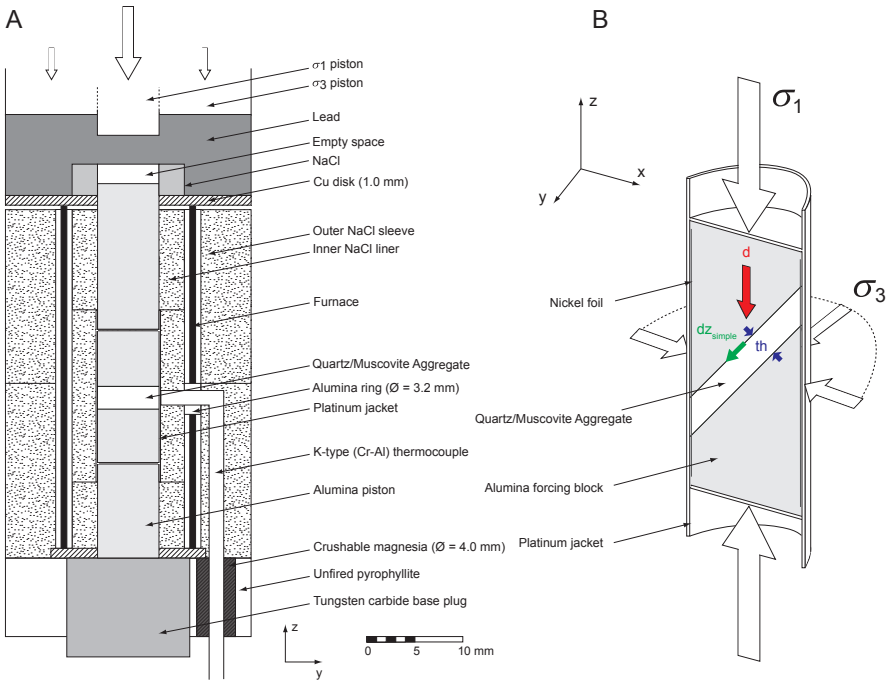

Figure 2.1 Drawing of the sample assembly and the shear geometry used in this study. a) Assembly inside of the pressure vessel in the y–z section. b) Geometry of the sample assembly for general shear experiments. Figure modified after Tarantola et al. (2010).

2.2.2.Experimental procedures

Alumina shear pistons cut at 45° to each other were used as forcing blocks to produce general shear conditions. The forcing blocks are jacketed in a Pt sleeve with Ni foil inserted between the alumina shear pistons and the Pt jacket. The starting material was placed between the two shear pistons with 0.1 wt% water added before Pt cups were used to mechanically seal the jacket so no water could escape. All deformation experiments were conducted with an axial strain rate of 10^{-4} s^{-1}, which correlates to an approximate shear strain rate of 10^{-5} s^{-1} and were conducted at 800°C and 1.5 GPa confining pressure. NaCl was used as the solid confining medium. NaCl liners were also placed between the Pt jacket and the stepped soft-fired pyrophyllite furnace. Conditions were set to produce sub-grain rotation recrystallization within the quartz while keeping muscovite mechanically stable and to avoid any melting during the experiments. These conditions were calculated based on the results of experiments conducted by Hirth and Tullis (1992) and Tullis and Wenk (1994). Figure 2.1 demonstrates the sample setup and deformation geometry inside the Pt jacket. Experiments were carried out to hydrostatic (~34 hour), peak stress (~ γ=0.6), and steady state (~ γ=4.0) conditions for

each mixture of muscovite and quartz. At the end of the experiment the temperature was lowered at the rate of 4°C/s to 200°C in order to preserve the microstructures. The differential stress decreases ~ 250 MPa from the temperature drop and is lowered at a rate of ~25 MPa min^{-1} while keeping the force on the sample ~200-300 MPa higher than the confining pressure to avoid decompression cracking within the sample material. Once the confining pressure reaches ~300 MPa during decompression, the temperature is lowered to 100°C and the force on the sample should be ~100 MPa higher than the confining pressure. The pressure slowly decreases until atmospheric conditions are reached.

2.3. Results

Experiments were observed by optical means using a standard petrographic microscope. Thin sections were cut perpendicular to the shear direction and polished to first-order grey values for the mineral quartz. Photomicrographs are displayed using a circular polarizer, crossed polarizers, or plane light to describe the microstructures. A circular polarizer is used to better present individual quartz grains in aggregates that possess a strong crystallographic fabric while photomicrographs using cross polarizers and plane light were used when describing microstructural features involving muscovite, because at the light microscope scale, small muscovite grains are difficult to identify and plane light is used to display muscovite within the aggregate.

The mechanical data (figure 2.2), displays the relationship that the greater the percentage of muscovite within the aggregate, the weaker the bulk strength of the aggregate becomes. The flow stress for the pure quartz experiment (379LT) is 287 MPa, while at 5% muscovite the flow stress decreases to approximately 240 MPa and at 10% muscovite the aggregate is approximately half as weak as the pure quartz experiment, with a flow stress ~150 MPa. The weakest sample was when the aggregate contained 25% muscovite. At 25% muscovite, the flow stress is 83 MPa, which is roughly 3.5x weaker than the pure quartz experiment.

Table 2.1 *Synthetic Quartz-Muscovite Deformed in General Shear at T=800 °C and P_c = 1.5 GPa*

Experiment #	Muscovite (%)	$\dot{\gamma}$ (s^{-1})	γ
370LT	0	1.25×10^{-5}	0.75
372LT	0	0	0
379LT	0	9.42×10^{-6}	3.96
382LT	5	1.83×10^{-5}	3.78
385LT	5	1.30×10^{-5}	0.64
389LT	10	1.75×10^{-5}	4.14
390LT	10	1.24×10^{-5}	0.52
391LT	25	1.91×10^{-5}	4.18
392LT	25	1.73×10^{-5}	0.53
394LT	5	0	0
396LT	10	0	0
398LT	25	0	0

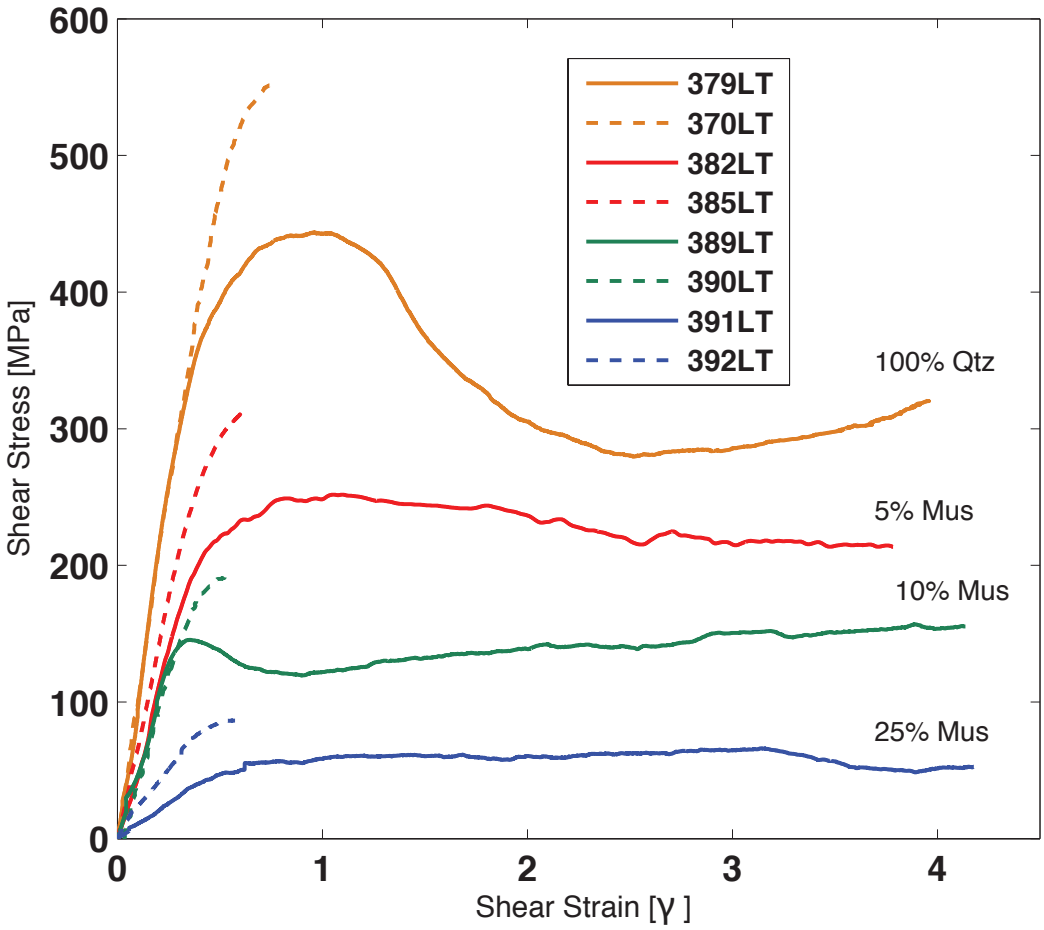

Figure 2.2 Stress–strain relationships for different deformed mixtures of quartz and muscovite in shear at 800°C and a shear strain rate of ~10^{-5} (s^{-1}).

2.3.1. Microstructural observations

2.3.1.1. Hydrostatic

Hydrostatic experiments were brought to a pressure and temperature of 1.5 GPa and 800°C respectively and hot pressed for ~34 hours and then quenched. The pure quartz aggregate shows slight grain crushing at grain boundaries and no internal deformation processes related to dislocation motion are observed. Grains can show internal microcracking due to pressurization, while quartz grain shapes can possess both round and sharp edges (figure 2.3a). When there is 5% muscovite within the aggregate, the muscovite grains are isolated from each other and sit between quartz grains. Muscovite grains can be found straight or bent, indicating they have no mechanical control or affect on the surrounding quartz grains during pressurization. In several cases, quartz grains that neighbor mica grains show small amounts of undulose extinction located in regions near a phase boundary, indicating possible stress concentrations near these phase boundaries (figure 2.3b). The aggregate also displays grain growth of new quartz grains. These new grains originate at grain boundaries and grain interiors, with the new grains nucleating from the crushed material during pressurization and grow statically over time. These nucleated grains show an average grain size of 10-15μm.

At 10% muscovite, the aggregate displays local connectivity between muscovite grains, where in some regions of the aggregate various muscovite grains are interconnected and in other regions the muscovite grains remain isolated where a lack of global connectivity throughout the aggregate has not been achieved. Grain growth is still apparent in the quartz grains while no undulose extinction was observed (figure 2.3c). At 25% muscovite, little to no grain growth is observed throughout the aggregate due to a lack of grain crushing as muscovite is interpreted to cushion quartz grains during pressurization (figure 2.3d). Muscovite is globally connected throughout the aggregate, where muscovite grains are connected throughout the majority of the aggregate and are assumed to partition the majority of the strain during deformation. This observation indicated that muscovite is the controlling phase of the aggregate though quartz grain boundaries still exist. Grain nucleation is prominent in the 5% and 10% muscovite samples and is not observed in the 25% muscovite aggregate as previously discussed while the pure quartz sample shows grain crushing; grain growth is not visible until peak stress conditions.

There seems to be slight alteration in the muscovite during the experiments. In plane light, muscovite is typically clear, but all the muscovite in these experiments posses a greenish tint in plane light though (figure 2.7b). EDS on various muscovite grains, both newly recrystallized and old grains showed no signs of melt production and are chemically stable (see Appendix B for EDS results). This greenish tint in plane light is attributed to possible lattice distortions and twinning. Experimental work by Herman and Green (2001) demonstrate that muscovite at these conditions (800°C and 15kbar) is close to melt conditions and that the muscovite could potentially become phengite if sufficient Mg is present within the sample.

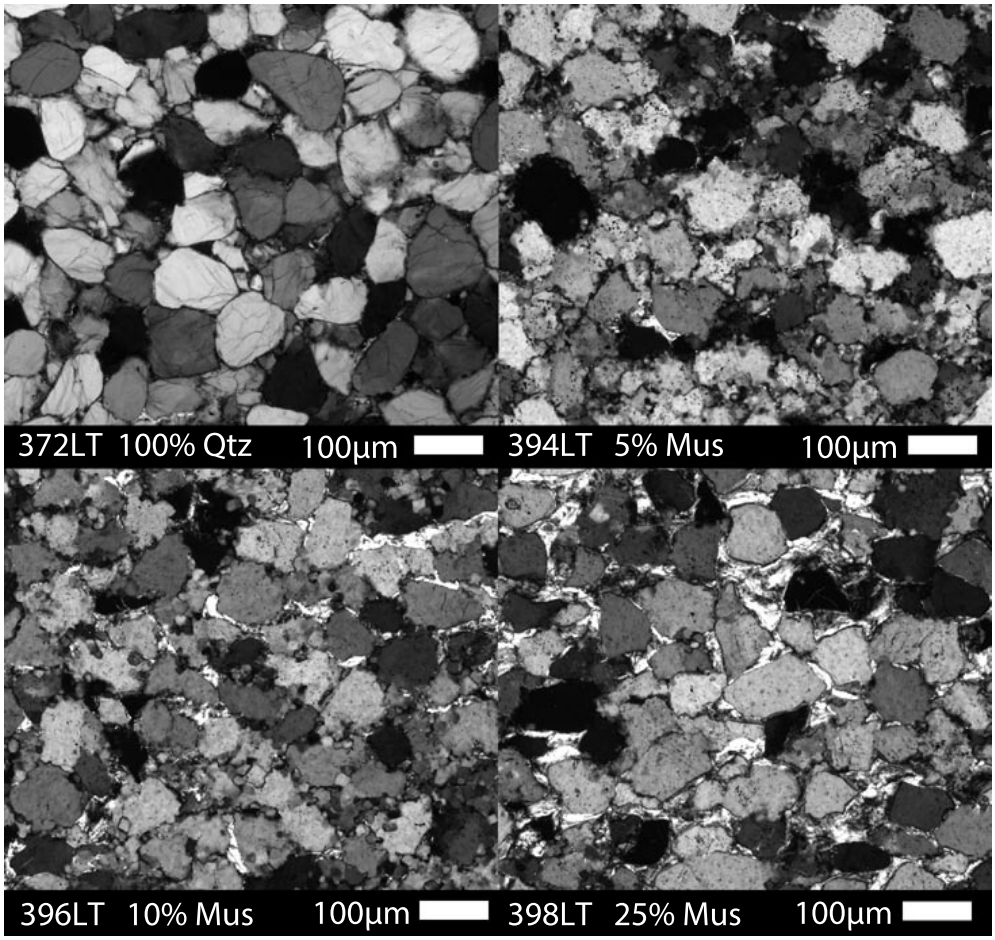

Figure 2.3 Micrographs for the different quartz-muscovite mixtures at hydrostatic conditions. Samples were brought to temperature and pressure conditions where they sat for 34 hours before samples were quenched. These are circular-polarized images; muscovite grains are visible as the brightest grains and are tabular in shape. Quartz grains are represented by various shades of grey.

2.3.1.2. Peak Stress

At peak stress conditions, the pure quartz aggregate has produced ~10% recrystallization with a recrystallization grain size ranging from ~8 – 15μm. The sample demonstrates homogeneous deformation with a foliation ~25° to the shear plane. The foliation is defined by the shape preferred orientation (SPO) of the original quartz grains. The original quartz grains demonstrate elongation parallel to the foliation plane where recrystallization is dominated along the foliation plane and serrated grain boundaries are dominantly observed perpendicular to the foliation plane (figure 2.4a). When there is 5% muscovite within the aggregate, the muscovite grains are isolated and randomly orientated though some muscovite grains help define a foliation ~25° to the shear plane which is defined by the SPO of the original quartz grains (figure 2.4b). There is ~5% recrystallization of the quartz grains within the sample. At 10% muscovite, a foliation has developed based on the SPO within the quartz at ~25° to the shear plane. The muscovite is locally connected throughout the aggregate, where in some regions of the aggregate various muscovite grains are interconnected in an anastomosing pattern and in other regions the muscovite grains remain isolated. There is <5% recrystallization of the quartz grains within the aggregate and many grain boundaries are serrated (figure 2.4c). At 25% muscovite, there is no detectable SPO and little to no (~1%) recrystallization within quartz grains. The muscovite is globally connected throughout the aggregate and quartz undergoes little to no plastic deformation (figure 2.4d).

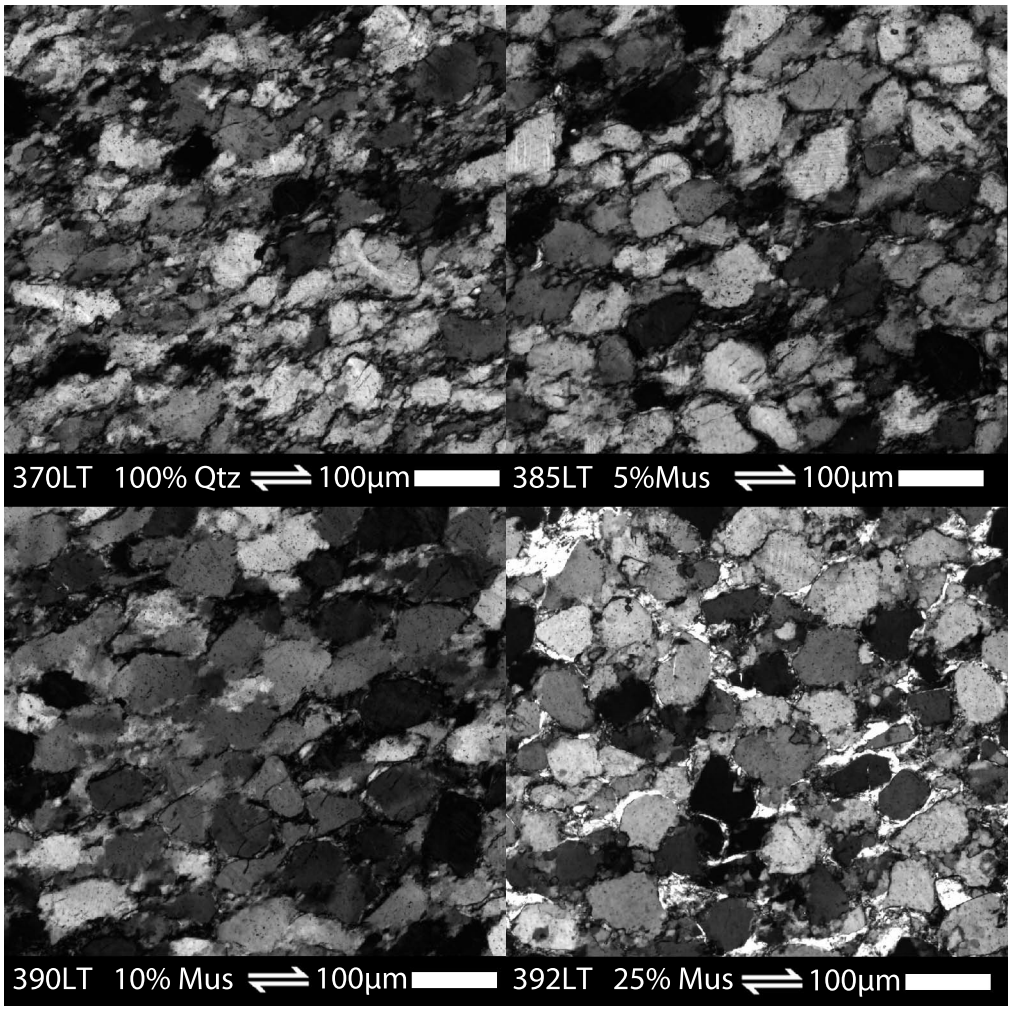

Figure 2.4 Micrographs for the different quartz-muscovite mixtures at peak stress conditions. These images are taken using a circular polarizer and the shear plane is horizontal to the frame of the micrographs. Recrystallization and the development of a shape-preferred orientation (SPO) are clearly visible in each image.

2.3.1.3. Steady State

Steady state experiments were run to $\gamma \sim 4$. At 100% quartz, the sample weakens after reaching peak stress and around $\gamma \sim 2.5$, the sample appears to reach steady state conditions. At this point, the shear stress slowly and continuously increases until the sample is quenched (figure 2.2). This subsequent increase in the shear stress at the onset of the steady state deformation is attributed to thinning of the sample and an increase in the strain rate, which has previously been observed and documented by Heilbronner and Tullis (2006). The aggregate displays ~95% recrystallization with a very strong foliation defined by the SPO of the non-recrystallized grains while many grains also display undulose extinction and deformation lamellae (figure 2.5a). Original grains that have elongated, into ribbons, often possess many subgrains or tilt walls throughout and possess serrated grain boundaries. In a few cases, grains orientated in the Ymax orientation are observed as ribbons that possess fairly straight undeformed

grain boundaries, which indicate that these grains are in an optimal orientation for intracrystalline slip. Throughout the entire aggregate there is a variation in accumulated strain with the central portions of the sample experiencing the highest accumulation of strain while opposing top and bottom corner regions of least displacement regions display the least amount of strain accumulation (figure 2.6). Figure 2.6 is a schematic illustration that displays the development of the high and low strain regions in some samples. All experimental samples start out in the hydrostatic position, illustrated by (figure 2.6a). By steady state conditions, the sample and pistons resemble the geometry illustrated in (figure 2.6b). The purple shaded region is the centrally high strain region where the neighboring grey regions are the oppositely opposing low strain regions. The red arrows indicate the amount of displacement accumulated from one end of the shear plane surface to the other. The larger the red arrow, the greater the displacement the material experiences and higher strain accumulation is observed in these regions that experience the greatest change in displacement over the entire experiment. The recrystallized grain size for the grains differs throughout the aggregate. In the central, highest strain, region the recrystallized grain size is ~4.2μm while in the lowest strain region the recrystallized grain size is ~8.1μm, but can be as large as 15μm.

At 5% muscovite there is still a variation in strain across the sample but this variation is not as strong as in the 100% quartz sample. This is due to strain partitioning into the, weaker, muscovite grains. There is ~80% recrystallization of quartz grains within the aggregate, while in the highest strain region the muscovite grains are approximately parallel to the shear plane. Individual muscovite grains connect with each other, developing thin linear mica stands though they can also be observed to bend around grains developing an anastomosing pattern. In the highest strain regions close to the piston-sample interface, C' shear bands form at ~30° to the shear plane where muscovite grains are typically found within the shear bands, but not in every case, (figure 2.5b) and (figure 2.7). In (figure 2.6b) red lines in the shaded high strain region refer to the location where these C' shear bands are forming. These shear bands are typically 300-500μm in length and terminate into a weak S-C; foliation. The S-C' foliation is only observed near these C' shear bands.

At 10% muscovite there is a significant drop in the volume of quartz recrystallization, with ~30% recrystallization. Quartz grains, however, still demonstrate undoluse extinction and deformation lamellae at quartz grain boundaries. Deformation

appears homogenous throughout the sample with no variation in strain, which is an indication of strain partitioning into muscovite grains. C' shear bands have developed throughout the entire aggregate with two distinct sets of angles, a high angle set at ~50° and a low angle set at ~25°, while muscovite grains form an anastomosing connectivity throughout the majority of the aggregate, though not globally, figure 2.5c. The presence of C' shear bands and interconnecting muscovite grains are interpreted to be partitioning the majority of the strain in the sample. A weak foliation is observed where quartz clasts are orientated nearly perpendicular to the orientation of the C' shear bands and define the foliation along with the muscovite grains, this can be interpreted as the S plane in a S-C' foliation, figure 2.8. At 10% muscovite the C' shear bands are defined by offset in both muscovite and quartz grains, where muscovite grains can be observed bending into the shear bands where as quartz grains are aligned into the S plane as previously noted.

Finally, at 25% muscovite there is <10% recrystallization with globally connected muscovite grains in an anastomosing geometry. Quartz grains show deformation lamellae as well as deformation bands but display no sign of internal recrystallization, which is another indication of strain partitioning into the surrounding muscovite grains. Strain within the sample is homogenous as in the 10% muscovite sample. C' shear bands are present within the aggregate, but only near the high displacement regions near the sample-piston interface similar to the 5% muscovite sample, figure 2.6b. These C' shear bands are longer than the bands at 5%, ranging from 600-700μm. Throughout the aggregate muscovite is so abundant that offset for C' shear bands is difficult to identify, figure 2.5d. This indicates that at 25% muscovite in the aggregate, the aggregate is dominantly controlled by the anastomosing connectivity of the muscovite.

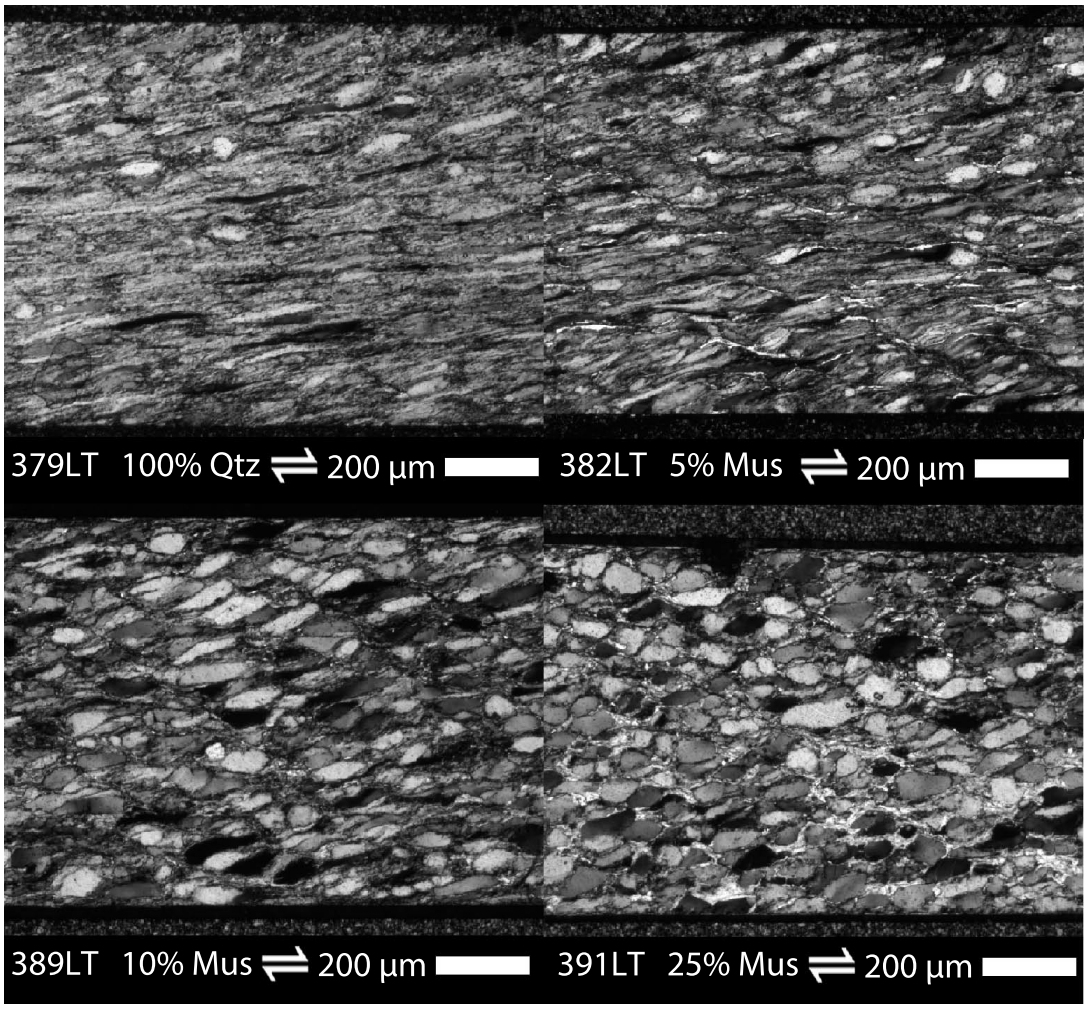

Figure 2.5 Micrographs for the different quartz-muscovite mixtures at steady state conditions. Micrographs are taken with a circular polarizer. Muscovite can be identified as the brightest grains in the aggregates. At steady state conditions, visible muscovite grains are long strands except in the 25% muscovite sample where muscovite forms an anastomosing pattern. The Shear plane is horizontal to the frame of the picture. In all four micrographs the sample-piston interface is visible at the top and bottom of each micrograph.

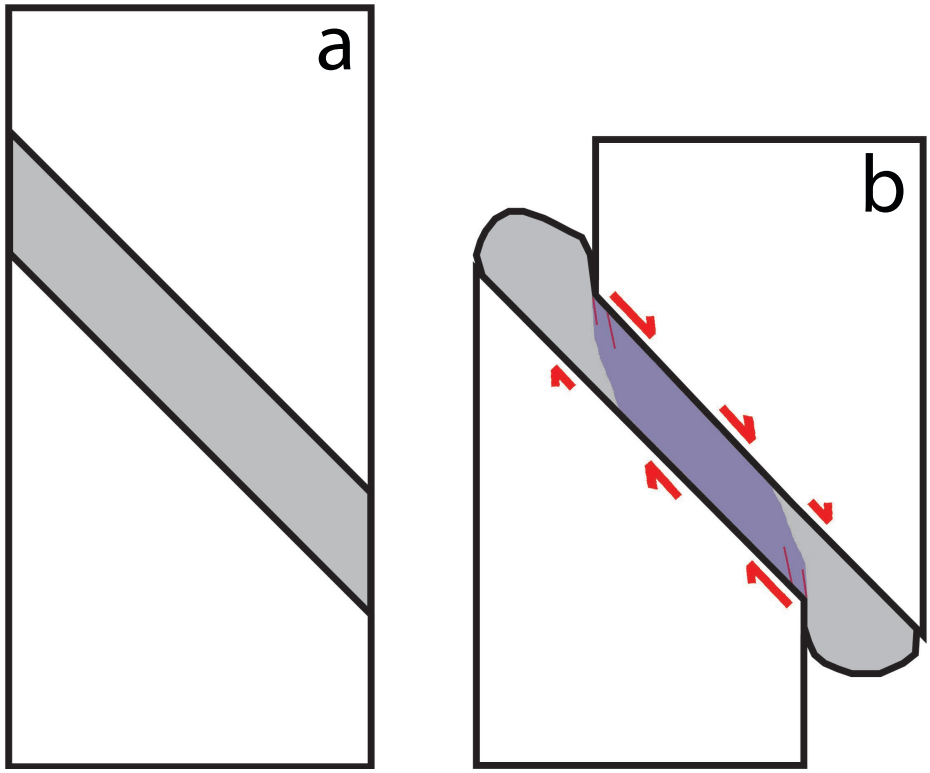

Figure 2.6 Schematic illustration of the shear geometry before and after deformation to high shear strains. a) White regions are the shear pistons and the grey region is the sample material. This is the geometry of all shear experiments prior to deformation. b) after the accumulation of high shear strains the sample geometry resembles this illustration where the shear pistons are offset. The corners of the shear pistons where the largest red arrows become much closer to each other in comparison to the shear piston corners near the small red arrows. The size of the red arrows indicates the amount of displacement change with the largest red arrows displaying the region experiencing the high change in displacement. The purple shaded region is the high strain region and the grey region is the low strain region. In the 5% and 25% muscovite samples preformed to steady state condtions C' shear bands form at the sample-piston interface where red lines have been placed.

2.3.2. C' shear bands and muscovite distribution

Based on microstructural observations, strain is partitioned into muscovite grains throughout deformation. The development of features such as C' shear bands, dissolution-precipitation processes, and recrystallization help muscovite migrate and redistribute throughout the aggregate, in turn developing a network of muscovite grains that weaken the aggregate. Two types of C' shear bands are observed in the three steady state aggregates; shear bands that are associated with the piston-sample interface, (figure 2.7), and shear bands that are not (figure 2.8). C' shear bands that are located at the sample-piston interface are often associated with slip on muscovite grains. Muscovite grains that do not define the plane of the shear band can be seen bending into the shear band enabling a sense of shear to be determined; drextral in (figure 2.7). The yellow box in (figure 2.7b) displays an important process where quartz is dynamically recrystallizing, and during dynamic recrystallization muscovite is precipitating in between the grain boundaries. The small muscovite grains can be identified in the plane

light micrograph in (figure 2.7b) as long thin layers with a greenish tint. This process is observed on the left side of this same shear band and observed throughout the aggregate. Based on the observations of just a light microscope, it is difficult to determine the mechanism that is redistributing muscovite into these spaces and whether it is dynamic recrystallization or dissolution-precipitation processes.

The second type of C' shear band observed are shear bands that are not associated with the sample-piston interface. In both the 5% and 10% muscovite samples, short, 100-300μm, C' shear bands that begin and end at the tips of muscovite grains are observed. These features are due to increases of stress concentrations at the tips of the muscovite grains and promote semi-brittle flow in the form of a C' shear band. These types of C' shear bands can form without the presence of muscovite. These shear bands are much shorter in length than the other shear bands, where the solid yellow line defines a shear band associated with the sample-piston interface and the yellow box displays a shear band that formed without muscovite present and stretches the diagonal length of the yellow box (figure 2.8).

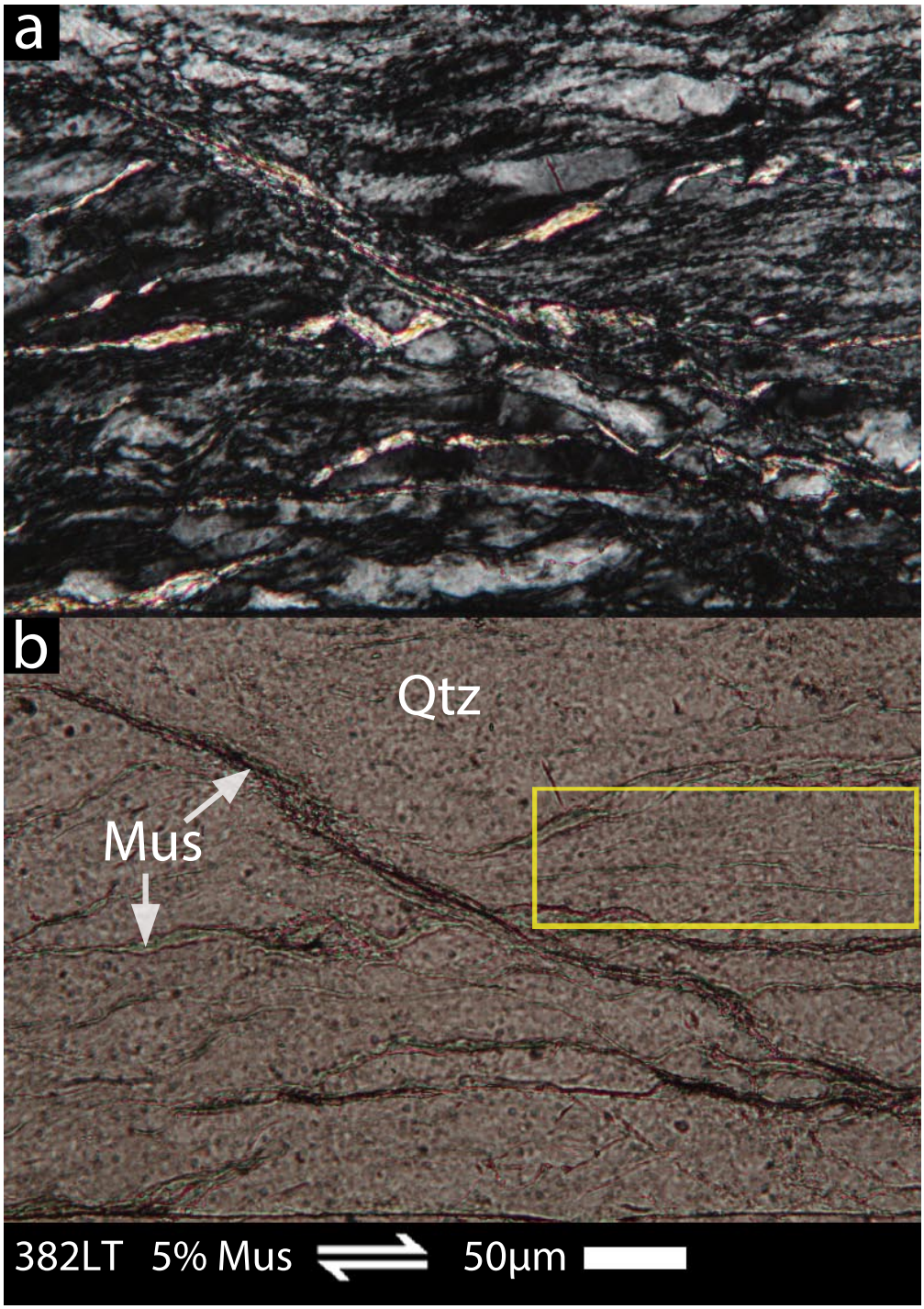

Figure 2.7 Micrograph of a C' shear band. a) Crossed-polarizer image of a C' shear band. The shear band is defined by the largest muscovite grain oriented antithetic to the dextral sense of shear. Other muscovite grains can be observed bending into the C' shear band which is a common feature. b) Plane light image of 'a' where the white arrow points to the C' shear band and the yellow box identifies a region of dynamic recrystallization in 'a' and in plane light the greenish tinted muscovite can be identified precipitating into this zone. Shear plane horizontal to the frame of the image.

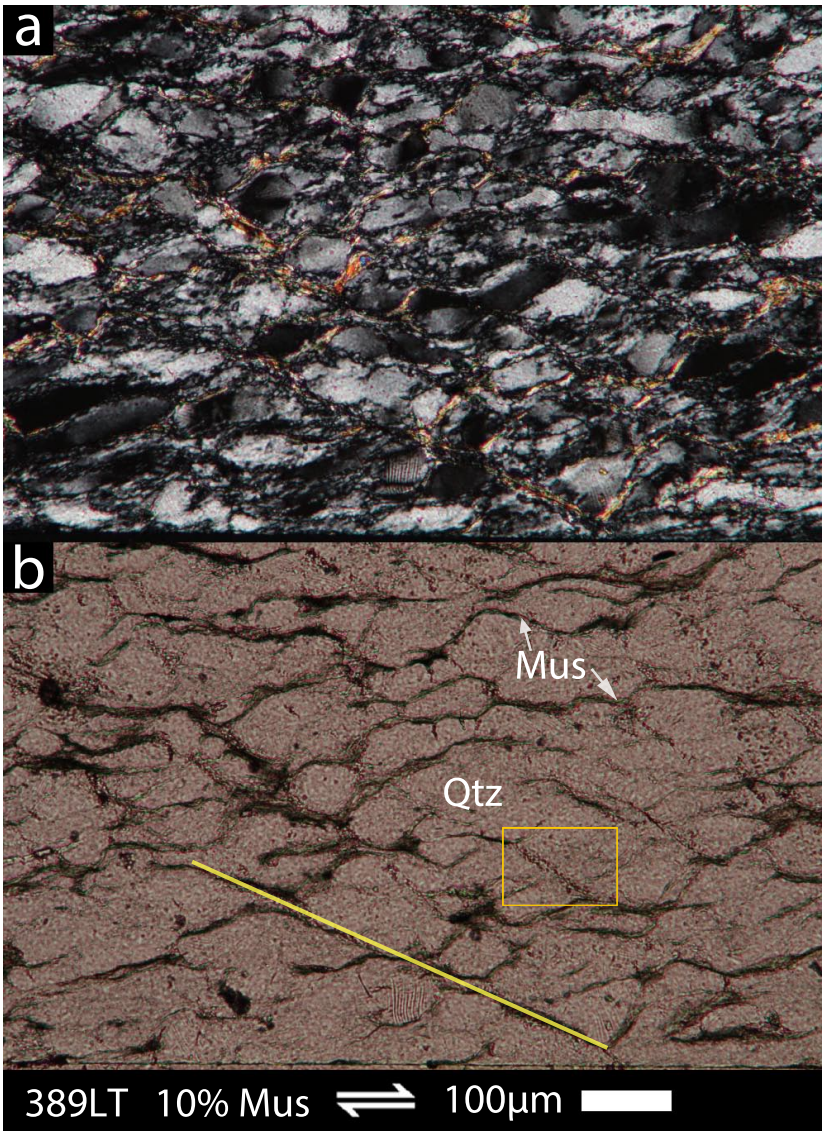

Figure 2.9 Micrograph of larger C' shear bands where shear bands slip on both muscovite and quartz. a) Crossed-polarized light image where C' shear bands are visible by the linear features. Some shear bands are up to 700µm long while others are a few hundred microns in length. b) The yellow line outlines the largest C' shear band while the yellow box is the region of interest in figure 2.9 where the shear band is defined by small granular quartz grains. The shear plane is horizontal to the frame of the picture.

The C' shear bands located centrally within the aggregate often promote recrystallization of muscovite and dissolution-precipitation processes. An electron back-scatter image shows several convincing features that promote muscovite redistribution throughout the aggregate (figure 2.10). In figure 2.10, there are five different labels of various features or mechanisms observed associated with the development of these C' shear bands and muscovite redistribution. Label 1, represents what are interpreted as void spaces created during the development of these smaller shear bands because of the high stress concentrations. It is possible these voids are crystallographically controlled but further work is needed to prove this hypothesis although it is still an important observation that void spaces can be created at such high confining pressures. The light

colored regions surrounding label 2 are muscovite grains located within a quartz grain where no visible crack or void space is transporting these muscovite grains internally within quartz grains. The mechanism interpreted to promote this type of migration is dissolution-precipitation. All experiments contain 0.1wt% H_2O prior to deformation and with muscovite, likely possessing some H_2O, present in the aggregate already, increased fluid pressures can aid in the activity of dissolution-precipitation processes. Label 3 is also interpreted as muscovite precipitation along micro-cracks both at grain boundaries and grain interiors. Muscovite precipitation along a boundary or crack can also be observed at the top and bottom of (figure 2.10) and it is interpreted as the most efficient process for redistributing muscovite throughout the aggregate. Label 4 depicts a linear line of void spaces originally described by label 1. This linear feature is interpreted as a C' shear band. Label 5 displays the precipitation of muscovite into these void spaces which define the C' shear band. The combination of processes identified at labels 3, 4, and 5 are interpreted as the primary mechanisms that redistribute muscovite while deformation is active.

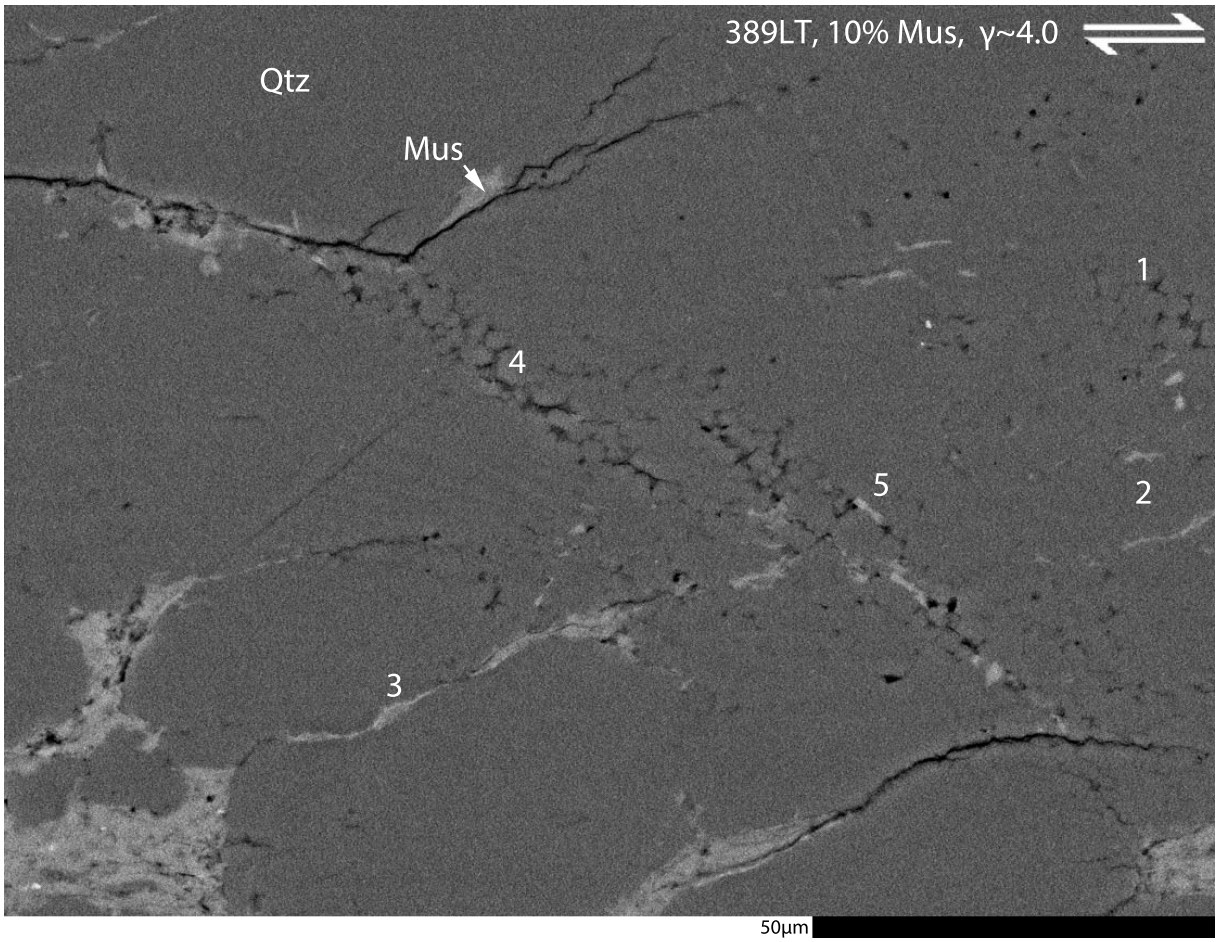

Figure 2.10 Electron back-scatter image from the region defined by the yellow box in figure 2.8. Quartz (Qtz) is defined by the dark grey color, while muscovite (Mus) is defined by the lighter grey color. 1) Displays an examples of small, ~1-3µm, granular quartz grains and void spaces at high confining pressures. 2) Location 2 describes muscovite grains isolated within a quartz grain. This is interpreted to occur by dissolution-precipitation processes. 3) Dissolution-precipitation of muscovite along grain boundaries. 4) C' shear band defined by the small granular quartz grains and void spaces. 5) Displays precipitation of muscovite into the void spaces defining the C' shear band. This process is interpreted as one of the mechanisms distributing muscovite throughout the aggregate during deformation.

2.3.3. Shape Preferred Orientations (SPO)

Grain boundary maps were constructed on equal area photomicrographs for each experiment where different shape preferred orientations (SPO) could be calculated using the surface orientation program, SURFOR, and the particle orientation program, PAROR (Panozzo 1983; Panozzo 1984; Schmid et al. 1987). Figures 2.11, 2.12 display all the SURFOR and PAROR data for each experiment (see Appendix B for grain boundary maps). The first column displays a surface orientation plot, which is known as the alpha plot where the y-axis represents 'b/a', where 'a' is the projection of the long axis of the grain on the x-coordinate axis and 'b' is the projection of the short axis of the grain on the y-coordinate axis. This makes 'b/a' the axial ratio of the short axis over the long axis of the grain. On the x-axis of the alpha plot is 'α', which is the projection curve between

the grain projection divided by the maximum projection. 90-α provides the angle between the relative grain projections and the shear plane. If the aggregate consisted of perfect spheres then the black line would be a horizontal line at b/a=1, because the short and long axis would be the identical. The more 'a' increases than 'b' within the grains of the aggregate, the deeper the well becomes developing similar grain projection orientations, i.e. foliation development. The diagrams in the second column of figures 2.11, 2.12 are rose plots, which plot normalized lengths of the aspect ratio 'a/b' in relation to the shear plane. The horizontal line in the rose plots defines the shear plane. The third column is an alpha plot describing the particle orientation of the grains, where 'α' represents the projection of the long axis of individual grains to the shear plane. 90-α provides the angle between the long axes of the grains to the shear plane. The fourth column is a rose diagram representing the long axis in relation to the shear plane.

At hydrostatic conditions, aggregate assemblages of 0, 5, and 10% muscovite demonstrate a random SPO, while the 25% muscovite aggregate assemblage demonstrates a slight preferred orientation approximately 35° above the shear plane. This preferred orientation is likely due to a combination of rotation of quartz grains where the long axis is perpendicular to the sigma 1 direction and a lack of grain crushing, due to a greater volume of phase boundaries to grain boundaries during compression resulting in more angular grains than in previous aggregate mixtures.

SPO development at peak stress conditions display a very similar result for the 100% quartz and 5% muscovite aggregates where the long axis of the grains is approximately 25° to the shear plane. At 10% muscovite, the long axis of the grains is higher than the 100% quartz and 5% muscovite aggregates, measured to 30° to the shear plane. This is likely due to the presence of C' shear planes spanning throughout the entire aggregate whereas the 100% quartz aggregate does not possess any C' shear bands while the 5% muscovite sample displays C' shear bands only in the high displacement regions at the sample-piston interfaces. At 25% muscovite, the long axes of the grains possess an angle of only 15° to the shear plane. This result agrees with the 25% muscovite hydrostatic sample where quartz grains rotate freely and at peak stress conditions the grains are rotating towards the shear plane. It should be noted that no recrystallization has occurred at peak stress conditions and the rose diagrams are normalized to a maximum of 1. A general trend observed is that from 5% to 25%

muscovite, the more muscovite within the aggregate the smaller the axial ratio of quartz grains becomes.

At steady state conditions, the SPO development between the four different samples displays a clear transition from the 100% quartz sample to the 25% muscovite sample. At 100% quartz and 5% muscovite, the surface and particle analyzes are similar with aspect ratios of 2.97 and 2.74, respectively with the long axis of the grains lying ~10-15° to the shear plane. These results likely indicate that both aggregates are clearly controlled by the load-bearing phase, quartz. At 5% muscovite, muscovite grains are largely insignificant in influencing quartz SPO at high strains. At 10% muscovite, the long axis of quartz grains is ~20° to the shear plane while possessing a lower aspect ratio at 1.95 in comparison to the 100% quartz and 5% muscovite samples. This result demonstrates that at a volume percent around 10%, muscovite grains partition a noticeable amount of the bulk strain; although at 25% muscovite, the sample possesses the broadest aspect ratio of 1.59 and no further rotation in relation to the 25% peak stress experiment. This result indicates that by 25% muscovite, the bulk of the strain is portioned into the muscovite grains.

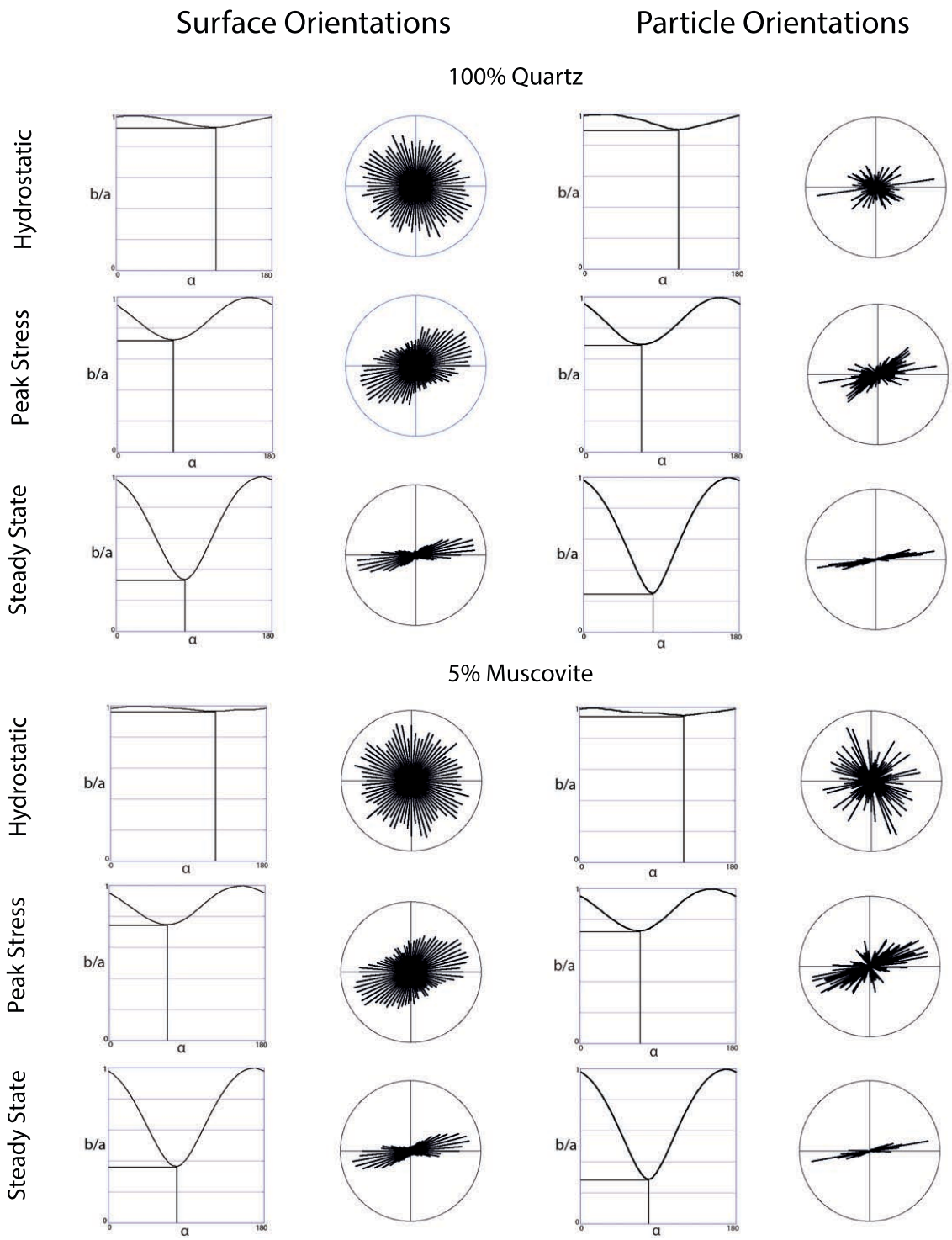

Figure 2.11 Surface and particle orientations for hydrostatic, peak stress, and steady state experiments for 100% quartz and 5% muscovite samples. The first column is the alpha plot for surface orientations where 'a' is the projection of the long axis and 'b' is the projection of the short axis of grains. 'b/a' is the axial ratio of the short to long axis projections. 'a/b' is commonly referred to as the aspect ratio of a grain. 'α' is the angle of the different grain boundary segments to the shear plane. 90-α, at the minimum α value, provides the angle of the long axis of the strain ellipse to the shear plane. In the second column are rose plots that represent the orientations of grain boundary segments to the shear zone boundary, which is the E-W horizontal plane. In the third column are alpha plots for particle analyses, where 'a' and 'b' are the same but 'α' is the angle between the long axis of the grain and the z-coordinate axis (or shear zone plane). The fourth column are rose plots for particle analyses where 90 minus the minimum alpha value provides the angle of the long axis of each grain to the shear plane.

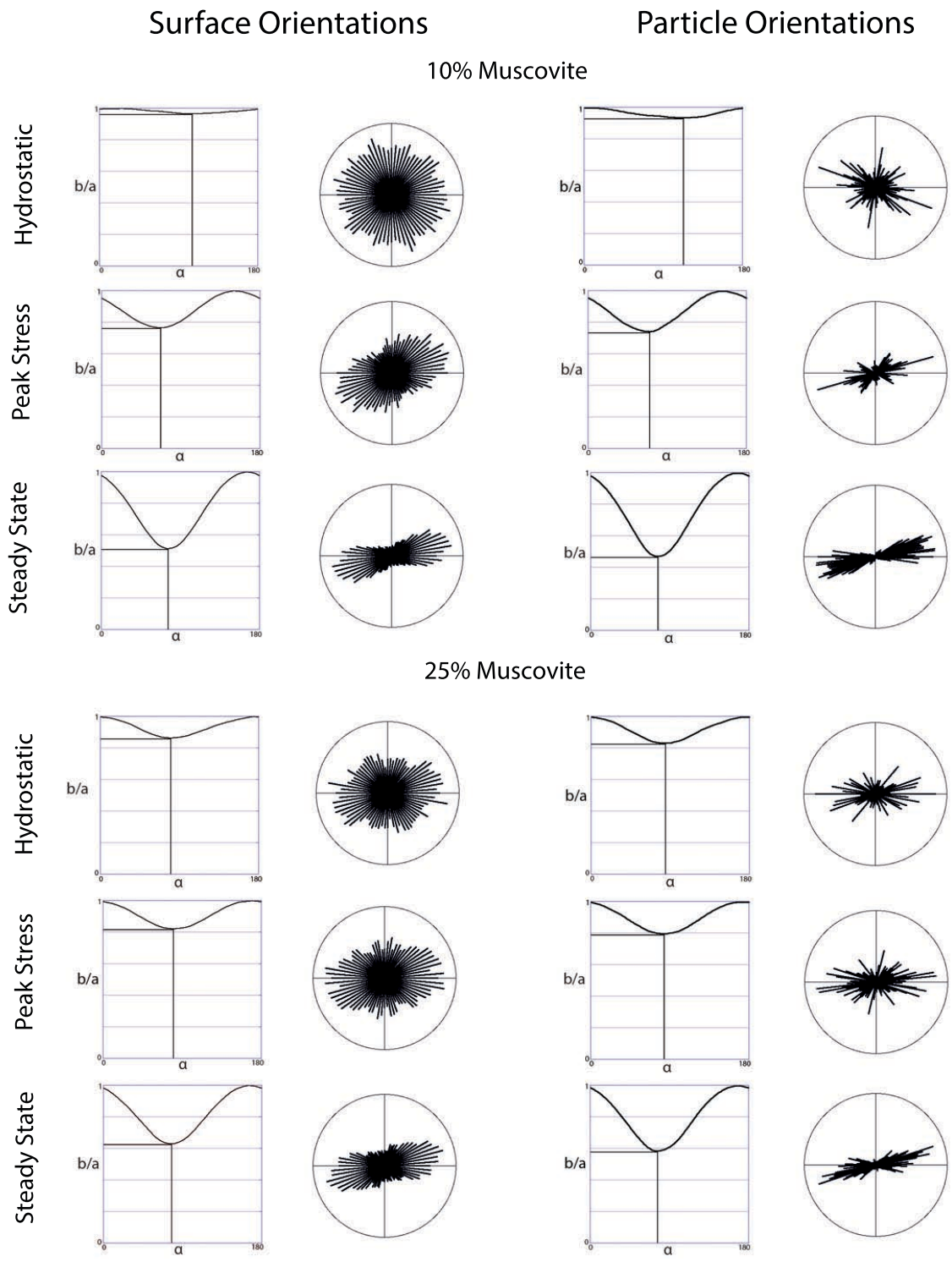

Figure 2.12 Surface and particle orientations for 10% and 25% muscovite samples. Plots are organized in the same manor as figure 2.10.

2.3.4. Crystallographic Preferred Orientations (CPO)

2.3.4.1. Bulk CPO

The CPO of quartz for each aggregate was measured by computer-integrated polarized (CIP) microscopy (Heilbronner and Pauli 1993; Heilbronner and Tullis 2006). The CIP analysis produces c-axis orientation images of uniaxial materials, in this case quartz. Masked portions of the images are regions of the aggregate that are unwanted for orientation measurement. These masked regions can be artifacts during sample preparation and/or undesired minerals. A color look-up table (CLUT) is used as a key to represent the c-axis orientations in the CIP image. The program, Image SXM, was used to create the pole figures using the macro 'lazy pole' from the CIP database. Each pole figure has a contour spacing of 0.5 and the shear plane for all pole figures is in the east-west orientation with a dextral sense of shear.

Hydrostatic experiments all display a random CPO, figure 2.13. As mentioned in the microstructures section, grain crushing and grain growth can be observed in both the circular polarized micrographs. CIP images also observe crushed grains in several CIP maps. This is also observed in single crystal quartz experiments conducted by Muto et al. (2011). The CPO of the newly grown quartz grains is not controlled by the CPO of the original grain, which agrees with the assumption that these grains grew from crushed quartz during pressurization, figure 2.14.

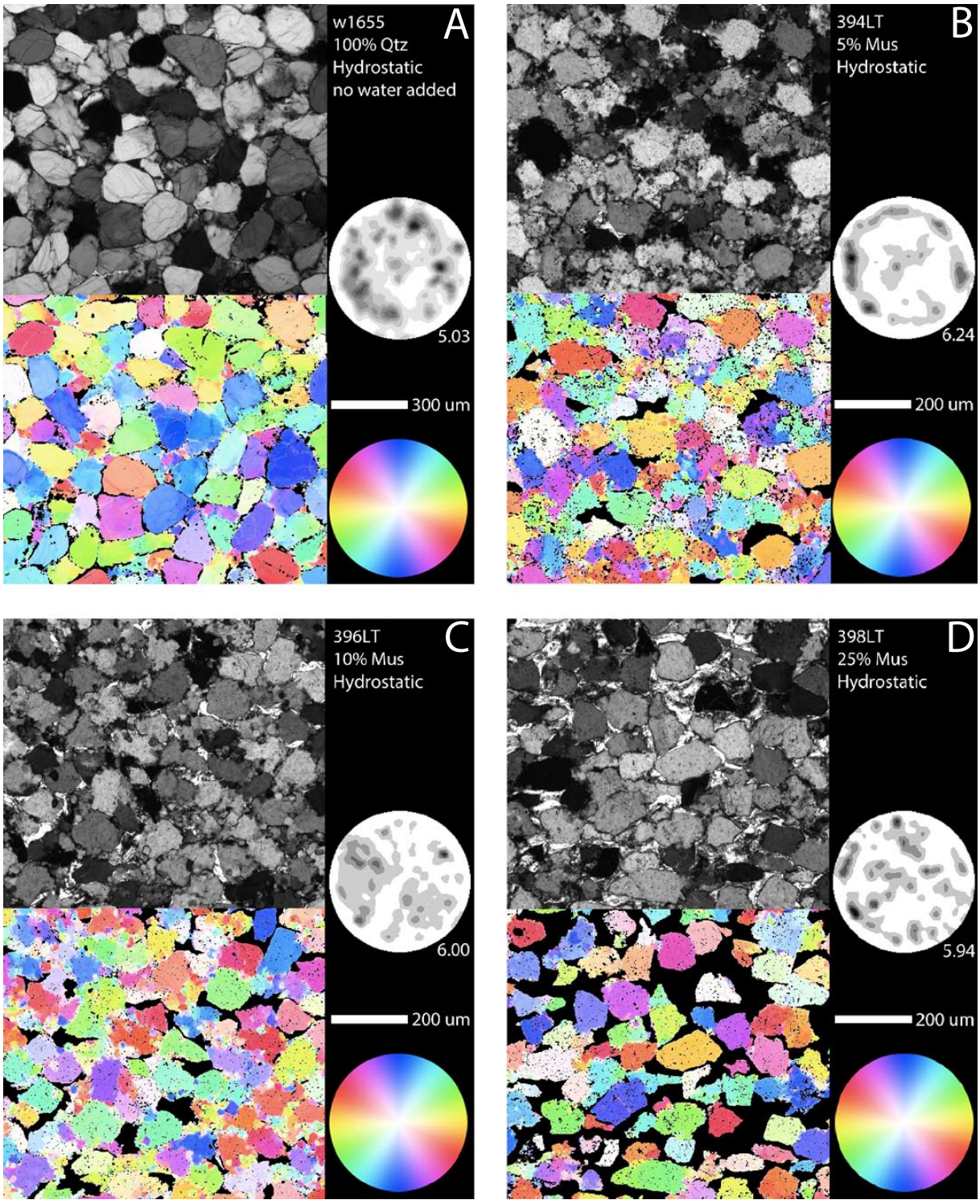

Figure 2.13 Circular polarized images (displayed in figure 2.3) together with CIP image for each circular polarized image below it displaying the quartz CPO. The color luck-up table (CLUT) is provided for each image to determine to orientation of each grain. The black regions in the CIP images are regions unwanted for measurement. Pole figures are constructed and displayed above the scale bar. Notice in b) and c) grain crushing is clearly visible in both the circular polarized and CIP images.

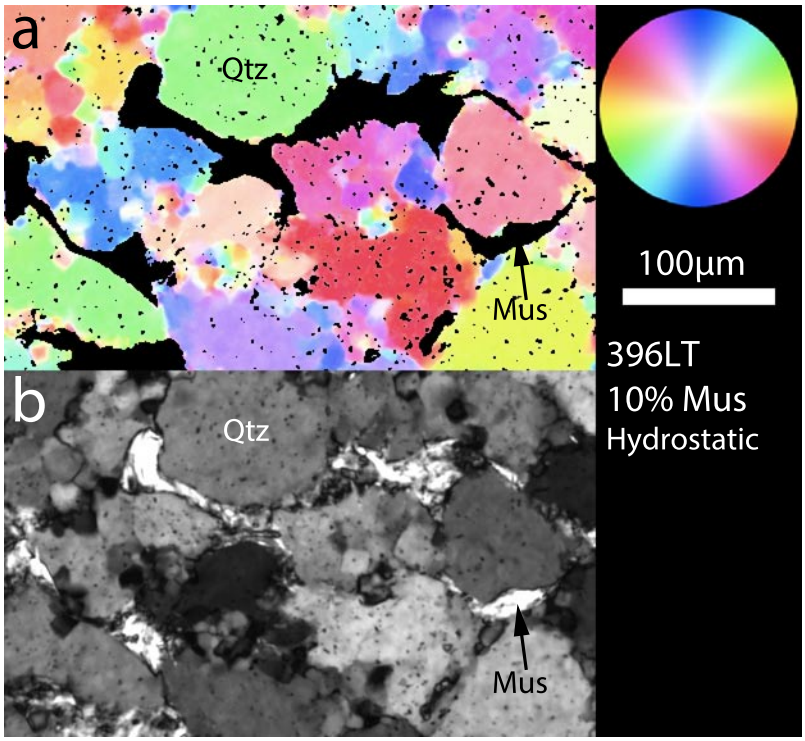

Figure 2.14 CIP image and circular polarized micrograph displaying the nucleation of crush quartz material in a hydrostatic experiment. The CIP image clear demonstrates there is no dependence of CPO on the newly grown quartz grains.

At peak stress conditions the 100% quartz sample displays a CPO that is oriented antithetic to the shear direction with two clustered regions. Each region contains two maxima and one region has a strong single maximum, figure 2.15a. At 5% muscovite, the sample displays a similar antithetic pattern with a strong single maximum with several randomly localized regions; likely related to the nucleation of crushed quartz material, figure 2.15b. At 10% muscovite, a single maximum is recorded in a similar orientation as the 5% muscovite sample, but otherwise displays a random texture, figure 2.15c. At 25% muscovite the pattern is similar to the 10% muscovite sample, with a single strong maximum, although the maximum is located ~20° counter-clockwise from the 5% and 10% muscovite CPO samples. The remainder of the CPO at 25% muscovite possesses a random orientation distribution, also observed in the 10% sample, figure 2.15d.

At steady state conditions the 100% quartz sample shows two equally strong maxima in a slightly asymmetric pattern in the direction of shear, figure 2.16a. At 5% muscovite, the CPO fabric also possesses two equally distributed maxima in the same orientation as the 100% quartz sample, but the maxima are weaker and more broadly distributed, figure 2.16b. At 10% muscovite, the quartz CPO displays a similar shape as the 5% muscovite sample, but at 10% muscovite there are two maxima whereas the 5% muscovite sample possessed a single maximum, figure 2.16c. At 25% muscovite, the

symmetry of the two maxima remains similar to the 5% and 10% muscovite samples with a single strong maximum, but there is a significantly more random distribution, figure 2.16d, resembling a broad coaxial quartz CPO.

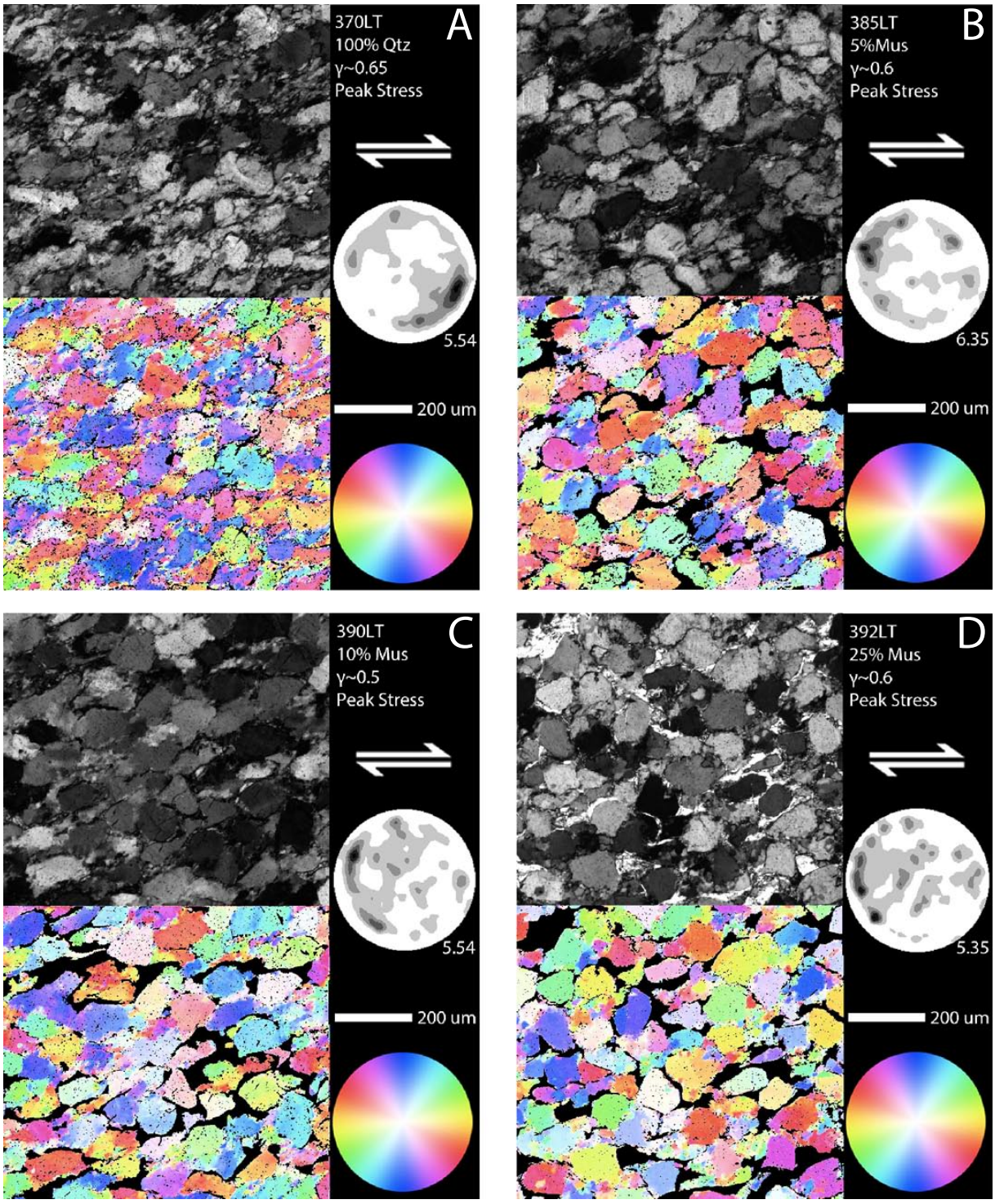

Figure 2.15 CIP images and pole figures for the four different peak stress experiments. Setup is the same as the hydrostatic images in figure 2.12.

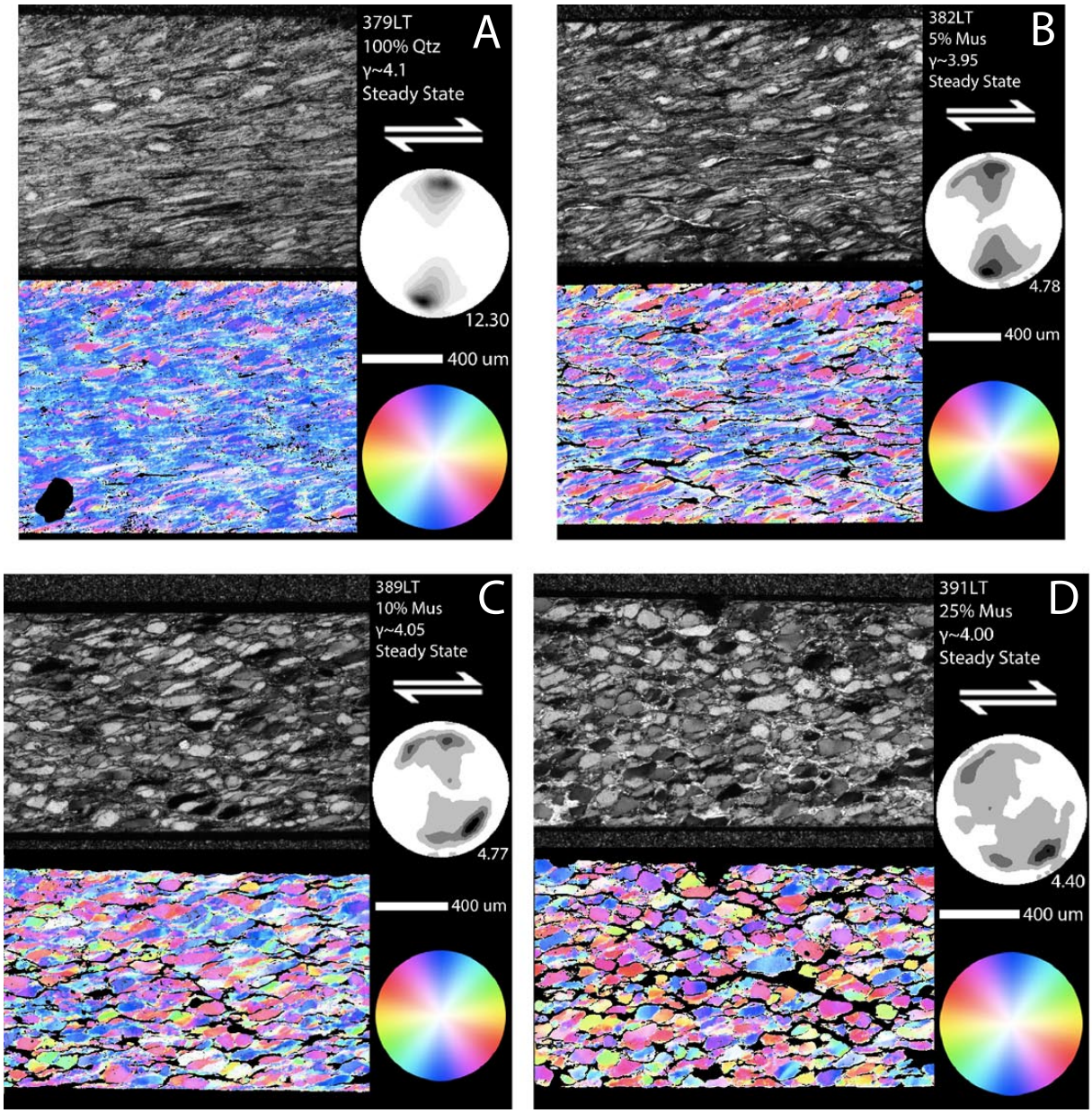

Figure 2.16 CIP images and pole figures for the four different steady state experiments. Setup is the same as the hydrostatic and peak stress images in figures 2.13 and 2.15 respectively.

2.3.4.2. Original CPO vs. Recrystallized CPO

To look more closely at the role of quartz recrystallization, CIP maps were constructed to analyze the CPO of just the original grains and the CPO of just the recrystallized grains in the four different steady state experiments (see Appendix B for CIP maps). This provides insight into the role of quartz recrystallization and how muscovite affects this process when deformed to high shear strains. Previous experimental studies on pure quartz aggregates attribute a coupling between dynamic recrystallization and CPO development as processes that lead to geometrical softening in quartz at high shear strains (Heilbronner and Tullis 2006; Muto et al. 2011). Another

experimental study observed that when muscovite was added to a pure quartz matrix, the volume of dynamic recrystallization in quartz decreased as the muscovite volume increased; by 50% muscovite-50% quartz there was little to no dynamic recrystallization in quartz within the aggregate deformed in axial compression (Tullis and Wenk 1994).

The pure quartz aggregate displays ~95% recrystallization and these grains contribute to the majority of the bulk CPO, while the original grains possess two broad maxima that are in an antithetic orientation to the shear sense; similar in shape to the 100% quartz peak stress CPO. The bulk, original, and recrystallized CPO pole figures are presented in figure 2.17. The CPO of the recrystallized grains at 5% muscovite contributes to the majority of the bulk CPO, similar to the 100% quartz sample. The original grains show the same pattern as in the 100% quartz sample where they are aligned for intracrystalline slip in the prism [c] orientation. At 10% muscovite, the CPO of the recrystallized grains possess the same CPO orientation as the original grains. This pattern is also observed at 25% muscovite. It is also important to note that the amount of recrystallization decreases as muscovite content increases, which is also observed in quartz-muscovite aggregates deformed in axial compression (Tullis and Wenk 1994). At 5% muscovite there is approximately 80% recrystallization in quartz, while at 10% and 25% muscovite there is 15% and 1-3% recrystallization, respectively.

In all of the peak stress and steady state samples analyzed, no sample displayed the development of a Ymax orientation and the dominant recrystallization mechanism observed is subgrain rotation (SGR).

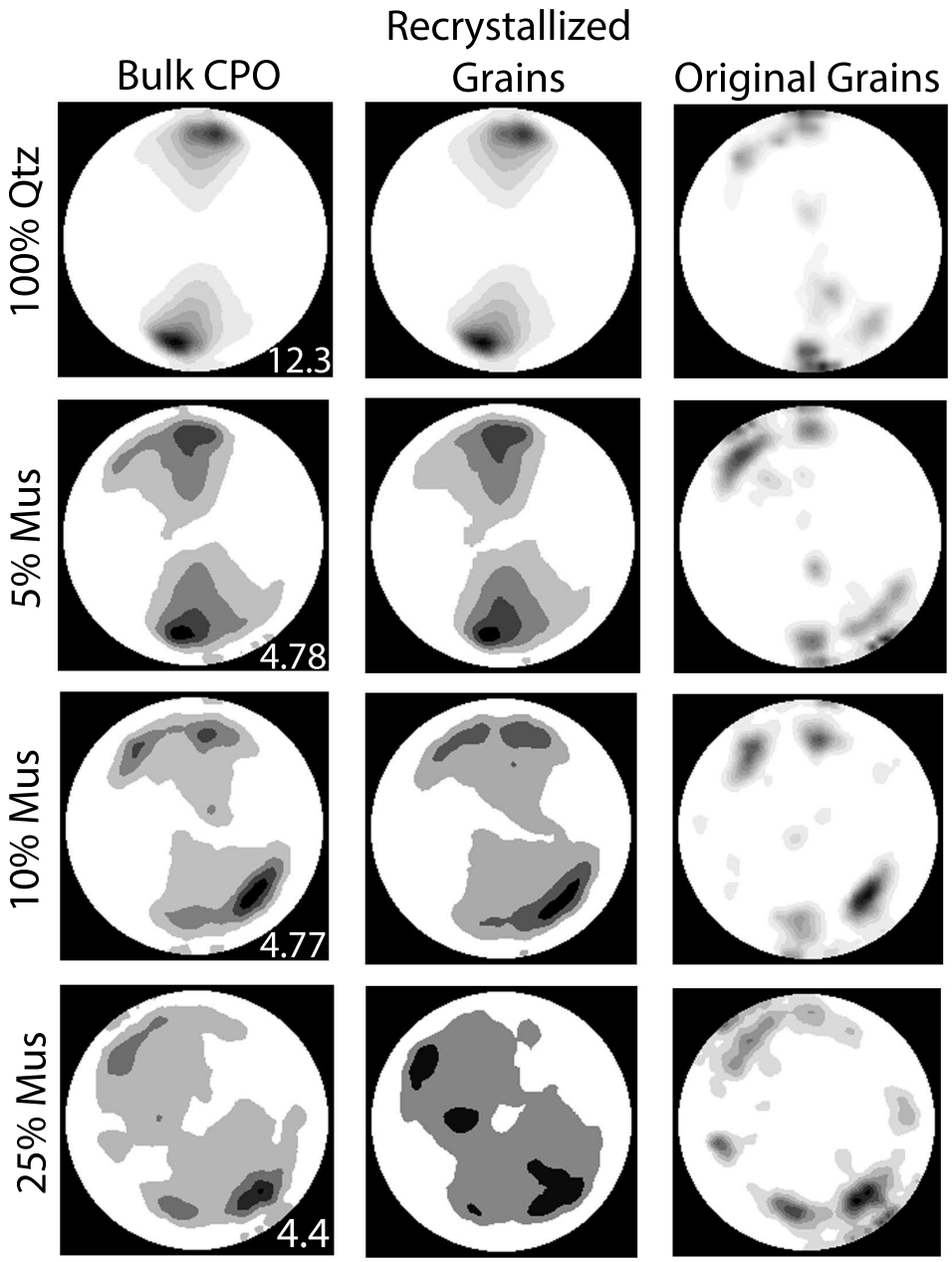

Figure 2.17 Quartz c-axis pole figures for each steady state experiment and c-axis pole figures for just the recrystallized and non-recrystallized grains. All pole figures represent a dextral sense of shear. The first column represents the bulk quartz CPO for each set of quartz and muscovite mixtures. The second column represents just the quartz CPO of the recrystallized grains and the third column is the CPO of just the original, non-recrystallized grains. The density contouring is 0.5 for all pole figures but it is important to realize that the volume percent of recrystallization is not equal in all experiments. There is estimated to be approximately 1-3% recrystallization at 25% muscovite where as in 100% quartz at steady state conditions there is approximately 95% recrystallized. This is why some of the contouring does not appear the same.

2.4. Discussion

2.4.1. Mechanical Data

A noticeable trend in the mechanical data is that all of the peak stress experiments are stronger than the steady state experiments for the equivalent volume percent of muscovite. The exact reasoning behind this observation is still unclear. The large difference in strength between experiments 370LT and 379LT is due to the

placement of the thermocouple (TC). The TC for the 100% quartz peak stress experiment has been documented to be at the sample-piston interface whereas the steady state experiment shows that the TC was located directly in the middle of the sample material. Alumina pistons have a high thermal conductivity and if the TC deviates away from the sample material it will alter the actual temperature the sample experiences. Alterations in sample strength can be noticeable if the TC position is not accurate enough. As for the three other sets of experiments, the TC positioning is reasonably located within the sample thickness. A possible explanation could be the starting distribution of muscovite for the 5% and 10% muscovite samples, where quartz is the controlling phase though it is impossible to know the actual distribution of muscovite at the start of the experiment although the work hardening slopes are very similar so it is difficult to justify muscovite distribution as the sole explanation; more experiments need to be run to resolve this issue. At 25% muscovite there is a clear decrease in the work hardening slope in relation to the other three sample mixtures. Note the two vertical lines in the two blue curves are electrical jumps recorded during the experiment. Although the slopes at 25% muscovite are different, the peak stress values are quite reasonable given the frictional error incorporated into a Griggs experiments. Holyoke and Kronenberg (2010) estimate at least ±50 MPa in frictional noise or error when NaCl is used as the confining medium. The peak stress for both the 25% muscovite samples are 83 MPa (391LT) and 96 MPa (392LT) including the electrical jumps, so these values seem reasonable for the low shear stress recorded. Experimental conditions and data are listed in Table 2.1.

2.4.2. SPO evolution

SPO measurements were conducted for each experiment where surface and particle analysis were conducted. At hydrostatic conditions, all samples displayed random orientations except at 25% muscovite there is a slight preferred orientation (figure 2.12). This is likely due to a lack of grain crushing and easy grain rotation during compaction and pressurization. During compaction, grain crushing is observed in all other aggregate mixtures and the edges of large quartz grains typically become rounded. In the case of 25% muscovite, the muscovite grains act as a “cushion” and prevent grain edges from crushing, which results in more angular grains, which appears to have altered the SPO at hydrostatic conditions. At peak stress conditions there is little

difference between the surface or particle analyses but at steady state conditions there is a distinct difference. At steady state conditions the 100% quartz and 5% muscovite sample show similar surface and particle analyses while at 10% and 25% muscovite there is alteration in the SPO of the quartz grains. This alteration, a decrease in aspect ratio and particle alignment, is directly related to strain partitioning into muscovite grains resulting in less plastically deformed quartz grains. Lisle (1985) concluded that there was no distinct relationship between the aspect ratio of quartz grains and the percent of secondary phases. Based on the SPO results from this study, at low shear strains our results agrees with the findings of Lisle (1985) where there is no distinct relationship between the aspect ratio and volume percent of secondary phases, however, at higher strains the aspect ratio appears to be better at distinguishing between the four different aggregate assemblages and this is most likely attributed to the amount of strain partitioning over the length of the deformation and the mechanical transition between LBF and IWP of the aggregates.

2.4.3. CPO evolution

The evolution of the bulk CPO in the 100% quartz aggregate start at a random distribution then at peak stress conditions prism [c] orientations are observed and by steady state conditions rhomb <a> orientations have been developed. These results are in agreement with quartz CPO results produced by Heilbronner and Tullis (2006). When muscovite is added to the aggregate it has no effect on the CPO at hydrostatic conditions. At peak stress conditions the 5% muscovite shows slight weakening of the overall distribution but at 10% and 25% muscovite, the CPO distribution is close to random with a single maximum in a similar orientation to the 5% muscovite sample. This increased weakening of the CPO fabric for the 10% and 25% muscovite samples is attributed to strain partitioning into weaker muscovite grains.

At steady state conditions, the presence of muscovite can be observed altering the quartz CPO. At 5% muscovite, the two maxima become much more distributed than in the 100% quartz CPO sample at steady state conditions. At 10% muscovite the general shape of the CPO orientations are similar to the 5% muscovite sample but now multiple maxima are observed. By 10% muscovite, the orientation of the two opposing maxima are rotated approximately 20° against the direction of shear in relation to the orientation of the two maxima in the 100% quartz steady state sample (figure 2.17).

Finally, at 25% muscovite the bulk CPO has rotated over 45° from the 100% quartz sample and displays a similar shape to the 5% and 10% muscovite samples at steady state conditions. To explain the rotation of the two CPO maxima against the direct of shear as the percent muscovite increases can be explained when examining the CPO of the original and recrystallized grains.

At 100% quartz, the recrystallized grains rotate in the direct of shear and develop rhomb <a> orientations, while the CPO of the original grains closely represents the prism [c] orientations observed in the 100% quartz peak stress experiment. The development of quartz CPO at high strains is in agreement with previous work on experimentally deformed quartz at 900°C (Heilbronner and Tullis 2006; Muto et al. 2011). All of the original quartz grains at steady state conditions possess the same prism [c] orientations, regardless of the amount of muscovite content (figure 2.17). At 5% muscovite, there is still a difference between the CPO of the recrystallized quartz grains and the CPO of the original grains where the recrystallize grains show a broad range of orientations; rotation in the direction of shear is observed though not all recrystallized grains rotate. By 10% muscovite, the CPO of the original grains matches exactly the CPO of the parent grains, in the prism [c] orientation. This is also observed in the 25% muscovite sample. This change in CPO of recrystallized grains illustrates strain partitioning in the aggregate and the mechanical transition between LBF and IWP. From these results both SPO and CPO demonstrate the transition from LBF to IWP. It is also important to understand that the amount of recrystallization in quartz drastically decreases from the 10% to 25% muscovite, where only 1-3% recrystallization is observed in the 25% muscovite sample while in the 100% quartz sample there is ~95% recrystallization. This result agrees with the axial compression experiments performed by Tullis and Wenk (1994). As a result of strain partitioning effecting the CPO orientations, at 10% and 25% muscovite the CPO of the quartz grains no longer represent a typical simple shear CPO geometry and more closely represents axial compression (Schmid and Casey 1986). This is an important result for applying quartz CPO data as an indicator for deformation geometry or shear sense indicator when muscovite is present at volume presents above 5%.

Numerical models studying texture development show agreement with the CPO development up to peak stress (Jessell 1988; Lister and Paterson 1979); although when the aggregate recrystallizes the models cannot replicate the rotation of the c-axes with

the sense of shear in the 100% quartz aggregate (figure 1.9). Even the model proposes by Jessell (1988) to incorporate the process of recrystallization will not allow the c-axes to rotation through the shear plane and so numerical models appear limited to low strain deformation in the shear geometry.

2.4.4. Transition from Load-bear Framework supported to Interconnection the of weak phase

The transition from quartz-dominated (LBF) to muscovite-dominated (IWP) aggregates occurs between 10% and 25% muscovite in the experiments performed in this study in the shear geometry. This result is in agreement with a previous study on synthetic quartz-muscovite aggregates performed in coaxial deformation where this transition occurs between 10% and 15% muscovite (Tullis and Wenk 1994). At 5% muscovite in the aggregate, muscovite grains are largely isolated from each other at hydrostatic and peak stress conditions. At steady state conditions, muscovite grains wrap around quartz grains and in some cases arrest recrystallization due to strain partitioning. In the highest region of displacement in the sample at the sample-piston interface C' shear bands can be observed where shear bands slip on connected muscovite grains (figure 2.7). The development of these C' shear bands is interpreted as the dominant mechanism to aid redistribution of muscovite throughout the aggregate during deformation and weakening the aggregates bulk strength.

At 10% muscovite, the muscovite grains can be locally interconnected but not globally connected. At 10% muscovite, the aggregate is in a transition between quartz-dominated and muscovite-dominated and several microstructural features are observed that provide insight into how muscovite is distributed throughout the aggregate during deformation. C' shear bands are observed throughout the entire aggregate at various angles to the shear plane. Unlike the 5% muscovite sample where all of the shear bands slipped on muscovite grains, at 10% muscovite, there are several shear bands that are defined by small, 1-3μm, granular quartz grains and void spaces (figure 2.9 label 4). This result agrees with Holyoke and Tullis (2006) where stress concentrations are observed at the tips of biotite grains promoting semi-brittle flow in the neighboring quartz grains, allowing biotite grains to become interconnected. Void spaces were also documented in a natural micaceous quartzite shear zone where void spaces were observed and produced at high confining pressures (Hippertt 1994). Hippertt (1994) predicted that these void spaces were developed because of the fluid pressure between the quartz

grain boundaries and that these void spaces were crystallographically controlled and micas would precipitate into these void spaces, which would promote fast distribution of muscovite throughout the shear zone during deformation. Based on our work so far, we cannot conclude whether these void spaces are related to crystallographic orientations but our experiments do have added water and muscovite can be observed precipitating into the void spaces, which agrees with the processes presented by Hippertt (1994).

By 25% muscovite, the muscovite is globally interconnected throughout the aggregate prior to deformation. C' shear bands are visible at high strains, but are only identified at the sample-piston interface in the region of high sample displacement, similar to the C' shear bands in the 5% muscovite sample. At 25% muscovite, there is significantly less deformation observed in the quartz grains, with 1-3% recrystallization. This result agrees with the microstructures observed in the coaxial experiments with similar aggregate percentages for muscovite and quartz (Tullis and Wenk 1994). Editing the masks from the CIP procedure for the three steady state experiments containing muscovite (figure 2.18) provides a visual of the development of muscovite grains throughout the aggregate as the muscovite partitions the majority of the strain in the sample and causes the transition from LBF to IWP; the white regions are muscovite and the black regions are quartz. We predict that if these experiments were able to continue to deform to higher shear strains that the muscovite would align into a single weak layer or zone and become a simply connected system.

A transition between the LBF and the IWP can be observed showing variations in strain accumulation throughout the sample. In the steady state pure quartz sample there is significant variation in strain accumulation between different regions within the sample, related to the amount of displacement experienced throughout the deformation. At 5% muscovite, the sample still displays a strain variation, which is an indication that quartz is still the dominantly controlling phase while at 10% and 25% muscovite there is no strain variation observed throughout the sample and deformation appears homogeneous. This indicates that quartz is no longer the dominantly controlling phase. This difference in variation of strain is likely due to strain partitioning into muscovite and not the quartz.

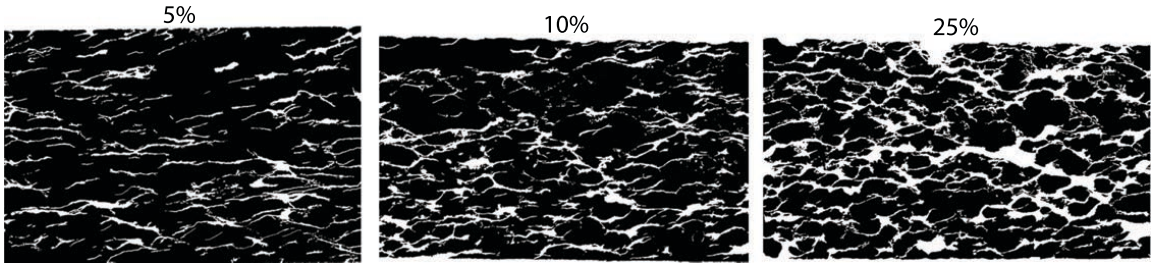

Figure 2.18 Illustrations of muscovite distribution throughout the aggregate within the three steady state experiments that contained muscovite. The white regions represent muscovite and the black regions are quartz. The shear plane is horizontal to the frame of the picture and the sense of shear is dextral.

2.4.5. Application to large-scale tectonics

A recent theoretical study by Montesi (2013) posits that strain localization has the greatest potential of occurring when there is a large strength difference between the different phases within a rock and when the weakest phase, e.g. muscovite or biotite, possesses a nonlinear rheology. Two numerical studies have modeled crustal shear zones in nature to determine how secondary phases can influence the viscosity and bulk strength of the rock (Gerbi et al. 2010;Johnson et al. 2004). All three of these studies state the importance of the interconnection of the weakest phase initiating and controlling strain localization and shear zone development. Johnson et al. (2004) observes that the weakest phase, biotite, in a tonalite pluton, develops localized microfractures when the aggregate is supported by the load-bearing phase, feldspar, and these microfractures evolve into ductile shear zones where strain is localized. This result agrees with the redistribution of muscovite along shear bands and precipitation into void spaces defining muscovite-poor shear bands (figure 2.9). Gerbi et al. (2010) constructed viscosity maps through a numerical model to illustrate the development of strong and weak layers in naturally deforming shear zones at the meter to kilometer scale (figure 2.19). The results of this model are in strong agreement with phase maps produced from the steady state experiments in this study (figure 2.18), where the weak phase aligns in an anastomosing pattern.

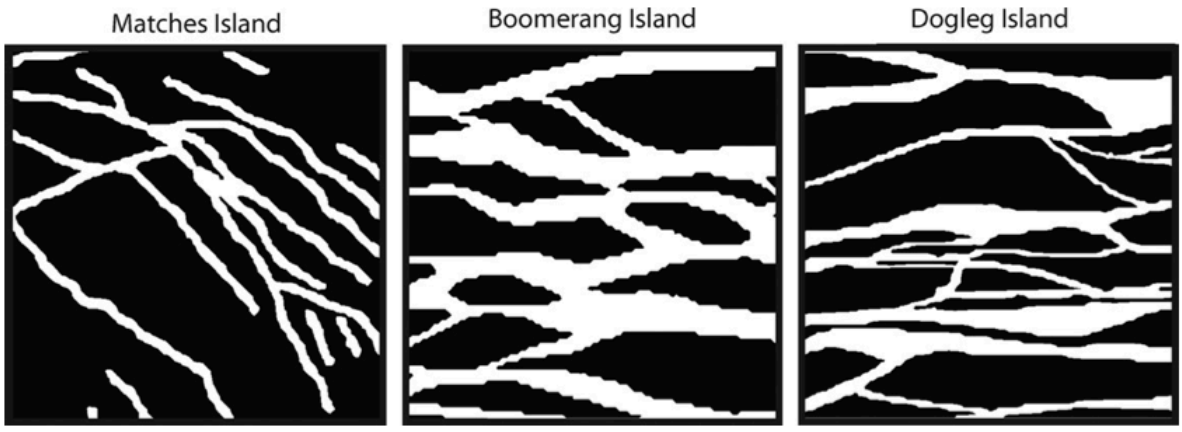

Figure 2.19 Viscosity maps developed by Gerbi et al. (2010). The similarity between the phase distribution maps produced for this study in figure 2.18 are in strong agreement in how the weak and strong phases for both studies distribution themselves in shear deformation. (modified from figure 7 of Gerbi et al. (2010)).

The results of this study demonstrate processes at the micro-scale can influence the development of large-scale tectonic structures throughout the crust. These studies (Gerbi et al. 2010; Johnson et al. 2004; Montesi 2013), as well as the observations by Hippertt (1994) show strong agreement with not only the result of weakening of the bulk aggregate when higher volume percentages of a weaker phase are added but the mechanisms that cause this weakening are in agreement with both the experimental results of this study and the study conducted by Holyoke and Tullis (2006), which provides validity for replicating deforming processes observed in natural in the experimental laboratory.

2.4.6. Work to be continued

This study provides evidence for the distribution of muscovite throughout the aggregate with different volume percentages of muscovite and quartz. It would also be influential in understanding the effects of grain size between the two phases as well as phase distribution (Handy 1990; 1994). The development of a method that would be able to quantify phase distribution would be extremely useful for not only muscovite-quartz aggregate but also all bi-phase mineral assemblages. Currently the Zener parameter is used as quantifiable the maximum stabilize grain size but provides no evidence on the anisotropy of the secondary phase and it limited by the geometrical parameters of the equation, further work on these topics would provide valuable insight in deformation of polymineralic rocks.

2.5. Conclusion

A series of experiments were conducted to investigate the role muscovite plays in affecting the fabric development of quartz deformation at dislocation-creep conditions to high shear strains. Mechanically, the addition of muscovite weakens the overall strength of the aggregate where muscovite-present aggregates show little to no mechanical weakening once peak stress conditions are reached. At 10% muscovite, the sample is approximately half as weak as the 100% quartz sample and at 25% muscovite; the sample becomes over 3.5x as weak as the 100% quartz sample.

The development of C' shear bands and dissolution-precipitation processes lead to the redistribution of muscovite throughout the aggregate while deformation is active. C' shear bands are observed to slip on both muscovite grains as well as quartz grains, where the quartz grains are coupled with void spaces, and where muscovite can be observed to precipitating into these void spaces. Regions of quartz recrystallization are also locations were muscovite can be observed precipitating into due to an increase in the grain boundary pathways.

Microstructural observations of quartz show that recrystallization is dominated by subgrain-rotation recrystallization and that grain boundary migration is not active at 800°C. At phase boundaries with muscovite, quartz grains can recrystallized but due to strain partitioning, quartz grains often do not. The transition from a load-bearing framework (LBF) supported aggregate to an interconnected weak phase (IWP) aggregate in shear occurs between 10% and 25% muscovite. By 25% muscovite within the aggregate, muscovite is the dominantly controlling phase while at 5% muscovite quartz is still the dominant phase and 10% muscovite the aggregate is in a transition phase.

The bulk CPO for pure quartz transitions from a random orientation at hydrostatic conditions, to prism [c] at peak stress, and to rhomb <a> at steady state conditions. When muscovite is added to the aggregate, strain partitioning into muscovite prevents newly recrystallized quartz grains from rotating into the rhomb <a> orientation. At 10% and 25% muscovite rhomb <a> is not achieved and recrystallized grains remain in a similar, prism <c>, orientation as the original quartz grains.

CHAPTER 3: End-member models to describe strain localization in shear zones

3.1. Introduction

The localization of deformation, in particular, the development of shear zones is of particular interest because shear zones can often be used as recorders of deformation history in regions of high strain deformation within the earth. Theoretical models (Hull 1988, Means 1995) have been proposed describing different types of evolving shear zones as a function of shear zone thickness and time. The type 2 model presented by both Hull (1988) and Means (1995) considers a thinning shear zone over time where the most actively deforming zone thins with time. This type of shear zone is expected for strain-softening materials. Other shear zones have been presented where the finite amount of shear strain changes continuously and is often characterized as possessing a sigmoidal foliation (Ingles 1983; 1985; 1986). These theoretical models by Ingles (1983; 1986) were used to investigate how finite principle strains and passive markers were affected when a pure shear component was applied to a perfect simple shear scenario.

Simpson (1983) describes how finite strain is distributed within a natural shear zone and how strain varies from the shear zone termination to the high strained regions of the shear zone.

These theoretical models are often quite simple and can only provide a measure of strain after deformation has arrested and offers no insight into possible mechanisms that can cause shear zones to form and why strain localizes in these zones. Several mechanisms have been proposed to promote strain localization in monomineralic materials (Poirier 1980 and White et al. 1980). One such mechanism is geometrical softening, where weakening of the material is due to a specific crystallographic orientation within the grains. This alignment of CPOs promotes anisotropy within a certain region of the rock that creates a decrease in the effective viscosity of the zone allowing for strain to localize and develop into a shear zone. Studies from theoretical and numerical models have often discussed and postulated the idea of geometrical softening in various materials (Wenk et al. 1991; Tommasi et al. 2009) with few experimental studies to draw from. Geometrical softening in experimental work on metals has been discussed previously (Harren et al. 1988), but only recently has experimental work been conducted on earth materials, in particular, quartz (Muto et al. 2011). Muto et al. (2011) posits that transitions in c-axis orientations can lead to anisotropy in grains based on their CPO orientation. They observe the development of Ymax orientations at high shear strains that promote geometrical softening and strain localization. These results on single crystal quartz experiments preformed by Muto et al. (2011) are in agreement with the experimental results on polycrystalline quartz conducted by Heilbronner and Tullis (2006); who also associated the development of Ymax c-axis orientations as a weak orientation where strain localizes within their samples performed to high shear strains. Natural and analogue studies also show a transition of CPO with progressive shear strain when recrystallization has occurred. Norcampfor shear experiments show the development of Ymax orientations at high shear strains while natural shear zones in Cap de Creus show transitions in CPO development (Carreras et al. 1977; Herwegh and Handy 1996). Based on the conditions of these experiments, the development of Ymax orientations for quartz c-axis is indicative of high temperature deformation. At lower temperatures the development of Ymax orientations at high strains does not occur (Tullis and Heilbronner 2002 and references therein). Natural studies of shear zones where quartz fabrics show

transitions in CPO with progressive shear strain also shows strain localization without the development of Ymax orientations (Carreras et al. 1977). It is clear from these studies that geometrical softening and strain localization is related to a transition of CPO orientations and recrystallization but questions still remain as to how strain is distributes throughout a developing shear zone? And how can this information be applied to natural shear zones?

The development of the recrystallized grain-size piezometer (Twiss 1977) has allowed for the extrapolation of flow stresses in different tectonic settings based on the recrystallized grain size of various materials. Modified versions of the original recrystallized grain size piezometer have been produced, and Stipp and Tullis (2003) have developed a recrystallized grain size piezometer for dislocation creep in quartz. This same quartz grain size piezometer is also correlated to roughly estimate the different quartz recrystallization mechanisms proposed by Hirth and Tullis (1992). In the experiments performed by Heilbronner and Tullis (2006) they measure different recrystallized grain sizes in experiments they assume reach steady state conditions and associate this variation not to differences in flow stress, but rather to CPO orientation, where recrystallized grains in the Ymax orientation produced the largest recrystallized grain sizes in relation to other know quartz CPO orientations. These same experiments as well as the experiments performed by Muto et al. (2011) argue that the localized zone of deformation observed in their experiments at high shear strains is due to an increase in strain rate in these localized regions. These results indicate that the recrystallized grain size could be dependent not only on the flow stress of the sample, but strain rate as well CPO orientation. The paleowattmeter is a scaling law that presents a relationship where the equilibrium grain size is proportional to the product of flow stress and strain rate (Austin and Evans 2007). Little work has been conducted experimentally to provide validation of whether there is a dependence of strain rate on the recrystallized grain size in deformed materials at steady state conditions and their application for natural deformation.

This study aids to analyze two end-member models on the development of shear zone formation in the framework of the paleowattmeter from general shear experiments preformed in a modified-Griggs apparatus. The use of experimentally deformed synthetic quartz powders will allow us to make quantitative relationships within the samples as well as draw relationships on previously conducted samples of similar

material in relation to better understand how localization can develop and whether grain size is affected by variations in strain rate.

3.2. Experimental methods

Three experiments of 100% quartz powder with a grain size range of 63-100 μm were preformed to hydrostatic, peak stress ($\gamma \sim 0.7$), and steady state ($\gamma \sim 4$) conditions in the shear geometry in a modified-Griggs apparatus (figure 3.1). Each experiment contained 0.1wt% water and was performed at 800°C and 1.5 GPa. Thin sections were cut perpendicular to the shear direction and polished to first-order grey values for the mineral quartz. Measurements for the individual models derive from the mechanical data or optical observation using a petrographic microscope while quartz CPOs were calculated using computer-integrated polarization (CIP) microscopy (Panozzo Heilbronner and Pauli 1993; Heilbronner and Tullis 2006). Further information of the setup and materials for an experiment can be found in section 2.3 and appendix A.

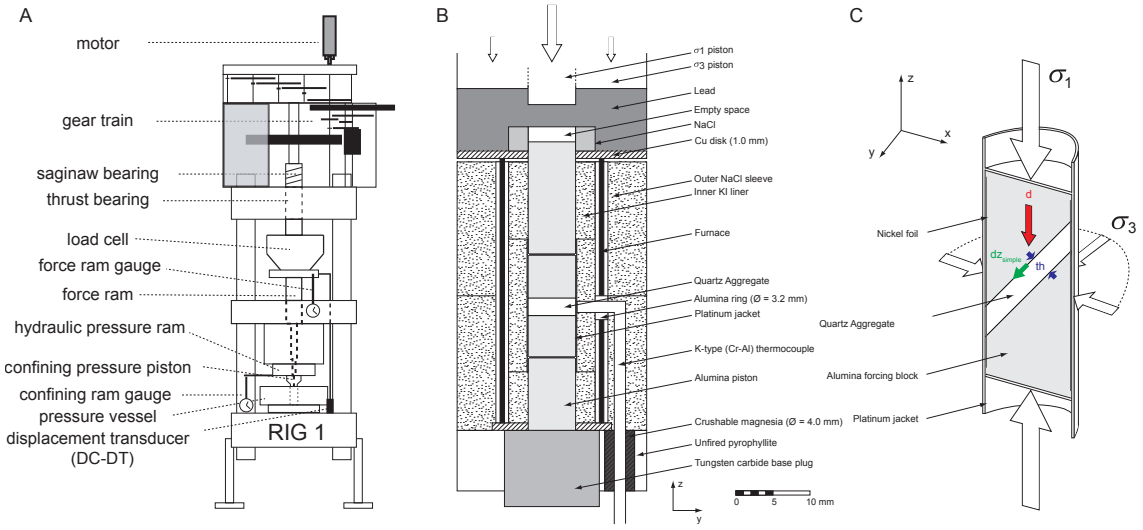

Figure 3.1 Schematic illustrations of a) modified Griggs-apparatus, RIG 1 at the University of Tromsø b) sample assembly inserted into the pressure vessel and c) the jackets samples in the shear geometry. Figure modified after Tarantola et al. (2010).

3.3. Microstructures

At hydrostatic conditions, quartz demonstrates slight grain crushing at the grain boundaries and no undulose extinction, indicating that no dislocation activity within the grains occurred during pressurization or while at hydrostatic conditions. Grains often show internal microcracking due to both compression and decompression of the sample; microcracks related to decompression are often all orientated with opening Mode 1 type crack in the orientation of the driving sigma 1 piston. Grains are found to

possess both round and sharp edges, (figure 3.2), and some instances growth of new grains nucleating from the crushed material at the grain boundaries can be observed.

At peak stress conditions, there is approximately 10% recrystallization with a recrystallized grain size of 8-15μm, though many of these grains are interpreted to result from nucleation from crushed material during compaction and pressurization, similar to descriptions by Muto et al. (2011). Internal deformation structures, such as subgrains, undulose extinction, and deformation lamellae are apparent in grains, indicating dislocation processes are active at peak stress conditions. Several grains display internal recrystallization, likely due to microcracking during pressurization while the majority of the grain boundaries of the original grains are highly serrated. The aggregate displays homogeneous deformation throughout and possesses a foliation defined by the SPO of the original grains at approximately 25° to the shear plane. Slight thinning of the sample is observed.

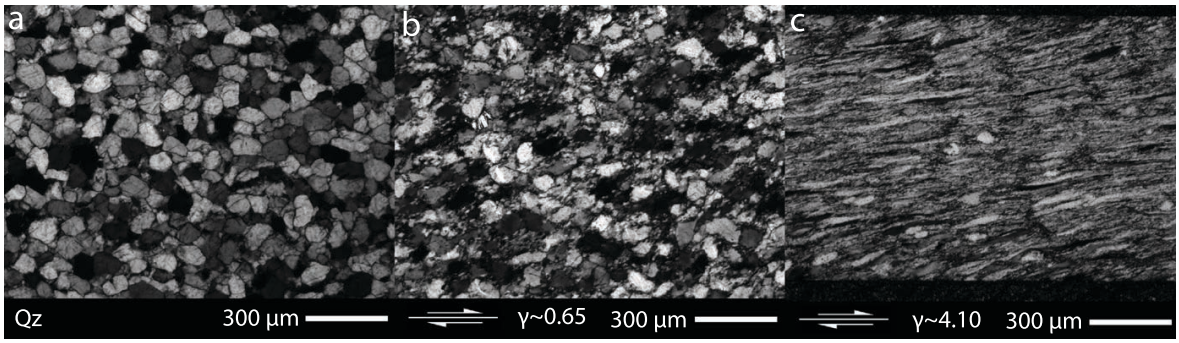

Figure 3.2 Photo micrographs of 100% quartz powder using a circular polarizer a) hydrostatic b) peak stress and c) steady state conditions for 800°C and 1.5 GPa. Shear plane is horizontal to the frame of the picture.

At steady state conditions, the aggregate is approximately 95% recrystallized with a very strong foliation defined by the SPO of the original grains, approximately 15° to the shear plane, but can vary depending on the local finite strain accumulated within the sample. Deformation structures such as subgrains, undulose extinction, and deformation lamellae are easily observed throughout the entire aggregate with the majority of the grain boundaries serrated. This indicates that dislocation processes are active throughout the aggregate. A variation in accumulated strain within the sample is observed in two oppositely opposing ends of the sample where accumulated displacement throughout the experiment is near zero, these two regions possess low strain in comparison to the rest of the sample (figure 2.6). In these two regions there is significantly less strain accumulated in the microstructures demonstrated by less recrystallization and a higher foliation angle to the shear plane, ranging from 20-40° to

the shear plane, while the sample thins approximately 20%. Both the peak stress and the steady state experiments show an increase in the angle of the foliation at the sample-piston interface regardless of accumulated strain. The difference between the differential stress of the peak stress and steady state experiments can be attributed to the positioning of the thermalcouple (TC), where the positioning of the peak stress TC is much closer to the sample piston interface than the steady state experiment. This offset of the TC creates a larger thermal gradient over the sample volume producing an experiment that experiences lower temperatures throughout, in comparison to an experiment where the TC is clearly located within the sample thickness. An experiment that experiences a higher thermal gradient produces higher differential stresses because at cooler temperatures materials are typically stronger (figure 3.3).

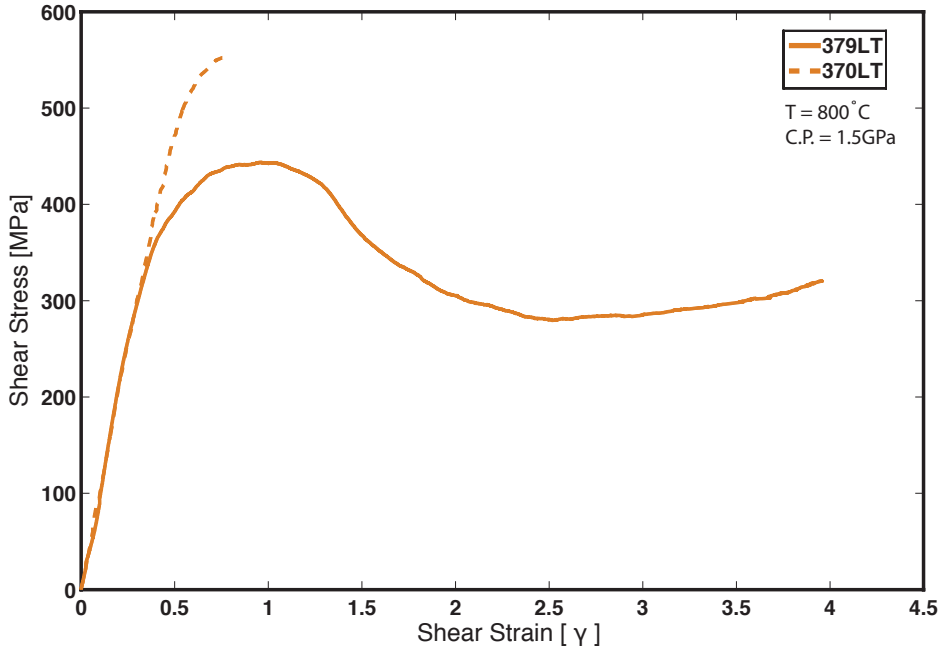

Figure 3.3 Stress–strain curves for peak stress and steady state experiments for 100% quartz in the shear geometry at 800°C, 1.5GPa, and shear strain rate of ~ 10^{-5}(s^{-1}).

Table 3.1 *Synthetic quartz deformed in general shear at T=800 ℃ and P_c=1.5 GPa*

Experiment#	$\dot{\gamma}$(s^{-1})	γ	Thinning (%)	Time (sec)
370LT	1.25e-5	0.75	5	60121
372LT	-	-	0	122445
379LT	9.42e-6	3.95	20	420395

3.4. Finite strain and strain profile

A cross-sectional area of approximately 400μm by 960μm at one end of the steady state experiment where a strain gradient is observed is used to calculate the finite strain across the section of the shear zone. This cross-sectional area is where all measurements were derived for the two different models. Equation 3 was developed by Ramsey & Graham (1970) and can be used to determine the finite strain across the thickness of the shear zone based on the angle of the foliation to the shear plane, which is defined as the sample-piston interface. Because there is slight alteration of the foliation at the sample-piston interface, the finite strain is not calculated for these regions. Another equation presented by Ramsey and Graham (1970) allows the calculation of the local finite shear strain across zone based on the known displacement of the shear zone, in this case, the shear displacement of the sample, assuming the top and bottom shear pistons were perfectly aligned at the start of deformation, equation 4. Combining these two equations, a strain profile was constructed for the cross-sectional area of the sample. Both models apply this strain profile and cross sectional area to draw finite strain and microstructural values from, which assumes that both models possess the same strain profile and same bulk strain accumulation. A similar treatment of these two equations (1,2) can be found in both natural and theoretical work on shear zones, respectively (Simpson 1983; Ingles 1986).

$$\gamma = \frac{2}{\tan 2\theta} \tag{3}$$

$$S = \int_0^x \gamma dx \tag{4}$$

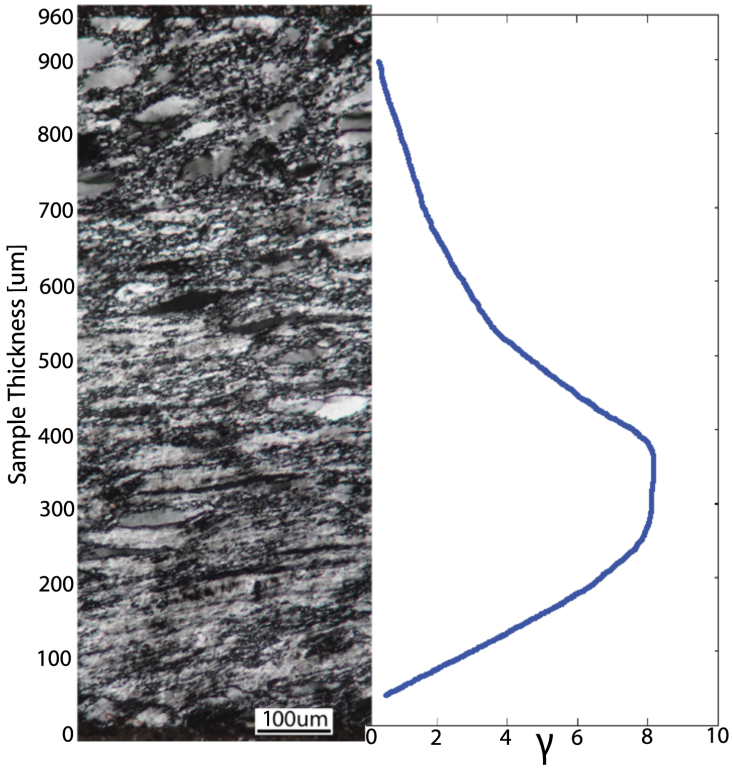

Figure 3.4 Microstructural cross section of strain gradient in 100% quartz steady state experiment (379LT). Blue line represents the calculated finite strain profile for this microstructural cross section with a maximum gamma of ~8. Photo micrographs taken using crossed polarizers and the shear plane is horizontal to the frame of the picture.

From the resulting strain profile, (figure 3.4), there is a large distribution of finite strain across the sample section. The bulk strain of the sample recorded by the mechanical data is $\gamma \sim 4$ while the strain profile created based on equations (3,4) displays a distribution of finite strain above and below $\gamma=4$ ranging from $\gamma \sim 0.25$ to $\gamma \sim 8$. The finite strain reaches a flat maximum in a ~200μm zone and steadily decreases to the edges of the sample above and below this zone.

3.5. End-member models

The two end-member models are described below. Both are derived based on microstructural elements within the cross sectional area in (figure 3.4). Figure 3.5 is a schematic of the two different models described below.

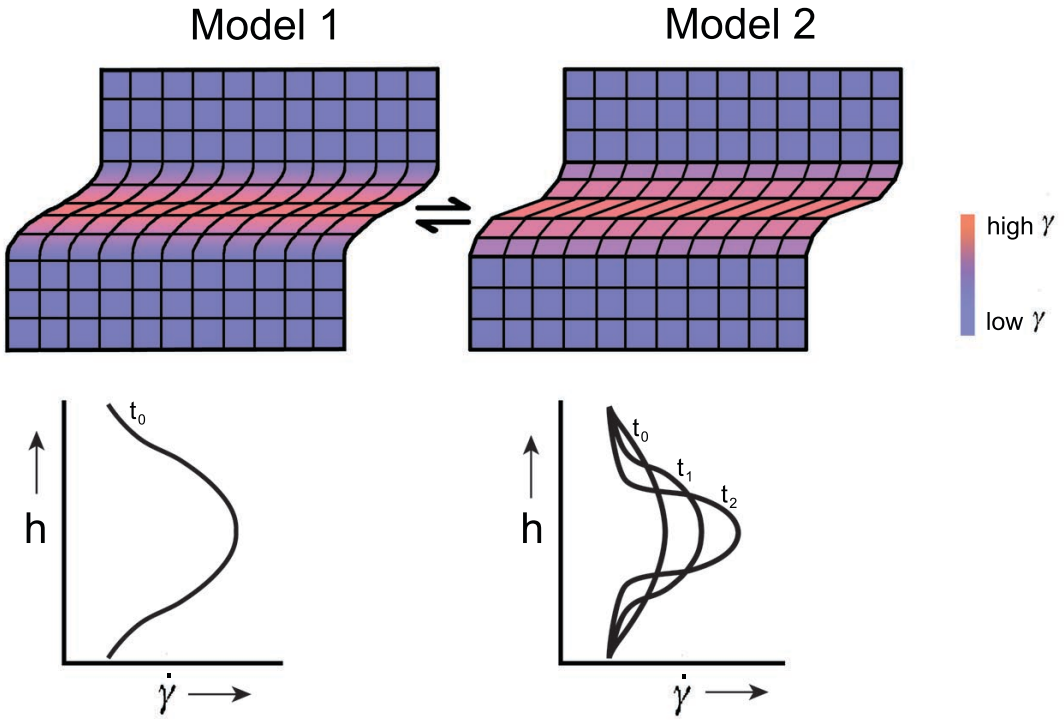

Figure 3.5 Two end-member models for strain localization in a shear zone. The block models for both Model 1 and Model 2 are quite similar because the same strain profile is used to describe both models. Model 1 applies the assumption that strain rate is highest at the core of the shear zone and continuously decreases to the periphery of the shear zone. Deformation is assumed to be active throughout the entire shear zone during deformation so the strain rate profile should remain in the same shape throughout the deformation history. Model 2 applies the assumption at deformation localizes over time and that when deformation localizes the strain rate should increase. t_0, t_1, and t_2 represent different time periods of localization where the inflection point is the transition from actively deforming to regions of grain growth.

3.5.1. Model 1:

Model 1 represents a shear zone that localizes through a gradational decrease in strain rate from the core of the shear zone, possessing the fastest strain rates, to the near undeformed regions of the shear zone, possessing the slowest strain rates. Model 1 assumes that deformation is active throughout the entire shear zone and that the shear zone is deforming throughout the entire deformation period. Regions that deform at faster strain rates will produce smaller recrystallized grain sizes based on the scaling relationship of the paleowattmeter. Because the paleowattmeter assumes there is little to no stress gradient within the system, a weakening mechanism, such as geometrical softening, must contribute to the initiation of localization of strain during the deformation.

For model 1, three regions were constructed: low strain ($0 \leq \gamma \leq 2$), medium strain ($2 \leq \gamma \leq 4$), and high strain ($4 \leq \gamma \leq 8$) from the cross sectional area of the shear zone, figure 3.4. The average grain size was determined in each region and plotted on the quartz recrystallized grain-size piezometer by Stipp and Tullis (2003) to determine the

approximate flow stresses for each region (figure 3.5). Plotting the calculated flow stresses in the Hirth et al. (2001) flow law for quartz, with a water fugacity of 4844 GPa and where Q=135 [kJ/mol], m=1, and n=4 allows for extrapolation of shear strain rates for the different individual regions, (figure 3.6), table 3.2. The value for water fugacity was calculated based on equation 3,

$$\ln f = \left[\ln \rho + \frac{A^{res}}{RT} + \frac{P}{\rho RT} \right]_{P,T} + \ln(RT) - 1 \qquad (5)$$

where f is fugacity, A^{res} is residual Helmholtz energy, ρ is molar density (n/V) and P, T, R are pressure, temperature and the universal gas constant, respectively (Pitzer and Sterner 1994; Sterner and Pitzer 1994). The values for Q, m, and n are the same values determined by Hirth et al. (2001). Since the model assumes that deformation is active throughout the entire shear zone, the total time of the experiment is used to back calculate the shear strain rate to a shear strain for each region. Applying the shear strain to equation 4, a calculated displacement can be achieved for each region and can then be summed to produce an approximate total displacement for the shear zone under these constraints, table 1.

The total displacement of the experiment, 3840μm was measured from the offset of the shear pistons using a light microscope. Model 1 predicts an approximate total displacement of 5334μm, which is roughly 28% larger than the measured displacement.

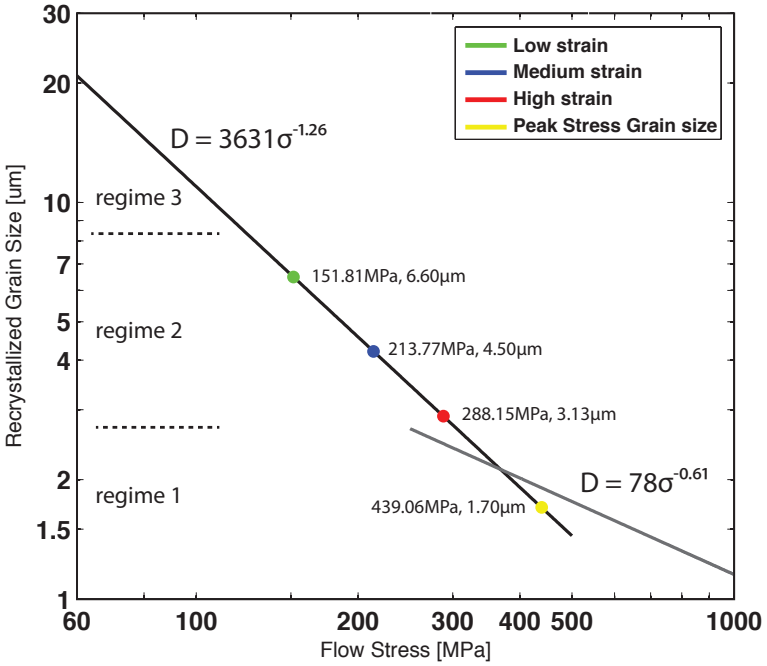

Figure 3.5 Recrystallized grain size piezometer for dislocation creep in quartz by Stipp and Tullis (2003). The steep dark grey curve is defined for relating stress and grain size for recrystallization mechanisms in regime 2/3 defined by Hirth and Tullis (1992), while the light grey gentle slope is used when regime 1 recrystallization is active. The steep grey line is only used in this study because SGR (regime 2) is the dominant recrystallization mechanism observed.

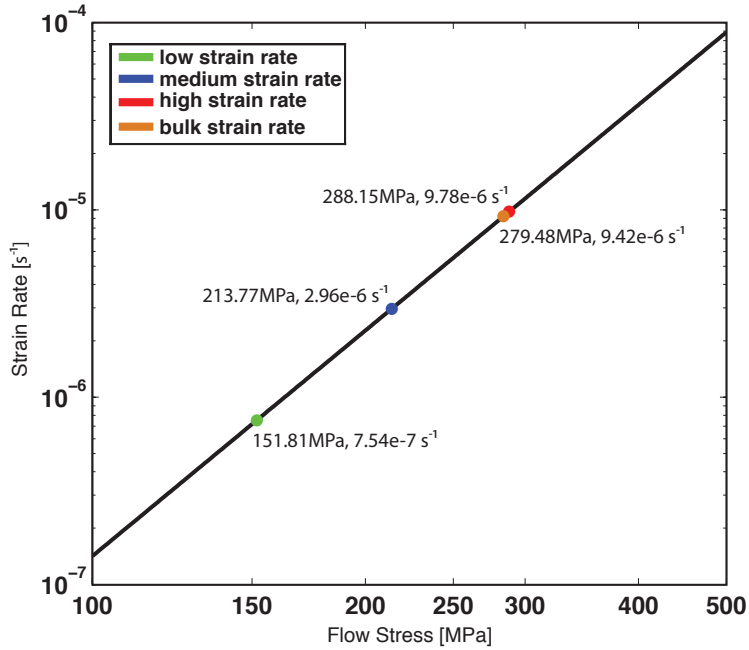

Figure 3.6 Flow stress measurements plotted on the Hirth et al. (2001) flow law for quartz.

Table 3.2 *Model 1 data for the different regions of strain*

	Grain Size(μm)	Flow Stress (MPa)	$\gamma(s^{-1})$	γ	Displacement (μm)
Low strain	6.48	151.81	7.54e-7	0.32	304
Med. strain	4.21	213.77	2.96e-6	1.25	1190
High strain	2.89	288.15	9.78e-6	4.11	3840

3.5.2. Model 2:

Model 2 represents a shear zone that progressively localizes over time. At various time periods, related to mechanical transitions, localization of the deforming zone occurs where a thinner localized zone will continue to deform, while the outer regions will continue to deform as well but at slower strain rates. The time periods for the different localized zones are illustrated in figure 3.7, and the thickness of each zone in figure 3.8. The localized zone that continues to deform, will deform at faster strain rates than at the previously thicker localized zone. This type of shear zone is similar to the type 2 shear zone described by Hull (1988) and Means (1995). The increase in strain rate with a thinner localized zone can be assumed because it is known that the experiment is preformed at a constant displacement rate, so if the localized zone thins, the strain rate must increase to compensate for the bulk displacement rate of the whole sample. It is assumed that the slower strain rate regions will be deforming at a slow enough rate where grain growth processes become active in these regions.

For model 2, four different zones were created: zone 1, zone 2, zone 3, and zone 4, which contain four different localization time-periods. Each zone represents a thinner localized zone, where zone 1 represents the entire sample cross-section and zone 4 is an ~200μm thick zone illustrated in a modified version of the strain profile (figure 3.8).

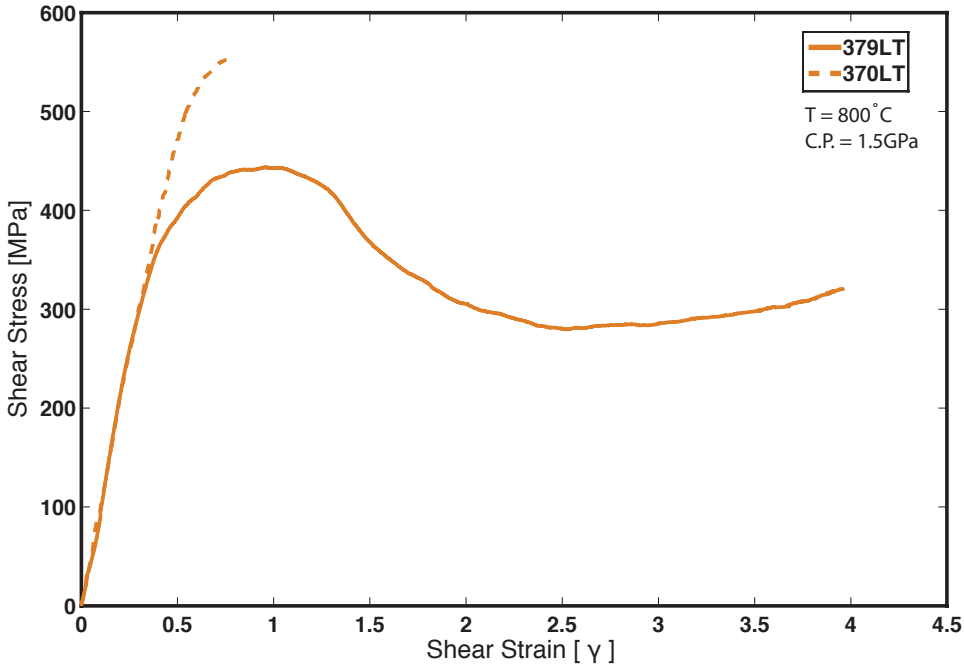

Figure 3.7 Shear stress – Time plot for 100% quartz experiment (379LT) deformed to steady state conditions. The different zones represent the time at which localization occurred. These zones have been chosen based on both microstructural observations and mechanical transitions in the mechanical data.

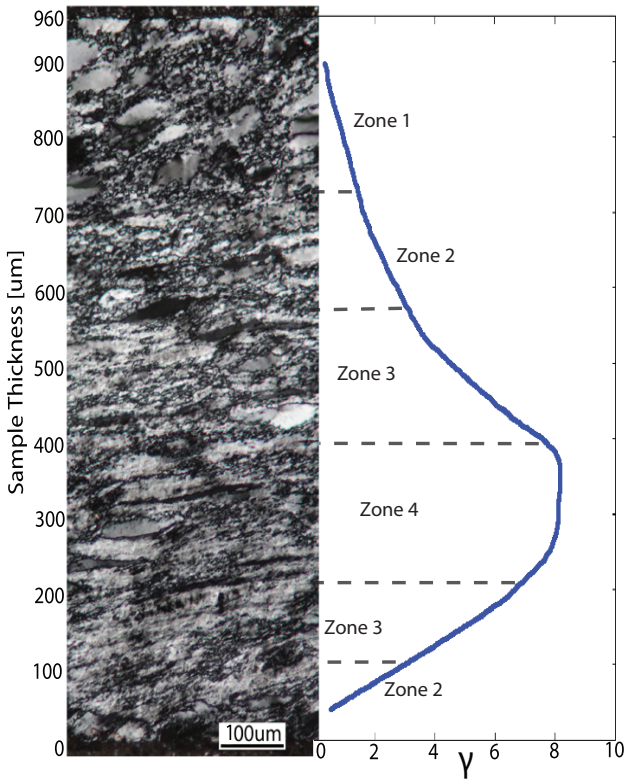

Figure 3.8 A modified version of figure 3.4 for Model 2 where the thickness of the different localized zones are annotated on the strain profile. Zone 1 represents the entire sample thickness while zone 4 represents a zone approximately 200μm thick.

Based on the microstructures in the peak stress experiment, (figure 3.2b), no strain localization has occurred and deformation is homogeneous throughout the sample. From this point, the model assumes that the first localization zone to occur, zone 1 to zone 2, develops at the onset of weakening from the point of peak stress. It is also assumed that zone 4 does not initiate localization until steady state flow is achieved, and zone 3 is assumed to initiate half way between the peak stress and the initiation of steady state flow (figure 3.7). Following these assumptions, the time intervals for each period of localization can be obtained from the mechanical data. If grain growth is assumed to become active at the onset of localization, then the time period for grain growth in each zone can be determined from the mechanical data. Applying the value of the shear stress from the point of peak stress recorded from the mechanical data of the steady state experiment (379LT) and applying it to the recrystallized grain-size piezometer for quartz, a grain size of 1.68μm is calculated; yellow point in figure 3.5. An estimate for the approximate grain growth can be calculated by using the novaculite grain growth data presented by Tullis and Yund (1982). The grain growth rate for novaculite at 1.5GPa confining pressure and 800°C is extrapolated to be approximately 0.09μm/hr. The calculated grain growth experienced from the region that does not localize from zone 1 to zone 2 is 72.10 hours, which correlates to 6.40μm in grain growth (figure 3.9). If the average recrystallized grain size is approximately 1.68μm at peak stress, then the final grain size, when the experiment is quenched, would yield 8.08μm for the zone 1 region. The average measured grain size of this zone from the microstructures is 8.30μm, which is in strong agreement with the calculated grain size. The same procedure can be calculated for zones 2 and 3. Zone 2 experiences 50.66 hrs of grain growth, where the predicted recrystallized grain size is 2.35μm with 4.56μm of grain growth yielding an average grain size of 6.91μm. The average measured grain size is 7.10μm. Zone 3 experiences 29.22 hrs of grain growth, where the predicted recrystallized grain size is 3.00μm with 2.63μm of grain growth, yielding an average grain size of 5.63μm. The average measured grain size is 6.05μm. Figure 3.9 displays the grain growth rate for each zone; zone 4 is assumed to be actively deforming when the experiment is quenched and no grain growth occurs in this zone.

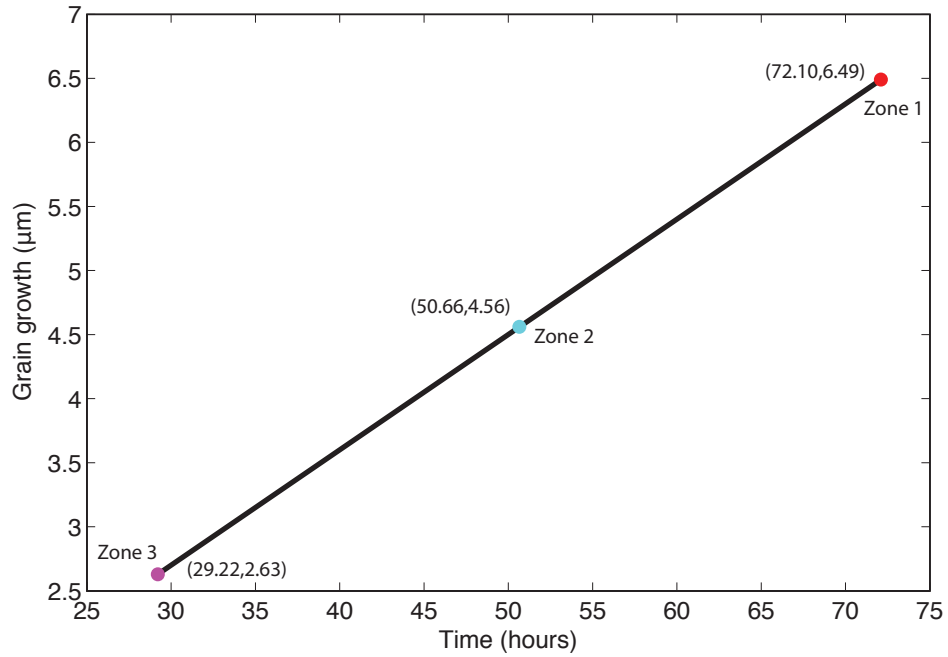

Figure 3.9 Plot representing the approximate grain growth for recrystallized grains based on the growth rate for novaculite determined by Tullis and Yund (1982). The slope of the line is 0.09μm/hr and based on the time of grain growth for each zone an approximate change in grain size can be achieved for each zone. Though Tullis and Yund (1982) state that grain growth is not linear over time, it is assumed that a linear fit is appropriate for the time scale of this experiment.

Table 3.3 *Data on the four different periods of strain localization*

	Thickness (μm)	Time of localization (sec)	Time of grain growth (sec)	Calculated Recrystallized grain size (μm)	Grain growth (μm)	Calculated Grain size (μm)	Measured Grain size (μm)
Zone 1	960	160828	259565	1.70	6.49	8.19	8.35
Zone 2	750	77192	182373	2.36	4.56	6.91	7.10
Zone 3	450	77193	105180	3.00	2.63	5.63	6.00
Zone 4	200	105180	0	2.53	0	0	3.45

To determine the specific strain rate for each zone during its period of localization, boundary conditions were constructed to approximate these values. Boundary conditions were required because there is no clear-cut method for determining the specific strain rates for each zone during its period of localization. A possible solution is to take the total amount of accumulated strain for each zone during period of localization based on the strain profile and divide by the time of localization for each zone, but this method does not agree with the assumptions for the model since zone 4 produces a strain rate lower than zone 3; this method is completely dependent

on where the boundaries between the different zone are placed. To avoid this problem upper and lower bounds were calculated to estimate the strain rate for each zone during its time of localization.

Zone 1 is the only zone where an exact strain rate can be calculated because the zone consists of the entire sample thickness and can be calculated from the mechanical data directly. For zones 2, 3, and 4 a lower bound can be constructed by calculating the average strain rate for each zone based on the maximum finite strain accumulated for each zone and the total time from the beginning of deformation to the point when the zone localizes to a new zone. For example, zone 4 accumulates $\gamma \sim 8$ in 4,200,393 sec, but this calculation includes the strain that was previously accumulated when zones 1, 2, and 3 were actively deforming, so the 'true' strain rate for just the localization period of zone 4 must be higher than this value because it is assumed that for each localization period the strain rate increases. This procedure is repeated for zones 2 and 3, and the lower bound strain rate values are plotted as the small diamonds in figure 3.10. An upper bound for the strain rates can be constructed if the non-localized regions are assumed to not deform at all, and the strain energy is localized only within the actively deforming zone. This can be accomplished because it is known that zone 1 represents the entire sample thickness and then based on the amount of thinning of each zone during each localization period, the strain rate must increase by the percent each zone thins in comparison to the previous localized zone because the experiment is performed at a constant displacement rate and this rate must be conserved within the deforming zone. This strain rate value must be higher than the 'true' strain rate value for each zone because it is assumed in the model that the non-localized zones continue to deform, but at much slower strain rates. Table 3.4 includes the data for the construction of both the upper and lower bounds.

Table 3.4 *Upper and Lower bound data for strain rate determination in Model 2*

	Lower Bound			*Upper Bound*	
	Time (sec)	**γ**	**LBγ (s^{-1})**	**Thinning (%)**	**UBγ (s^{-1})**
Zone 1	160828	1.5	9.33e-6	0	9.33e-6
Zone 2	238020	2.5	1.05e-5	21.8	1.14e-5
Zone 3	315213	4.5	1.43e-5	40.0	1.59e-5
Zone 4	420393	8	1.90e-5	56.0	2.48e-5

The upper and lower bounds were plotted for each zone of localization in figure 3.10. The results of the upper and lower bounds are in accordance with the assumptions of the model and there is no overlap between an upper or lower bound calculation for different zones.

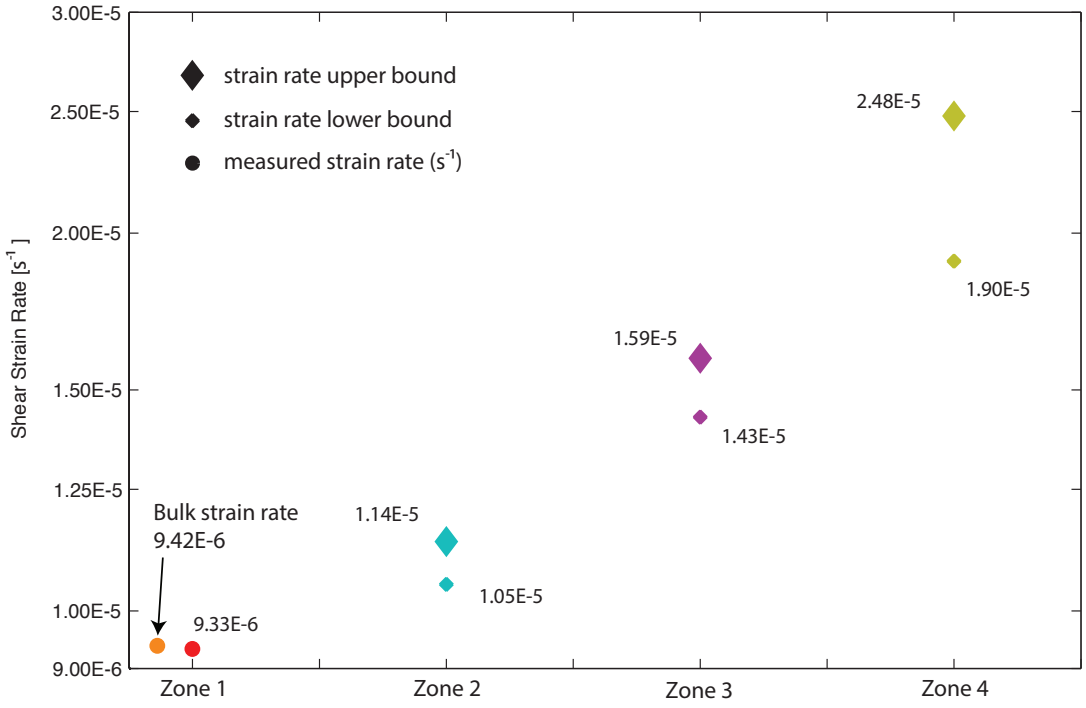

Figure 3.10 Plot represents the predicted range of possible strain rates for each zone during localization. Lower and upper bounds were calculated and discussed in the text. These bounds agree with the assumptions of the model because there is no overlap between upper or lower bounds between zones and that the strain rate must increase during localization.

3.6. Discussion

3.6.1. Measurements and strain gradient

All of the microstructural measurements were taken from a 400μm by 960μm cross-sectional area where there is a visible strain gradient in the steady state experiment run to a bulk shear strain of $\gamma \sim 4$. Previous studies often cite this strain gradient, or variation of high and low strain regions, if it is observed within the sample, but no previous study has used this gradient as a measurement for strain localization (Dell'Angelo and Tullis 1996; Heilbronner and Tullis 2006; Pec et al. 2012). Heilbronner and Tullis (2006) however, have used various regions within a single experimental sample that possess different finite strains to investigate CPO orientations at regions of various accumulated strains and percent recrystallization. We feel that analyzing this

strain gradient would allow us to investigate the process of strain localization within a typical monomineralic general shear experiment preformed in a modified-Griggs apparatus and apply it to localizing deformation structures. A first-order approach is taken to develop these two end-member models in an attempt to establish relationships between various physical parameters observed within the experimentally produced shear zone. For these two different models, regions or zones were developed to allow for quantitative relationships to be established between finite strain, recrystallized grain size, and shear strain, which would allow various assumptions to be proposed and tested for each model.

The recrystallized grain size piezometer by Stipp and Tullis (2003) is used to calculate the different flow stresses based on the recrystallized grains in Model 1, while the piezometer is also used to calculate the grain size based on the flow stress from the mechanical data in Model 2. Although Stipp and Tullis (2003) present two different slopes in their piezometer, these two different slopes are based on the recrystallization mechanism observed in their study. All of the experiments in this study were performed where the dominant recrystallization mechanism is subgrain rotation recrystallization. This mechanism is defined by the slope $D=3631\sigma^{-1.26}$ and though the flow stress recorded at peak stress conditions clearly falls into the regime 1 region of their plot defined by the slope $D=78\sigma^{-0.61}$, (figure 3.5), we feel justified in using just the one slope for our calculations. If the slope $D=78\sigma^{-0.61}$ was used for the recrystallized grain size calculation in model 2, the recrystallized grain size would change from 1.70μm to 1.91μm, which would result in a calculated observed grain size of 8.37μm, which would match our measured result even better. Although this result better represents our measured grain size, it is difficult to assess which slope to choose because the most accurate grain size measurement that were recorded are ±0.5μm, which is not specific enough to distinguish between the two results and because the experiments were performed at conditions for subgrain rotation recrystallization and these are the microstructures observed in our experiments, we feel justified in using the slope $D=3631\sigma^{-1.26}$ for all of our measurements.

The bulk strain rate for the steady state experiment is plotted against the different regions or zone calculated for both models (figures 3.6 and 3.10). In Model 1, (figure 3.6) demonstrates that the bulk strain rate best represents the fastest strain rate region of the sample. In Model 2, the bulk strain rate is best represented by the

deformation of zone 1 when the entire sample was deforming. This result presents a disagreement between Model 1 and Model 2. For model 1, this demonstrates that both the medium and low strain regions within the strain gradient are deforming at a slower strain rate than the bulk strain rate, which requires the fastest strain rate region to deform at a faster rate than the bulk strain rate to conserve the bulk displacement rate of the experiment. Model 2 however, is in agreement with the mechanical data where zone 1 is approximately deforming at the same strain rate as the bulk strain rate and zones 2, 3, and 4 are deforming at faster strain rates than the bulk strain rate, (figure 3.10), conserving the displacement rate of the experiment. Model 2 is also consistent with microstructures observed in the peak stress experiment where deformation is homogeneous throughout the sample. Model 1 is inconsistent with these microstructural observations and would assume a strain gradient across the sample. This result does not disprove Model 1 as a valid model for strain localization in nature but based on these results, Model 2 better represents strain localization at high shear strains in the Griggs apparatus.

3.6.2. Localization – geometrical softening

Geometrical softening is a mechanism proposed by Poirier (1980) and White et al. (1980) where strain localizes in regions where intracrystalline slip is most favorable in a material. Muto et al. (2011) conducted quartz single crystal experiments in shear to investigate the role of different quartz slip systems and the evolution of active slip systems with increasing shear strains to determine the most favorable slip systems for geometrical softening. The single crystal results from Muto et al. (2011) and the polycrystalline quartz results from Heilbronner and Tullis (2006) demonstrate that at high shear strain intracrystalline slip is most favorable in the prism <a> orientation, which produces a Ymax orientation in quartz c-axis pole figures. Muto et al. (2011) postulate that recrystallization was initiated during a change in slip system, from prism [c] to rhomb <a> and then a further change in slip system occurred due to grain boundary migration (GBM) recrystallization, which activated the prism <a> slip system producing Ymax orientations. The experiments performed by Muto et al. (2011) and Heilbronner and Tullis (2006) were conducted at 900°C where GBM recrystallization is clearly active, based on their results. The results from this study, conducted at 800°C, demonstrate that GBM recrystallization is not active and that SGR recrystallization is the

dominant recrystallization mechanism, which agrees with results by Muto et al. (2011), who state that grain boundary migration (GBM) recrystallization must be active to achieve the Ymax orientation. Regardless of the lack of Ymax orientations, the process of recrystallization is still important to geometrical softening at the conditions conducted in this study. Pole figures for the three different experiments conducted in this study show distinct CPO transitions and the development of a strong CPO fabric once steady state conditions are achieved. The CPO develops from a random texture to a prism [c] single girdle orientation with a single maximum to a rhomb <a> CPO fabric at steady state conditions (figure 3.11a). These results agree with CPO results presented by Heilbronner and Tullis (2006).

Separating the CPO of the recrystallized grains and the original grains for the steady state experiment demonstrates that there is likely a change in the dominant slip system from prism [c] to rhomb <a> at the onset of recrystallization, (figure 3.11b), which is assumed to be the point where localization is initiated, based on Model 2 from this study. The peak stress experiment displays ~10% recrystallization, though some of these recrystallized grains are likely the product of neorecrystallization due to grain crushing and nucleation during the pressurization, which makes it difficult for direct grain size measurements but it is clear that dislocation processes are active at these conditions. The CPO of the peak stress experiment and the CPO of the original grains from the steady state experiment provide strong evidence that the process of recrystallization is coupled with strain localization. This result is also observed in the experiments conducted by Heilbronner and Tullis (2006) where strain localization is only observed when recrystallization processes are active.

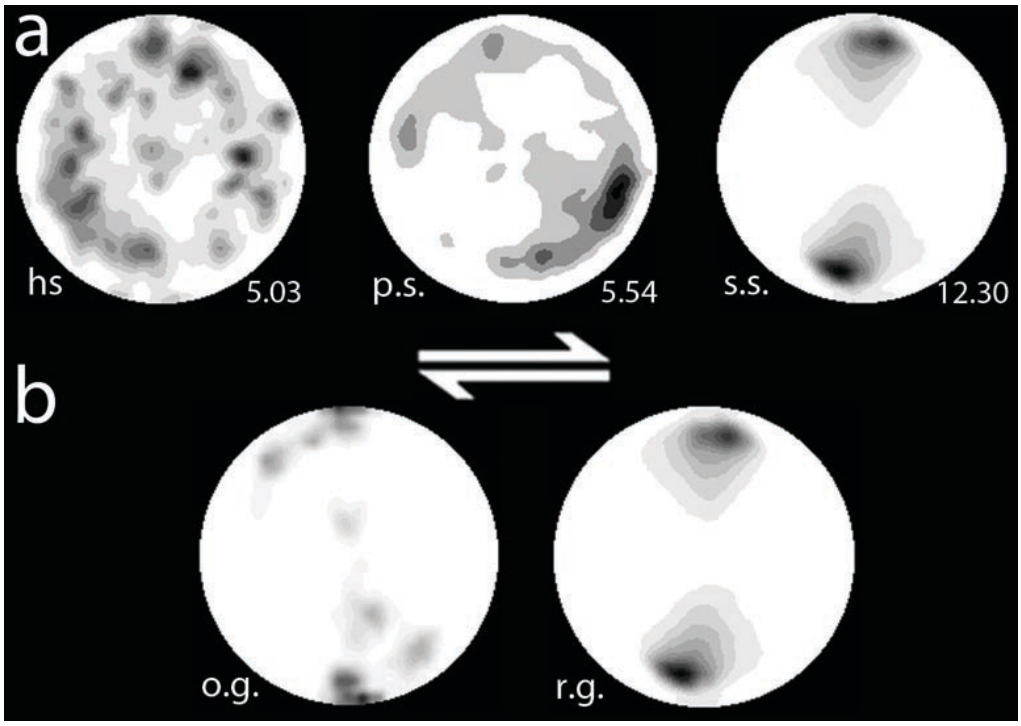

Figure 3.11 Quartz CPO pole figures a) hs =hydrostatic, p.s.= peak stress, and s.s.= steady state., with the pole figure maximum placed next to each pole figure, b) quartz CPO for just the o.g. =original grains and the r.g. = recrystallized grains where

An interesting question to pose is, once the aggregate has completely recrystallized and the aggregate is deforming at steady state conditions, is there a point when strain no longer localizes? Hull (1988) describes a Type 3 shear zone where the thickness of the shear zone does not change with time, which (Hull 1988) predicts could be the result of achieving a constant strain rate across the shear zone or true steady state conditions, typically not reached in experiments. Based on the strain profile constructed for the strain gradient in this study there is a flat plateau of the finite strain. This region, zone 4, in Model 2 is assumed to initiate at the onset of reaching steady state conditions. If zone 4 is truly at steady state conditions, where the strain profile displays relatively homogeneous strain across this zone, then this zone alone could be considered a Type 3 shear zone by Hull (1988) and no further localization would occur until a change in the system. s

3.6.3. Grain size – Piezometer vs. Paleowattmeter

Strain localization in the steady state experiment conducted in this study is observed and the recrystallized grain size throughout this sample changes based on the amount of accumulated strain. Heilbronner and Tullis (2006) and Muto et al. (2011) indicate a similar result, where smaller recrystallized grain sizes are observed in regions

where high strain has been accumulated. This result is provides evidence that an increase in strain rate due to strain localization can affect the size of recrystallizing grains during dislocation creep deformation. In the context of the paleowattmeter where stress is assumed to be uniform across the sample, Model 2 is consistent with the trend that recrystallized grain sizes will be larger in regions of slower strain rates while zones with faster strain rates will produce smaller grains. This study as well as Muto et al. (2011) assumes that the stress gradient across the sample is homogeneous. This result is inconsistent with the theory of the recrystallized grain size piezometer, where the recrystallized grain size is based solely on the stress of the system. Through personal communication with Prof. Greg Hirth, sets of coaxial experiments were conducted on polycrystalline quartz aggregates where decreasing strain rate steps were performed during the experiments. As the strain rate decreased, the microstructures show an increase in the recrystallized grain size, which agrees with the results of this experiment and Muto et al. (2011) where the recrystallized grain size is dependent on both the stress and strain rate of the system. Based on the results of this study as well as the strong agreement from other experimental based studies on localization of shear zone it is important in understanding the consequences of using a grain size piezometer in natural studies when investigating monomineralic shear zones where geometrical softening is likely a dominate localization mechanism.

3.7. Conclusion

To conclude, this work presents two end-member models that describe the development of localization in a shear zone where the paleowattmeter is used as a reference frame. Model 1, where deformation is active throughout the entire sample and a strain rate gradient is assumed with the fastest strain rates localized at the core of the shear zone, decreasing to slower strain rates at the termination of the shear zone. Based on the calculated finite strain for the cross sectional area, Model 1 overcompensates the shear displacement that is measured from the experiment, in relation to the finite strain measurements.

Model 2, where deformation is localized over time based on various mechanical transitions, shows consistency with theoretical calculations of stress, strain rate, and grain growth data that is consistent with measured data within the cross sectional area of the sample. Model 2 shows agreement with the assumption that localization does not

initiate until peak stress conditions where recrystallization is coupled with the development of strain localization.

Model 2 is consistent with the assumption that grain growth is active once localization has occurred and agrees with other experimental work where grain growth processes can dominant when there is a decrease in strain rate. The implications for applying this type of model to natural shear zones would require an understanding of stress as well as the strain, and strain rate of the deformation structure within the outcrop.

Reference

1. Austin, N., and B. Evans (2007), Paleowattmeters: A scaling relation for dynamically recrystallized grain size, *Geology*, *35*(4), 343–346, di:10.1130/G23244A.1.

2. Austin, N., and B. Evans (2009), The kinetics of microstructural evolution during deformation of calcite, *J. Geophys. Res.*, *114*, B09402, doi:10.1029/2008JB006138.

3. Barnhoorn, A., M. Bystricky, L. Burlini, and K. Kunze (2004), The role of recrystallisation on the deformation behavior of calcite rocks: large strain torsion experiments on Carrara marble, *J. Struct. Geo.*, *26*, 885–903.

4. Berthé, D., P. Choukroune, and P. Jegouzo (1979), Orthogneiss, mylonite and non coaxial deformation of granites: the example of the South Armorican Shear Zone, *J. Struct. Geo.*, *1*, 31–42.

5. Bouchez, J.-L. (1977), Plastic deformation of quartzite's at low temperature in an area of natural strain gradient (Angers, France), *Tectonophysics*, *39*, 25–50.

6. Bouchez, J.-L. (1978), Preferred orientations of quartz a-axes in some tectonites; kinematic inferences, *Tectonophysics*, *49*, T25–T30.

7. Bouchez, J.-L. (1983), Fabric asymmetry and shear sense in movement zones, *Geologische Rundschau*, *72*, 401–419.

8. Braun, J., J. Chéry, A. Poliakov, D. Mainprice, A. Vauchez, A. Tomassi, and M. Daignières (1999), A simple parameterization of strain localization in the ductile regime due to grain size reduction: A case study for olivine, *J. Geophys. Res.*, *104*, 25,167–25,181.

9. Burg, J. P., and P. Laurent (1978), Strain analysis of a shear zone in a granodiorite, *Tectonophysics*, *47*, 15–42.

10. Bürgmann, R., and G. Dresen (2008), Rheology of the Lower Crust and Upper Mantle: Evidence from Rock Mechanics, Geodesy, and Field Observations, *Annu. Rev. Earth Planet. Sci.*, *36*, 531–567, doi:10.1146/annurev.earth.36.031207.124326.

11. Canova, G.R., H.R. Wenk, and A. Molinari (1992), Deformation modeling of multi-phase polycrystals: case of a quartz-mica aggregate, *Acta. metall. mater.*, *40*, 7 1519–1530.

12. Carreras, J., A. Estrada, and S. White (1977), The effects of folding on the c-axis fabrics of a quartz mylonite, *Tectonophysics*, *39*, 3–24.

13. Dell'Angelo, L.N., and J. Tullis (1996), Textural and mechanical evolution with progressive strain in experimentally deformed aplite, *Tectonophysics*, *256*, 57–82.

14. De Ronde, A.A., H. Stünitz, J. Tullis, and R. Heilbronner (2005), Reaction-induced weakening of plagioclase–olivine composites, *Tectonophysics*, *409*, 85–106.

15. Eisbacher, G.H. (1970), Deformation mechanics of mylonite rocks and fractured granites in Colequid mountains, Nova Scotia, Canada, *Bull. Geol. Soc. Am.*, *81*, 2009–2020.

16. Etchecopar, A. (1977), A plane kinematic model of progressive deformation in a polycrystalline aggregate, *Tectonophysics*, *39*, 121–139.

17. Etchecopar, A., and G. Vasseur (1987), A 3-D kinematic model of fabric development in polycrystalline aggregates: comparisons with experimental and natural examples, *J. Struct. Geo.*, *9*(5-6), 705–717.

18. Evans, B.W., J. Renner, and G. Hirth (2001), A few remarks on the kinetics of static grain growth in rocks, *International Journal of Earth Science*, *90*, 88–103.

19. Garcia Celma, A. (1982), Domainal and fabric heterogeneities in the Cap de Creus quartz mylonites, *J. Struct. Geo.*, *4*, 443–455.

20. Gerbi, C., N. Culshaw, and J. Marsh (2010), Magnitude of weakening during crustal-scale shear zone development, *J. Struct. Geo.*, *32*, 107–117.

21. Harren, S. V., H. E. Déve, and R. J. Astro (1988), Shear band formation in plane strain compression, *Acta Metall.*, *36*, 2455–2480.

22. Handy, M.R. (1990), The solid-state flow of polymineralic rocks, *J. Geophys. Res.*, *95*(B6), 8647–8661.

23. Handy, M.R. (1994), Flow laws for rocks containing two non-linear viscous phases: a phenomenological approach, *J. Struct. Geo.*, *16*(3), 287–301.

24. Heilbronner, R., and J. Tullis (2006), Evolution of c axis pole figures and grain size during dynamic recrystallization: Results from experimentally sheared quartzite, *J. Geophys. Res.*, *111*, B10202, doi:10.1029/2005JB004194.

25. Hermann, J., and D. H. Green (2001), Experimental constraints on high pressure melting in subducted crust, *Earth and Planetary Science Letters*, *188*, 149–168.

26. Herwegh, M., and M. R. Handy (1996), The evolution of high-temperature mylonitic microfabrics: evidence from simple shearing of a quartz analogue (norcampfor), *J. Struct. Geo.*, *18*, 689–710.

27. Herwegh, M., J. Linckens, A. Ebert, A. Berger, and S.H. Brodhag (2011), The role of second phases for controlling microstructural evolution in polymineralic rocks: A review, *J. Struct. Geo.*, *33*, 1728–1750.

28. Hippertt, J.F.M. (1994), Grain boundary microstructures in micaceous quartzite: Significance for fluid movement and deformation processes in low metamorphic grade shear zones, *The Journal of Geology*, *102*(3), 331–348.

29. Hirth, G., and J. Tullis (1992), Dislocation creep regimes in quartz aggregates, *J. Struct. Geo.*, *14*(2), 145–159.

30. Hirth, G., Teyssier, C., and Dunlap, W.J. (2001), An evaluation of quartzite flow laws based on comparisons between experimentally and naturally deformed rocks, *International Journal of Earth Sciences*, *90*, 77–87, doi: 10.1007/s005310000152.

31. Holyoke, C.W., and A.K. Kronenberg (2010), Accurate differential stress measurement using the molten salt cell and solid salt assembles in the Griggs apparatus with applications to strengh, piezometers and rheology, *Tectonophysics*, *494*, 17–31.

32. Holyoke, C.W., and J. Tullis (2006), The interaction between reaction and deformation: an experimental study using a biotite + plagioclase + quartz gneiss, *J. metamorphic Geol.*, *24*, 743 – 762.

33. Hull, J. (1988), Thickness–displacement relationships for deformation zones, *J. Struct. Geo.*, *10*, 431–435.

34. Ingles, J. (1983), Theoretical strain patterns in ductile zones simultaneously undergoing heterogeneous simple shear and bulk shortening, *J. Struct. Geo.*, *5*, 369–381.

35. Ingles, J. (1985), Theoretical and natural strain patterns in ductile simple shear zones, *J. Struct. Geo.*, *115*, 315–334.

36. Ingles, J. (1986), Terminations of ductile shear zones, *Tectonophysics*, *127*, 87–95.

37. Jessell, M. (1988), Simulation of fabric development in recrystallizing aggregates–I. Description of the model, *J. Struct. Geo.*, *10*(8), 771–778.

38. Johnson, S.E., R.H. Vernon, and P. Upton (2004), Foliation development and progressive strain-rate partitioning in the crystallizing carapace of a tonalite pluton: microstructural evidence and numerical modeling, *J. Struct. Geo.*, *26*, 1845–1865.

39. Jordan, P.G. (1987), The deformational behavior of bimineralic limestone–halite aggregates, *Tectonophysics*, *135*, 185–197.

40. Jordan, P. (1988), The rheology of polymineralic rocks – an approach, *Geologische Rundschau*, *77*(1), 285–294.

41. Kameyama, M., D.A. Yuen, and S.-I. Karato (1999), Thermal-mechanical effects of low-temperature plasticity (the Peierls mechansm) on the deformation of a viscoelastic shear zone, *Earth and Planetary Science Letters*, *168*, 159–172.

42. Kelemen, P.B., and G. Hirth (2007), A periodic shear-heating mechanism for intermediate-depth earthquakes in the mantle, *Nature*, *446*, doi: 10.1038/nature05717.

43. Law, R.D. (1990), Crystallographic fabrics: a selective review of their applications to research in structural geology, *Geological Society, London, Special Publications*, *54*, 335–352, doi: 10.1144/GSL.SP.1990.054.01.30.

44. Linckens, J., R.H.C. Bruijn, and P. Skemer (2014), Dynamic recrystallization and phase mixing in experimentally deformed peridotite, *Earth and Planetary Science Letters*, *388*, 134–142.

45. Lisle, R.J. (1985), The effect of composition and strain on quartz-fabric intensity in pebbles from a deformed conglomerate, *Geologosche Rundschau*, *74*(3), 657–663.

46. Lister, G.S., and B.E. Hobbs (1980), The simulation of fabric development during plastic deformation and its application to quartzite: the influence of deformation history, *J. Struct. Geo.*, *2*(3), 355–370.

47. Lister, G.S., and M.S. Paterson (1979), The simulation of fabric development during plastic deformation and its application to quartzite: fabric transitions, *J. Struct. Geo.*, *1*, 99–115.

48. Lister, G.S., and G.P. Price (1978), Fabric development in a quartz feldspar mylonite, *Tectonophysics*, *49*, 37–78.

49. Means, W.D. (1995), Shear zones and rock history, *Tectonophysics*, *247*, 157–160.

50. Molinari, A., G.R. Canova, and S. Ahzi (1987), A self consistent approach of the large deformation polycrystal viscoplasticity, *Acta. Metallurgica*, *35*(12), 2983–2994.

51. Montési, L.G.J. (2013), Fabric development as the key for forming ductile shear zones and enabling plate tectonics, *J. Struct. Geo.*, *50*, 254–266.

52. Montési, L.G.J., and G. Hirth (2003), Grain size evolution and the rheology of ductile shear zones: from laboratory experiments to postseismic creep, *Earth and Planetary Science Letters*, *211*, 97–110.

53. Muto, J., G. Hirth, R. Heilbronner, and J. Tullis (2011), Plastic anisotropy and fabric evolution in sheared and recrystallized quartz single crystals, *J. Geophys. Res.*, *116*, B02206, doi:10.1029/2010JB007891.

54. Niemeijer, A.R. and C.J. Spiers (2005), Influence of phyllosilicates on fault strength in the brittle–ductile transition: insights from rock analogue experiments, *From: Bruhn, D. & Burlini, L. (eds) High Strain Zones: Structure and Physical Properties. 245*, 303–327.

55. Ogawa, M. (1987), Shear instability in a viscoelastic material as the cause of deep focus earthquakes, *J. Geophys. Res.*, *92*, 13,801–13,810.

56. Olgaard, D.L., and B. Evans (1986a), Effect of second-phase particles on grain growth in calcite, *Journal of the American Ceramic Society*, *69*, C-272–C277.

57. Olgaard, D.L., and B.W. Evans (1986b), Effect of second-phase particles on grain growth in calcite, *Journal of American Ceramic Society*, *69*, C-272–C277, doi: 10.1111/j.1151-2916.1986.tb07374.x.

58. Olgaard, D.L., and B. Evans (1988), Grain growth in synthetic marbles with added mica and water, *Contributions to Mineralogy and Petrology*, *100*, 246–260.

59. Panozzo, R. H. (1983), Tow-dimensional analysis of shape-fabric using projections of digitized lines in a plane, *Tectonophysics*, *95*, 279–294.

60. Panozzo, R. (1984), Two-dimensional strain from the orientation of lines in a plane, *J. Struct. Geo.*, *6*, 215–221.

61. Panozzo Heilbronner, R., and C. Pauli (1993), Integrated spatial and orientation analysis of quartz c-axes by computer-aided microscopy, *J. Struct. Geo.*, *15*, 369–382.

62. Pec, M., H. Stünitz, and R. Heilbronner (2012), Semi-brittle deformation of granitoid gouges in shear experiments at elevated pressures and temperatures, *J. Struct. Geo.*, *38*, 200–221.

63. Pieri, M., L. Burlini, K. Kunze, D.L. Olgaard, and I.C. Stretton (2001a), Rheological and microstructural evolution of Carrara marble with high shear strain: results from high temperature torsion experiments, *J. Struct. Geo.*, *23*, 1393–1413.

64. Pieri, M. K. Kunze, L. Burlini, I.C. Stretton, D.L. Olgaard, J.-P. Burg, and H.R. Wenk (2001b), Texture development of calcite by deformation and dynamic recrystallisation at 1000K during torsion experiments of marble to large strains, *Tectonophysics*, *330*, 119–140.

65. Pitzer, K.S., and S.M. Sterner (1994), Equations of state valid continuously from zero to extreme pressures for H20 and CO2, *Journal of Chemical Physics*, *101*, 3111–3116.

66. Poirier, J.P. (1980), Shear localization and shear instability in materials in the ductile field, *J. Struct. Geo.*, *2*, 135–142.

67. Précigout, J., and F. Gueydan (2009), Mantle weakening and strain localization: Implications for the long-term strength of the continental lithosphere, *Geology*, *37*, doi:10.1130/G25239A.1.

68. Ramsey, J.G. (1980), Shear zone geometry: a review, *J. Struct. Geo.*, *2*, 83–99.

69. Ramsey, J.G., and R.H. Graham (1970), Strain variations in shear belts, *Can. J. Earth Sci.*, *7*, 786–813.

70. Regenauer-Lieb, K. and D.A. Yuen (2003), Modeling shear zones in geological and planetary sciences: solid- and fluid-thermal-mechanical approaches, *Earth-Science Reviews*, *63*, 295–349.

71. Ross, J.V., S.J. Bauer, and F.D. Hansen (1987), Textural evolution of synthetic anhydrite–halite mylonites, *Tectonophysics*, *140*, 307–326.

72. Rutter, E.H., and K.H. Brodie (2004), Experimental grain size-sensitive flow of hot-pressed Brazilian quartz aggregates, *J. Struct. Geo.*, *26*, 2011–2023.

73. Rutter, E.H., and K.H. Brodie (2004), Experimental intracrystalline plastic flow in hot-pressed synthetic quartzite prepared from Brazilian quartz crystals, *J. Struct. Geo.*, *26*, 259–270.

74. Schmid, S.M., and M. Casey (1986), Complete fabric analysis of some commonly observed quartz c-axis patterns, *Geophysical Monograph Series*, *36*, 263–286.

75. Schmid, S.M., and M.R. Handy (1991), Towards a genetic classification of fault rocks: geological usage and tectonophysical implications. In: Müller, D.W., McKenzie, J.A., Weissert, H. (Eds.), *Controversies in Modern Geology*, Academic Press London, pp. 95–110.

76. Schmid, S.M., R. Panozzo, and S. Bauer (1987), Simple shear experiments on calcite rocks: rheology and microfabric, *J. Struct. Geol.*, *9*, 747–778.

77. Shea, W.T., and A.K. Kronenberg (1992), Rheology and deformation mechanisms of an isotropic mica schist, *J. Geophys. Res.*, *97*, 15,201–15,237.

78. Shea, W.T., and A.K. Kronenberg (1993), Strength and anisotropy of foliated rocks with varied mica contents, *J. Struct. Geo.*, *15*, 1097–1121.

79. Simpson, C. (1983), Displacement and strain patterns from naturally occurring shear zone terminations, *J. Struct. Geo., 5*, 497–506.

80. Skemer, P., J.M. Warren, P.B. Kelemen, and G. Hirth (2010), Microstructural and rheological evolution of a mantle shear zone, *Journal of Petrology*, *51*, 43–53.

81. Song, W. J., and J.-H. Ree (2007), Effect of mica on the grain size of dynamically recrystallized quartz in a quartz–muscovite mylonite, *J. Struct. Geo.*, *29*, 1872–1881.

82. Starkey, J., and C. Cutforth (1978), A demonstration of the independence of the degree of quartz preferred orientation and the quartz content of deformed rocks, *Canadian Journal of Earth Sciences*, *15*, 841–847.

83. Sterner, S.M., and K.S. Pitzer (1994), An equation of state for carbon dioxide valid from zero to extreme pressures, *Contributions to Mineralogy and Petrology*, *117*, 362–374.

84. Stipp, M., and J. Tullis (2003), The recrystallized grain size piezometer for quartz, *Geophys. Res. Lett.*, *30*(21), 2088, doi:10.1029/2003GL018444.

85. Takeshita, T., H.-R. Wenk, A. Molinari, and G. Canova (1990), Simulations of dislocation assisted plastic deformation in olivine polycrystals, in *Deformation Processes in Minerals, Ceramics and Rocks*, edited by D. J. Barber and P. G. Meredith, pp. 365–377, Unwin Hyman Ltd., London, 1990.

86. Tarantola, A., L. Diamond and, H. Stünitz (2010), Modification of fluid inclusions in quartz by deviatoric stress I: experimentally induced changes in inclusion shapes and microstructures, *Contributions to Mineralogy and Petrology*, *160*, 825–843, doi:10.1007/s00410-010-0509-z.

87. Tomé, C., H.-R. Wenk, G. Canova, and U.F. Knocks (1991), Simulations of texture development in calcite: comparison of polycrystal plasticity theories, *J. Geophys. Res.*, *96*, 11,865–11,876.

88. Tommasi, A., M. Knoll, Vauchez, A., J.W. Signorelli, C. Thoraval, and R. Logé (2009), Structural reactivation in plate tectonics controlled by olivine crystal anisotropy, *Nature Geoscience*, *2*, doi:10.1038/NGEO528.

89. Tullis, J., J.M. Christie, and D.T. Griggs (1973), Microstructures and preferred orientations of experimentally deformed quartzites, *Geological Society of America Bulletin*, *84*(1), 297–314.

90. Tullis, J., and H.R. Wenk (1994), Effect of muscovite on the strength and lattice preferred orientations of experimentally deformed quartz aggregates, *Mat. Sci. Eng.*, *A175*, 209–220.

91. Tullis, J., and R.A. Yund (1982), Grain growth kinetics of quartz and calcite aggregates, *Journal of Geology*, *90*, 301–318.

92. Twiss, R. (1977), Theory and applicability of a recrystallized grain size paleopiezometer, *Pure Appl. Geophys.*, *115*, 227–244, doi:10.1007/BF01637105.

93. Urai, J. L., W.D. Means, and G.S. Lister (1986), Dynamic recrystallization of minerals, *Geophysical Monograph Series*, *36*, 161–199.

94. Wagner, F., H.-R. Wenk, H. Kern, P. Van Houtte, and C. Esling (1982), Development of preferred orientation in plane strain deformed limestone. Experiment and theory, *Contrib. Mineral. Petrol.*, *80*, 132–139.

95. Warren, J.M. and G. Hirth (2006), Grain size sensitive deformation mechanisms in naturally deformed peridotites, *Earth and Planetary Science*, *248*, 438–450.

96. Wenk, H.R., K. Bennett, G.R. Canova, and A. Molinari (1991), Modelling plastic deformation of peridotite with the Self-Consistent Theory, *J. Geophys. Res.*, *96,* 8337–8349.

97. Wenk, H.R., G. Canova, Y. Bréchet, and L. Flandin (1997), A deformation-based model for recrystallization of anisotropic materials, *Acta. mater.*, *45*(8), 3283–3296.

98. Wenk, H.-R., G. Canova, A. Molinari, and H. Mecking (1989a), Texture development in halite: Comparison of Taylor model and self consistent theory, *Acta. Metall.*, *37*, 2017–2029.

99. Wenk, H.-R., G. Canova, A. Molinari, and U. F. Kocks (1989b), Viscoplastic modeling of texture development in quartzite, *J. Geophys. Res.*, *94*, 17,895–17,906.

100. Wenk, H.R., and C.N. Tomé (1999), Modeling dynamic recrystallization of olivine aggregates deformed in simple shear, *J. Geophys. Res.*, *104*, 25,513–25,527.

101. White, S.H., S.E. Burrows, J. Carreras, and F.J. Humphreys (1980), On mylonites in ductile shear zones, *J. Struct. Geo.*, *2*, 175–187.

Appendix A: Review and description of experimental procedures

Introduction

This appendix describes the Griggs apparatus, the experimental setup, and the experimental procedure conducted for this thesis. All the experiments were conducted in the rock deformation laboratory at the University of Tromsø in Norway. All of the experiments were conducted on Rig1 and all the mechanical data for each experiment was recorded digitally as well as physically through a paper chart record.

The Griggs apparatus

A modified Griggs-type solid medium deformation apparatus, Rig1, was used in this study (Figure 2.1). The apparatus comprises of a steel frame with three main platens (upper, middle, and lower), which are connected by two vertically parallel steel bars. A rotary motor and a gear box rest on top of the upper platen while the load cell is located and connect to the middle platen. A Saginaw bearing connects the gearbox to the load cell, which is connected to the hydraulic ram and driving pistons that run from the bottom of the load cell through the middle platen and stop approximately half way between the middle and lower platens. *Copper* pipes run through the housing of the hydraulic ram to cool the oil during use and reduce any pressure variations from daily temperature changes. The confining pressure, during use, is calculated using an external pressure transducer, which records and measures the oil pressure from within the hydraulic ram. The apparatus produces pressure by lowering the hydraulic ram downward against the steel σ_3 piston which applies a force on the sample assembly. A hand lever or a motorized linear drive and hydraulic cylinder can be used to lower or raise the hydraulic ram, increasing or decreasing the pressure respectively. An external load cell is used to measure the force on the sample. The load cell is attached to the gear train by a Saginaw bearing. The gear train allows a range of up to six orders of magnitude in displacement rate, driven by a servomotor used with a potentiometer control. The driving ram, located at the center of the hydraulic ram, applies a force against the tungsten carbide σ_1 piston, which is aligned with the jacketed sample and applies the force to the sample. To reach the sample the σ_1 piston will push through the Pb piece and come in contact with the upper alumina piston, applying a direct force to the sample material. Due to the significant amount of moving parts on the rig, there are frictional forces that are apparent and recorded during each experiment and cannot be avoided.

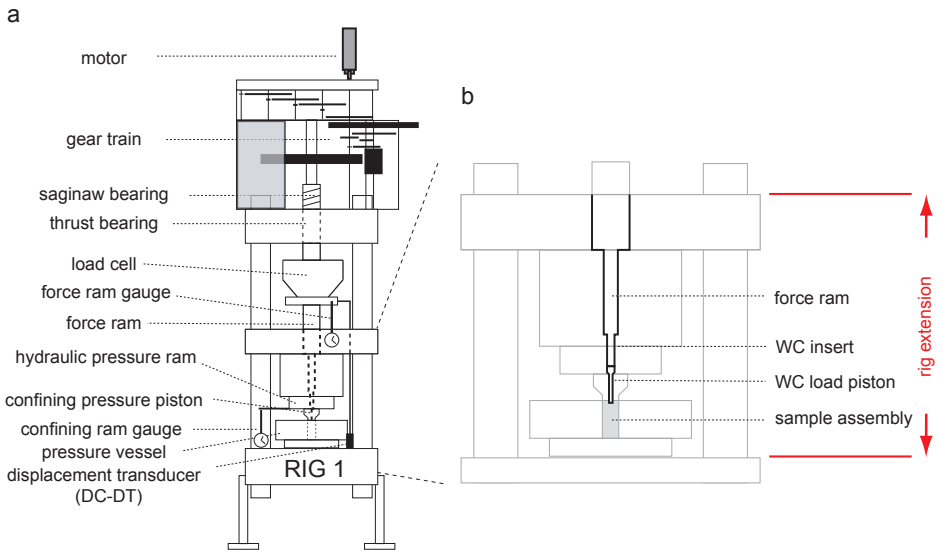

Figure A1. a) Schematic diagram of Rig 1 at the University of Tromsø b) illustrating rig extension during experiment (Figure modified after Pec et al. 2012).

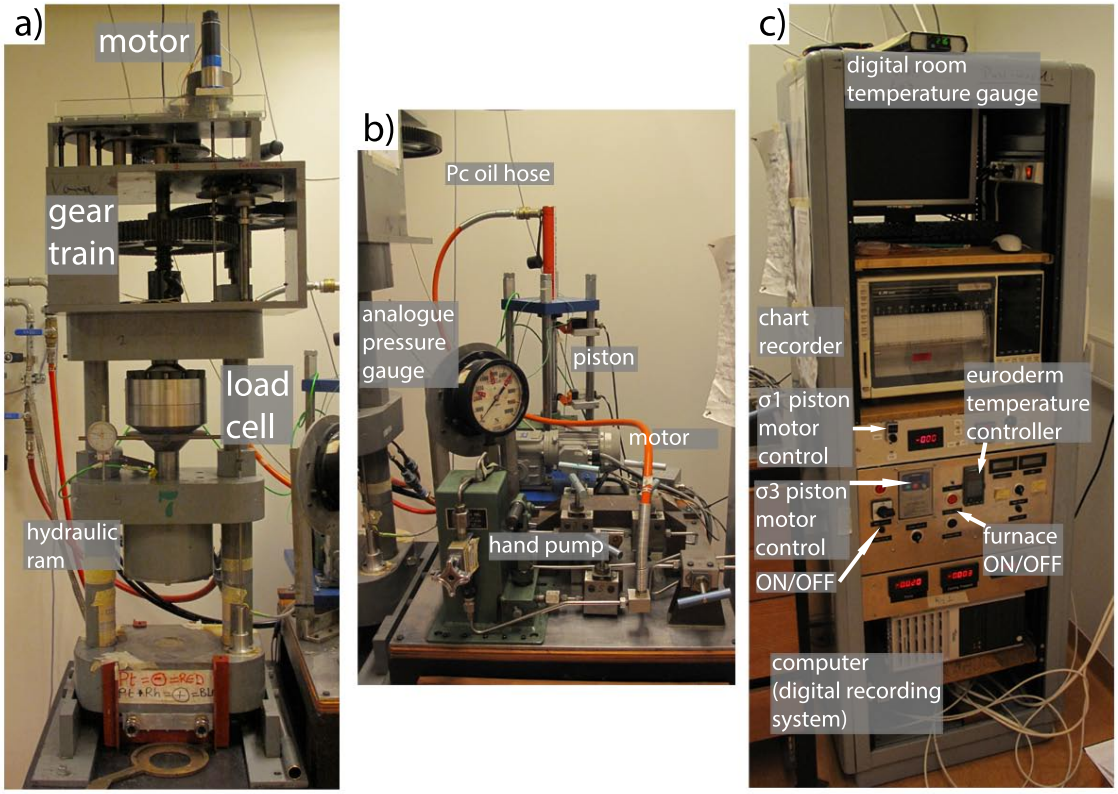

Figure A2. a) modified Griggs deformation apparatus b) automated pumping system c) record center and data storage.

Pressure Vessels, base plate, and cooling ring

Two different models of pressure vessels (PV) were use in these experiments, an internally cooled PV manufactured by STRECON named “Hercules” and a strip-wound container also manufactured by STRECON. Both PVs have a 1-inch (25.4 mm) diameter bore centrally located within the pre-pressed tungsten carbide (WC) core. All PVs rest

on top of a base plate, which consists of a central steel core, which is covered by a Teflon ring. The steel core has a hole running through it for the thermocouple to be inserted. On the top side of the steel ring is a circular recess ~1mm deep for the WC base plug and on the bottom side there is a linear recess running across the diameter of the ring ~4mm deep which allows the thermocouple to be bent and safely protruded out the side of the PV-base plate assembly, figure 2.5. A copper rod is attached to the steel disc, which is where an electrical cable is attached providing current to the system. Water-cooling copper pipes are also run through the base plate. Copper and/or Nickel sheets were placed in the circular recess to prevent any chemical etching from occurring during the experiments while at elevated temperatures and pressures.

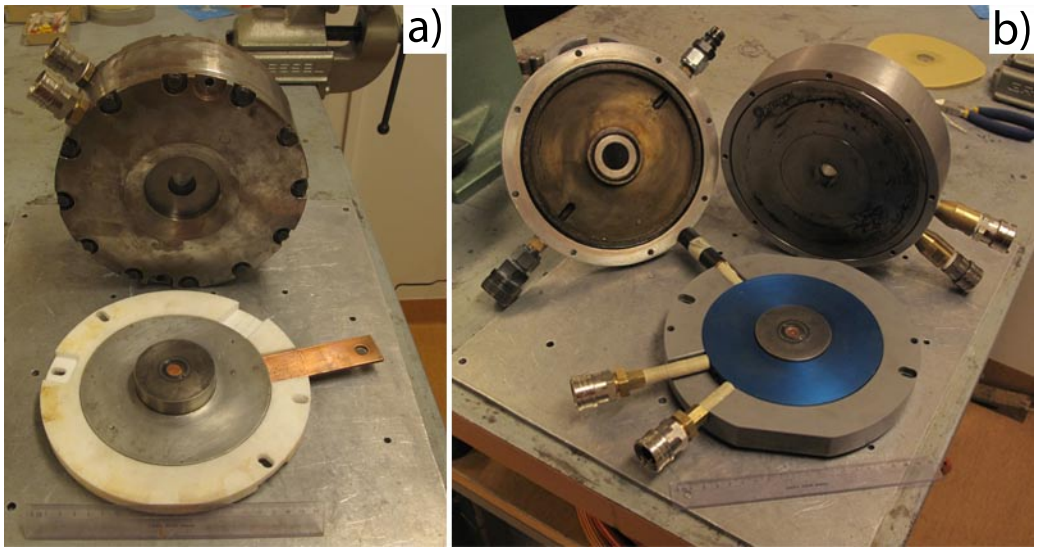

Figure A3 a) Hercules Pressure vessel and base plate b)Strecon strip-wound Pressure vessel (top right), cooling ring (top left) and the base plate (bottom).

A cooling ring is also placed on top of the PVs to reduce the temperature gradient of the assembly. The cooling ring on the Hercules model did not have to be removed after every experiment but it should be cleaned regularly to reduce wear on the rubber O-rings. The cooling ring for the strip-wound PV was removed and cleaned before and after each experiment. It is fastened to the PV with 8 screws to ensure no water would escape.

When assembling the PV and base plate a paper disc is placed in between to prohibit any contact due to flowing current through the system.

Sample preparation

Sample material

Professors Greg Hirth and Jan Tullis from Brown University provided the sample material used in these experiments. Black Hills Quartzite was provided ground up with a grain size range from ~40-220μm and sieved to various grain sizes of <40, 40-63, 63-100, 100-220, 220< μm. The only fraction used in the experiments was the grain sizes within the 63-100μm range. Black Hills Muscovite was provided ground to several centimeters in diameter along the basal-plane orientation. The combination of a coffee-bean grinder and ceramic mortar and pestle were used to further grind down the muscovite. The muscovite was then sieved to the various grain sizes of <45, 45-63, 63-125μm where the 45 -63μm grain size range was used in all experiments. All sample material is kept in glass vials at room temperature in a dark lab drawer.

Sample mixing

To insure homogenous distribution of both the quartz and muscovite in powder form, a mixing method was used to prevent clumping of muscovite and disaggregation of the two powders. Quartz and muscovite powders were placed in a 10ml glass beaker and held in an ultrasonic bath filled with water. Place enough acetone in the glass beaker to create a slurry with the powders and stir the slurry while the base of the glass beaker is submerged within the water of the ultrasonic bath. Continue to stir until the acetone has completely evaporated and no clumps remain within the sample. Repeat this process two to three times and then place in a glass vile for storage. This procedure is based on a similar method used by De Ronde 2005.

Shear pistons

To make shear pistons, a right cylinder is cut from a prefabricated rod of alumina with a diameter of 6.33cm. Once the cylinder is cut, both ends are polished and then a 45° cut is made approximately halfway between the cylinder. Typically a lip is left on one of the shear pistons. This lip can be removed by holding the shear piston against the water saw blade manually while using your finger to apply slight pressure from the other side of the blade to prevent any bending of the saw blade. If there is a slight difference in the size of the shear pistons, always use the taller shear piston as the bottom piston.

Jacketing the sample

A Pt jacket is used to incase the shear pistons and sample material for the duration of the experiment. The jacket is ~20mm in length and is cut from a prefabricated supplier with a wall thickness of 15mm. Once cut, both ends of the jacket are filed until flat and then the jacket is annealed in a ceramic furnace at 900°C for ~1 hour. Once annealed one end of the jacket is welded shut with a Pt cup. Ni foil with dimensions of 17 x 21mm is cut and inserted into the jacket. Place one shear piston into the jacket and use a pusher piece to insure the piston is resting against the Pt cup. Carefully pour the weighed sample material into the jacket and then place the top shear piston into the jacket. To make sure that the two shear pistons are aligned, three marks are made on both the jacket and the top shear piston. If water is added to the sample, use the syringe to carefully place the water on the top or side of the top shear piston. Finally, weld the top cup to the jacket and the mark with a scalpel and permanent marker the orientation of strike, the up direction, and where the thermocouple should be placed.

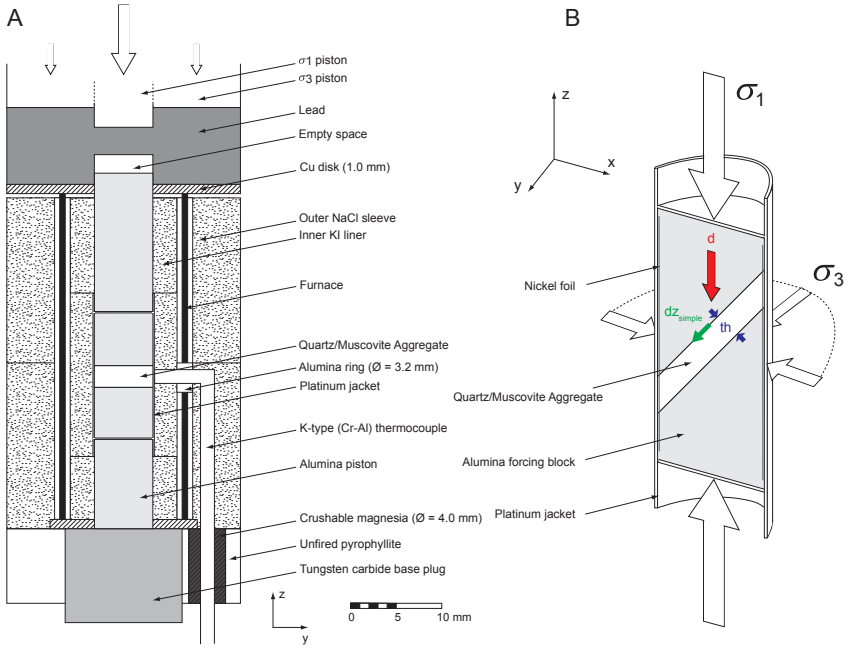

Figure A4. Drawing of the sample assembly and the shear geometry used in this study. a) Assembly inside of the pressure vessel in the y–z section. b) Geometry of the sample assembly for general shear experiments. (Figure modified after Tarantola et al. 2010).

Sample assembly

To construct the sample assembly (figure 2.3), two outer salt pieces are used as the confining medium with the height of the lower salt piece measured to the point where the thermocouple comes in contact with the proposed sample position located within the Pt jacket. A small gouge can be made where the thermocouple is bent in the salt

piece to avoid any unnecessary pressure against the neck of the thermocouple during assembly or pressurization. The outer salt cells encapsulate the furnace as well as three inner salt pieces and the Pt jacket. A hole is drilled in the central inner salt piece as well as the furnace to allow the thermocouple to be as close as possible to the sample material. Two alumina pistons are attached to the top and bottom of the Pt jacket; each cut and polished to a specific height to position the sample material and thermocouple accurately. The furnace comprises three cylindrical pieces, the inner and outer pieces are __ cm in height and are soft-fired pyropholite and the middle cylinder is __ cm in height and is composed of graphite. The slower salt piece possesses a 1 cm recess where a Cu disc is inserted and on top of the furnace and

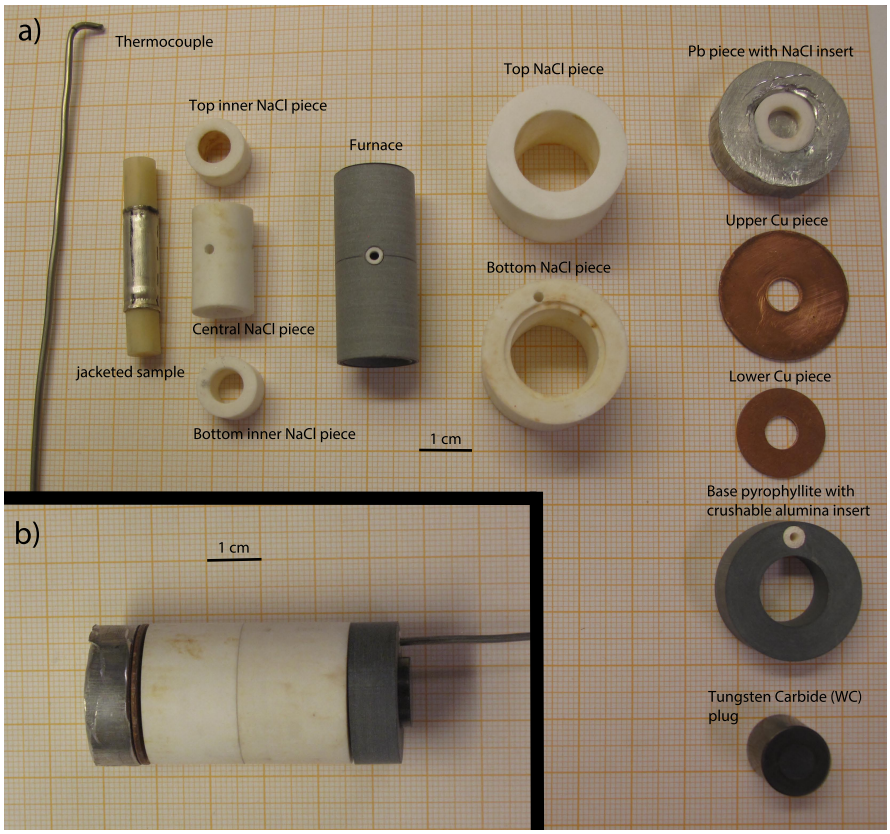

Figure A5. a) All of the different pieces used in a single Griggs experiment for this study, b) pieces assembled.

Rig Preparation

Base Plate and Pressure Vessel

Once the sample has been assembled, it is placed on top of the central steel disc of the base plate and a cardboard disc is placed around the sample covering all metal surfaces (figure 2.5a). The pressure vessel is then fitted over the sample assembly, carefully, not tearing or removing any Teflon tape surrounding the outer salt pieces. Once the pressure vessel is fit over the sample assemble and rests on the central steel disc of the

base plate connect the pressure vessel to the base plate with two screws, finger tight and remove the assemble from the arbor press and flip upside-down resting on a cylindrical stage. Here masking tape is applied to both the steel plate as well as the thermocouple to avoid contact between electrically flowing surfaces (figure 2.5c). Glue is applied to prevent the two thermocouple wires from coming in contact and the wires are attached to the K-type thermocouple connector. A final piece of tape is put over the thermocouple securing it to the base plate.

Experimental procedure

PV + Base plate into Rig

To insert the pressure vessel and base plate configuration into the deformation rig the sigma-1 and sigma-3 pistons are sufficiently backed off. A thermo-paper disc is placed in the recess on the lower platen to insure no contact between the platen and the base plate's steel disc. The pressure vessel and base plate configuration can be either set in through the front or the back side of the rig and is dependent on which configuration is being used, for details see appendix A.

Once the PV is fitted into the rig, lower the confining pressure piston (CP piston) and the driving piston until the CP piston lies ~1-2mm above the top of the driving piston and then line up the driving piston with the σ_1 piston (figure __). When they are aligned, lower the CP piston until it comes into contact with the sigma-3 piston, then give two-three more pumps and then lower the sigma-1 piston until the force recorder noticeably increases. Finally, loosen the connecting screws between the pressure vessel and base plate.

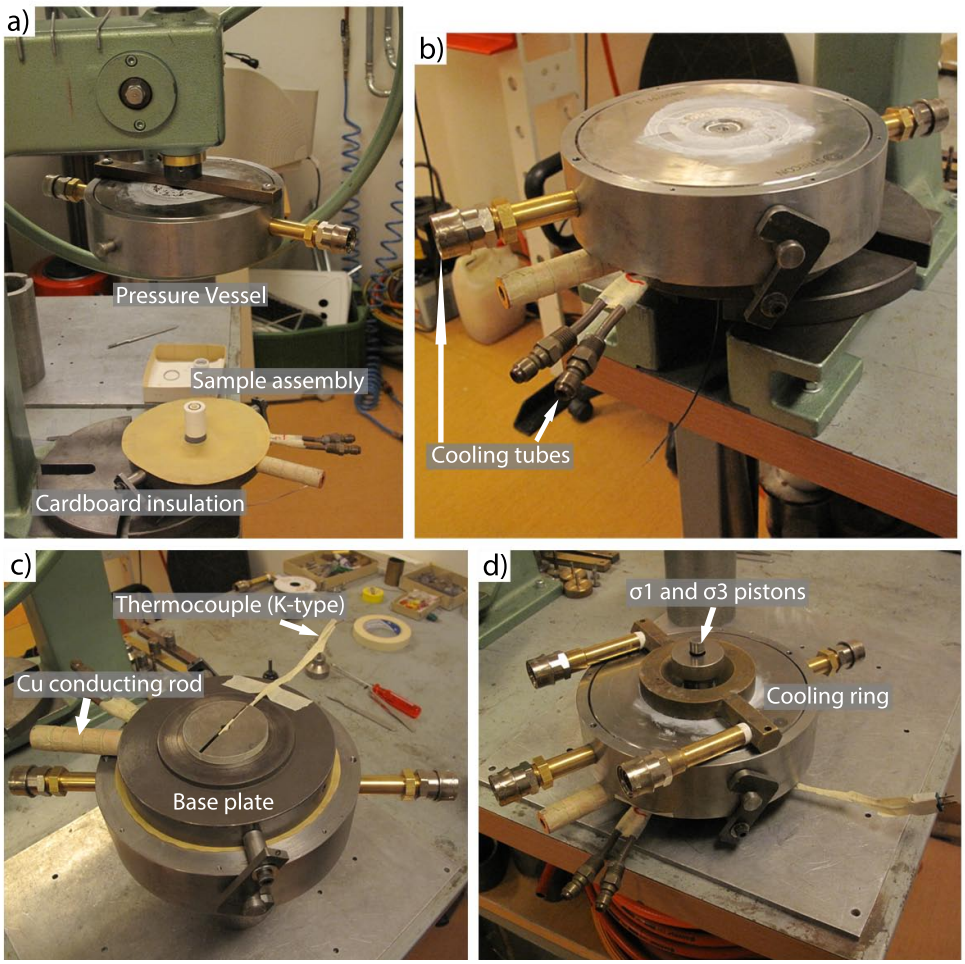

Figure A6. a) loading the pressure vessel over the sample assembly, b) top view of the pressure vessel and the base plate, c) bottom view of the pressure vessel and base plate, d) cooling ring and σ_3 piston placed on top of the pressure vessel.

Cooling system

To construct the cooling system, attach the various water hoses to the water source, PV, base plate, and rig. Double check to make sure water flow continuously flows in one direction. To test the water system, detach the outflow connection against the wall and place the nozzle in a bucket and turn the water flow latch to ON and turn the power on for the rig and the water should flow through the cooling system and exit into the bucket. Once water has been flowing into the bucket, turn the power off and reattach the nozzle to the proper connection. Finally, connect the thermocouple to the rig and turn the power back on. The temperature, if the TC is working properly, should read room temperature (22-25°) and then after several minutes the temperature should drop to the temperature of the water traveling through the cooling system, typically 14-16°C. Once this point is reached, the chart record and digital record can be set up and then begin pressurization.

Setup of Chart Record

To set up the chart recorder for rig1, check to make sure there is sufficient paper to record the entire experiment. The chart record uses four different recording devices, each recording a different parameter and represented as a different color on the chart record. Force is red, green is confining, blue is displacement, and black is temperature. Each record has a specific voltage bandwidth range, i.e. force has a voltage bandwidth of two volts. These bandwidths are selected based on the predicted values, parameters, design of the experiment. The bandwidths used in all of my experiments were set to: force: 2V, confining pressure: 5V, displacement: 0.5V, and temperature: 5V. Two different chart speeds are typically used, one for pressurizing and quenching and the other for during the experiment time frame. The chart speed used during pressurizing and quenching is 120mm/hr while the chart speed during the experimental time frame is 10mm/hr. Finally, one needs to write down all the starting conditions of the experiment at the bottom of the chart, such as: sample number, date, time, rig#, sample material, recorder bandwidths, chart speed, initial values of recorders, water temperature, as well as any additional comments.

To setup the digital recording system located on the computer one needs to open a LabView file. This file records all the data that is also being recorded on the chart record but digitally. Typically, the LabView file does not need to be tampered with and the only values that need to be changed is the "measurement per second" recorded value from 0.5 (standard setting) to 1.0 measurements per second recorded. The final step is to save the file with the experimental run number, e.i. 391LT. Hit "Run" to start recording and on the chart recorder, hit the button "pen lift" to drop the pen recorders in contact with the paper. Now the experimental parameters are being recorded.

Pressurization

To pressurize the experiment to the desired pressure and temperature slowly pump up the pressure, by use of the hand pump, until ~25-50 MPa where an audible cracking sound can be heard. This noise is the cracking of the furnace under the compression of the upper Cu-piece and indicates there is full contact between the Cu-discs and the furnace. Continue pumping by use of the hand pump at a fairly slow rate and while using the hand pump manually lower the driving piston down until the force record noticeably increases. Repeat approximately every 1-2 minutes until the driving piston moves

independent of the CP piston. When the driving piston begins to move independently of the CP piston, close value 5 and stop using the hand pump. For the remainder of pressurization, two servo-controlled motors are used to lower both the CP and driving pistons.

The exact position of the sample in relation to the driving piston is not discretely known and to get around this problem the CP piston is driven down 0.3mm and then stopped and then the driving piston is driven down 0.2mm and then this cycle repeats itself until the ideal pressure is reached. This prevents the driving piston from moving at a faster rate than the CP piston.

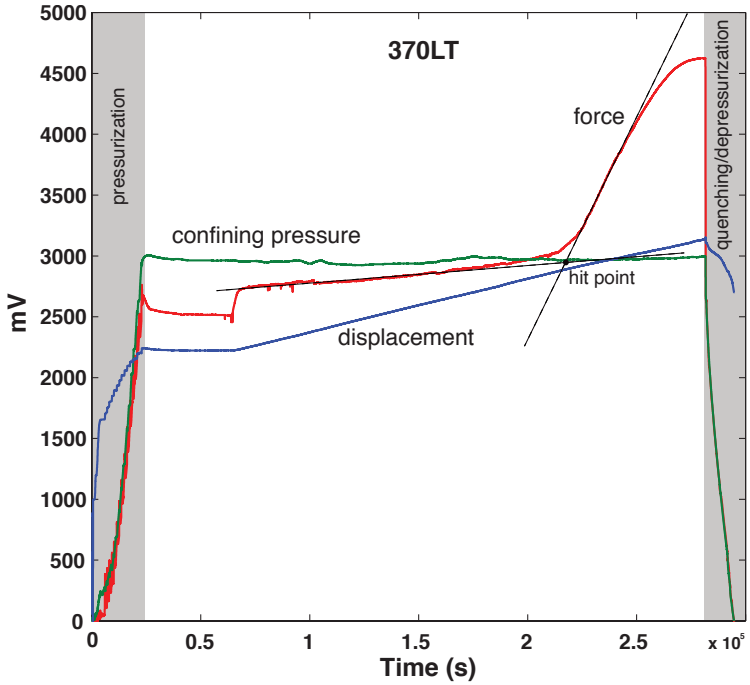

Figure A7. Raw mechanical data for the entire experiment 370LT with time vs. mV.

Deformation

Once the desired pressure and temperature conditions are reached, the driving motor is advanced at a specific displacement rate. The force record will then sharply increase and level out. This leveling feature is the driving piston reaching a yield point within the Pb piece of the sample assembly (figure 2.6). The force record will then slowly increase over time until the force record again increases. This increase is associated with the contact of the driving piston with the alumina piston. A discrete value cannot be pinpointed in the force record but an approximation is made by the intersection of two linear lines. The first line is matched to the "run-in" curve and the second line is fitted to

the elastic slope. The intersection of these two lines is defined as the hit point of the experiment. Once the hit point is reached the material can go through various phases. Typically the first phase of deformation is the elastic deformation where there is an increase in the force record but if the force applied to the sample was released the stress on the material would drop back down to its original value, ideally time independent. This region is defined by a linear increase of force vs. displacement. When the force applied to the sample exceeds the elastic properties of the sample material it transitions into either a work hardening or a work softening "recovery" phase of deformation. This transition point is regarded as the yield point of the material.

If the sample material transitions through the yield point and the stress on the material continue to increase, this is called work hardening. At a certain point the material will then either fail instantaneous through brittle processes or will weaken due to recovery mechanisms, which is documented by a decrease in the force on the sample. The point where the material transitions from work hardening to work softening is referred to as the peak strength of the material. Finally, a stable regime is reached where work hardening and softening mechanisms balance out and rough linear force vs. time curve is recorded.

Quenching and depressurization

When the experiment is completed it needs to be quenched to perverse the microstructures within the sample. This is done by rapidly lowering the temperature to 200°C, typically at a rate of 4-5°C/s. This will cause a drop in the confining pressure. To avoid any decompression cracking, turn the driving piston motor in the up direction and turn on when necessary to make sure that the force, controlled by the driving piston motor, is 200-300 MPa higher than the confining pressure. Once the rig has leveled out at 200°C, slowly retract the CP piston. During this time the driving piston is also retracted, reducing the force. In keeping with an ~200-300 MPa difference it is easier to manage the driving piston motor than the CP motor, so checking the chart record every few minutes is advantageous to avoid any decompression cracking. Once the confining pressure has reached ~300-400 MPa the difference between the force and confining pressure should be ~150-200 MPa and this difference should slowly decrease until it is ~100 MPa when the confining pressure is ~100 – 150 MPa. When the confining pressure reaches ~400-500 MPa the temperature is reduced from 200 to 100°C and

then finally when the confining pressure is reduced to ~100 – 150 MPa it is reduced from 100 to 30°C. Once the confining pressure reaches zero, use the wrench to manually back the remaining force off with the driving piston. At this point there should be no confining pressure or force on the sample and it has been quenched and depressurized.

Sample recovery

To remove the sample assembly from the pressure vessel the sigma-1 and sigma-3 pistons need to be removed. Typically this can be done by hand but sometimes a cloth and wrench need to be used and in extreme cased the vice is used. Once removed flip the PV and base plate up side down and cut off the remaining TC wire and remove the base plate. The hydraulic press is used to push out the sample assembly with a Pb spacer in between a steel pusher piece and the sample assembly. Before dissecting the sample assembly both the pressure vessel and base plate need to be cleaned. Remove the tape and sand down any excess material.

Once the base plate and PV are cleaned and stored, the sample assembly can be dissected. Using a scalpel, remove the upper Cu and Pb-piece. Then carefully remove the outer and inner salt medium as well as the furnace while always remembering which direction is up. When all the material has been removed mark the point where the TC placement with a marker. It is also useful to look at the TC under a light microscope if there were any problems during the experimental run. Once the jacketed sample is recovered, mark the up direction and store in a small plastic container. All excess material can then be thrown away except the Pb-piece is recycled, both the both and top Cu-pieces, and the WC plug.

Appendix B: Extra data

Introduction to Appendix B

This appendix will present data that is mentioned or used to construct valuable results used throughout chapters 2 and 3 in this thesis. Pole figures were presented based on CIP the construction of CIP maps for just the original grains that do not recrystallize completely throughout deformation and CIP maps for just the recrystallized grains. Next, are the Grain boundary maps used to construct the SPO data presented in chapter 2. Finally, grain size measurements are listed for models 1, 2 in chapter 3 of this thesis. Images may be reduced in size to reduce the number of pages taken up in the thesis.

CIP maps for just the original and recrystallized grains

100% Quartz (masked original grains – masked recrystallized grains)

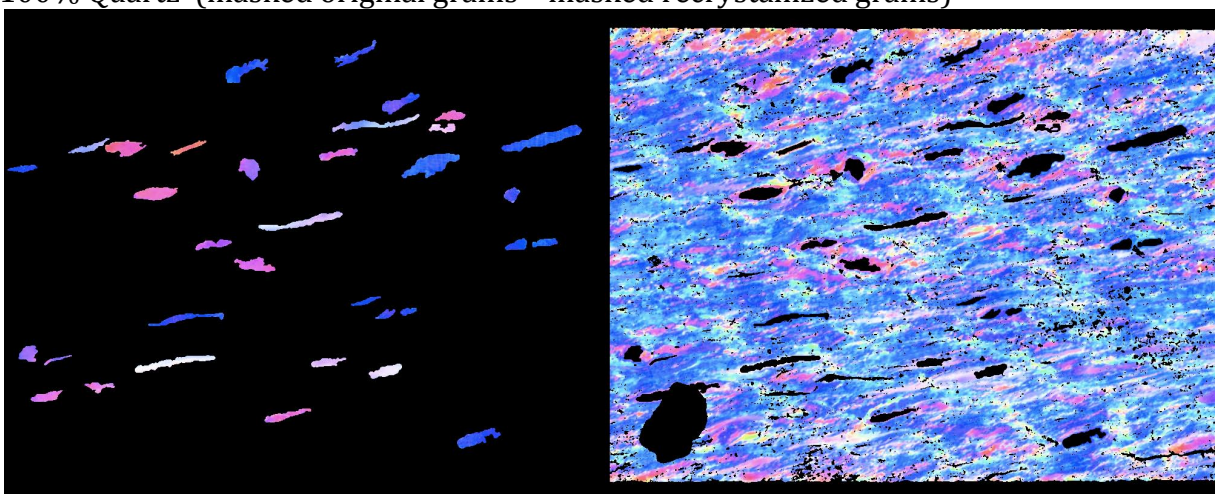

5% Muscovite 95% Quartz (masked O.G. – masked R.G.)

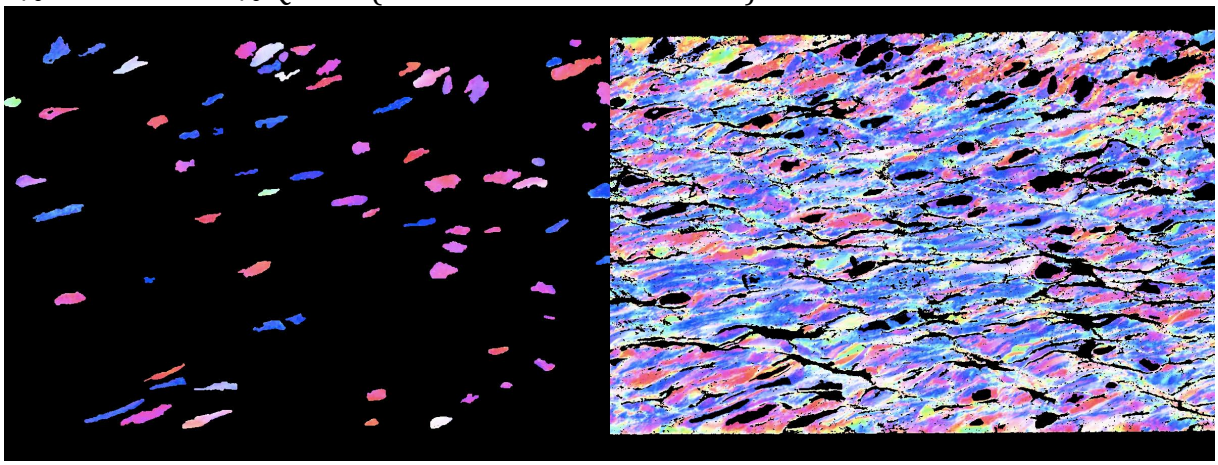

10% Muscovite 90% Quartz (masked O.G. – masked R.G.)
NOTE sinistral sense of shear

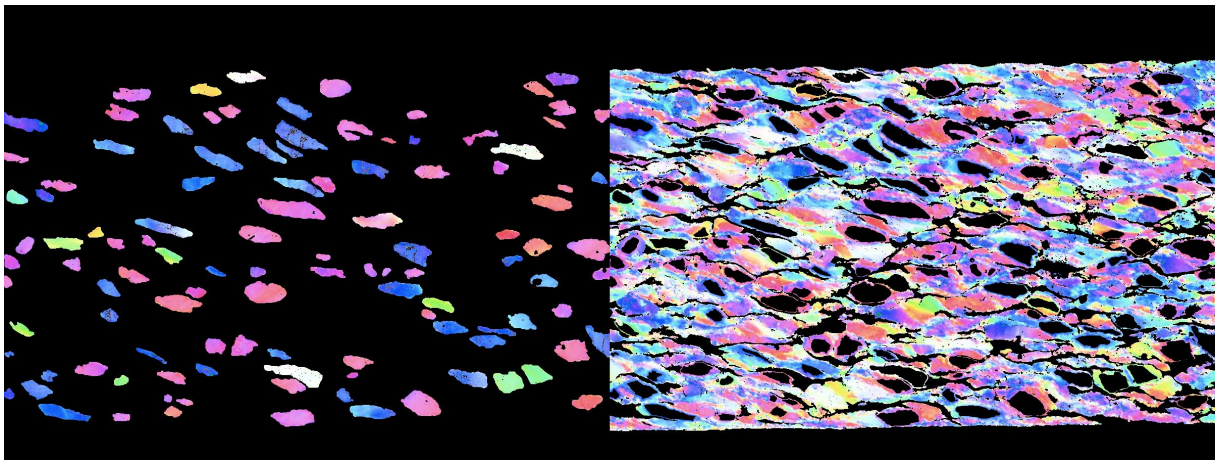

25% Muscovite 75% Quartz (masked O.G. – masked R.G.)

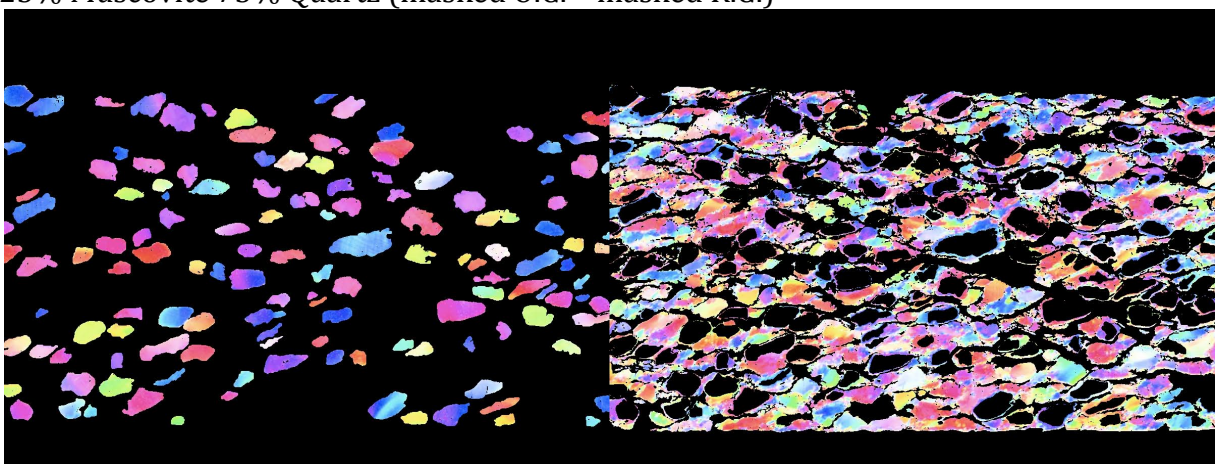

Grain boundary maps for shape preferred orientation data

100% Quartz (hydrostatic – peak stress – steady state)

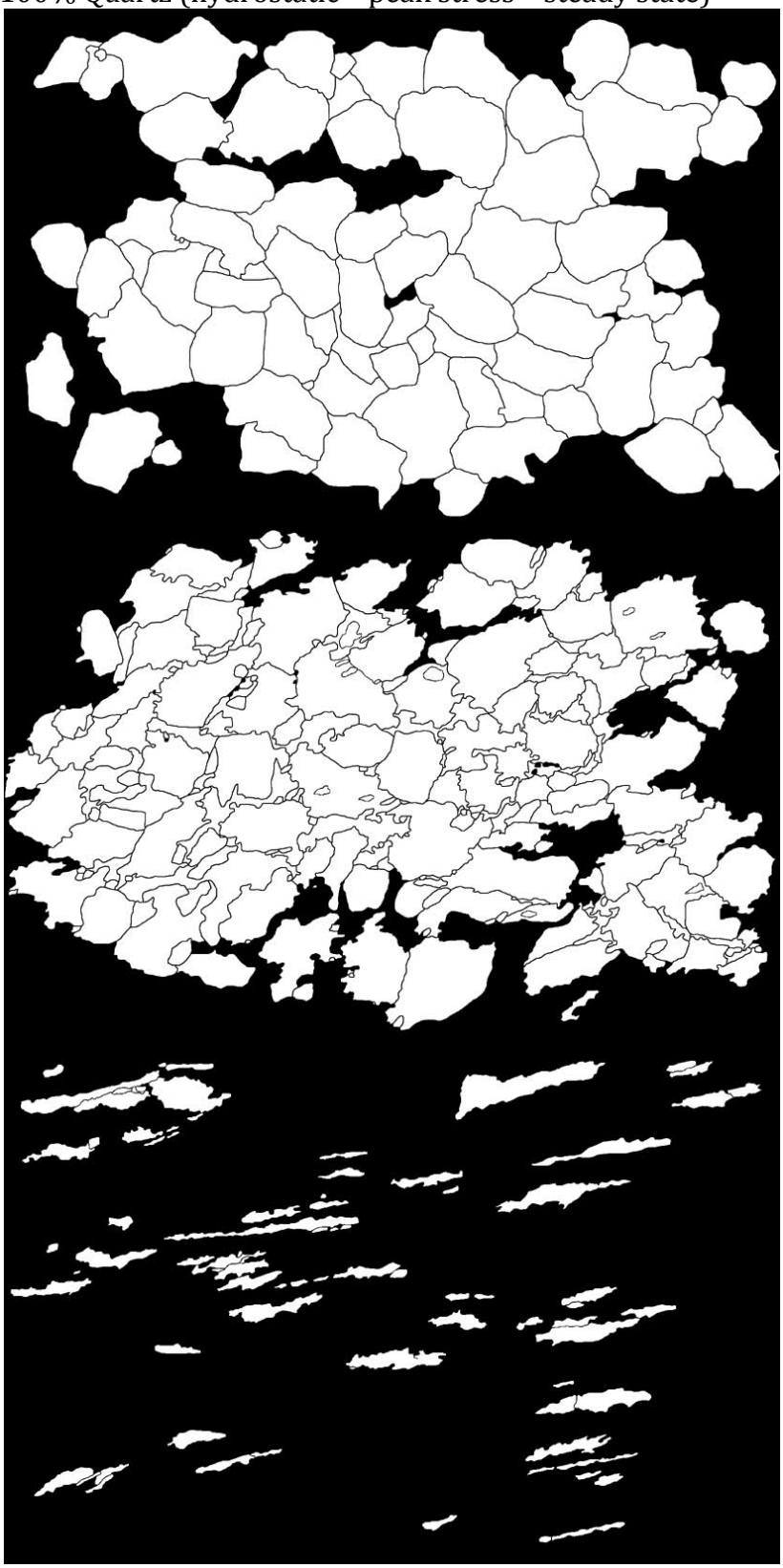

5%muscovite – 95%quartz (hydrostatic – peak stress – steady state)

10%muscovite – 90%quartz (hydrostatic – peak stress – steady state)

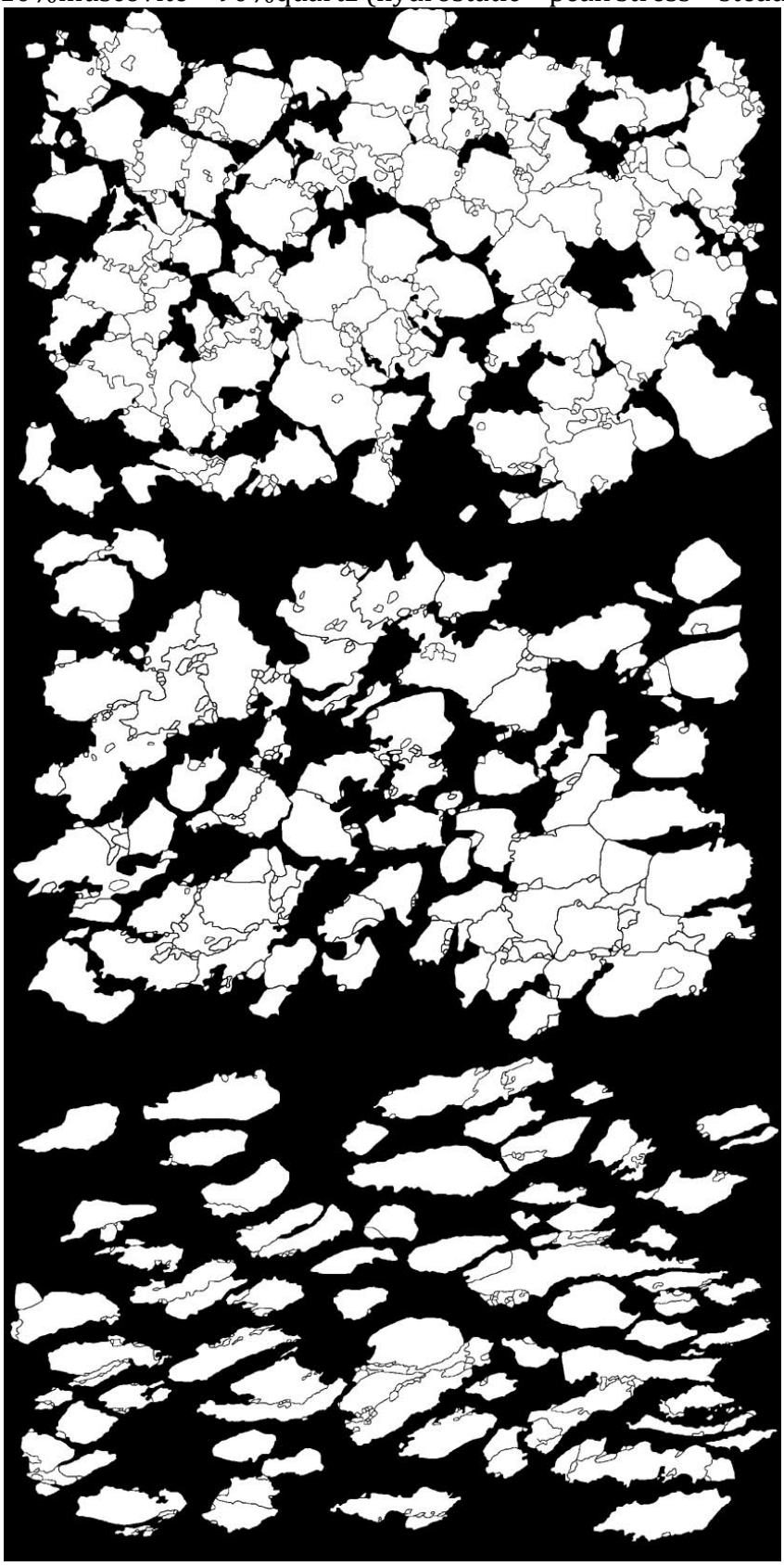

25%muscovite – 75%quartz (hydrostatic – peak stress – steady state)

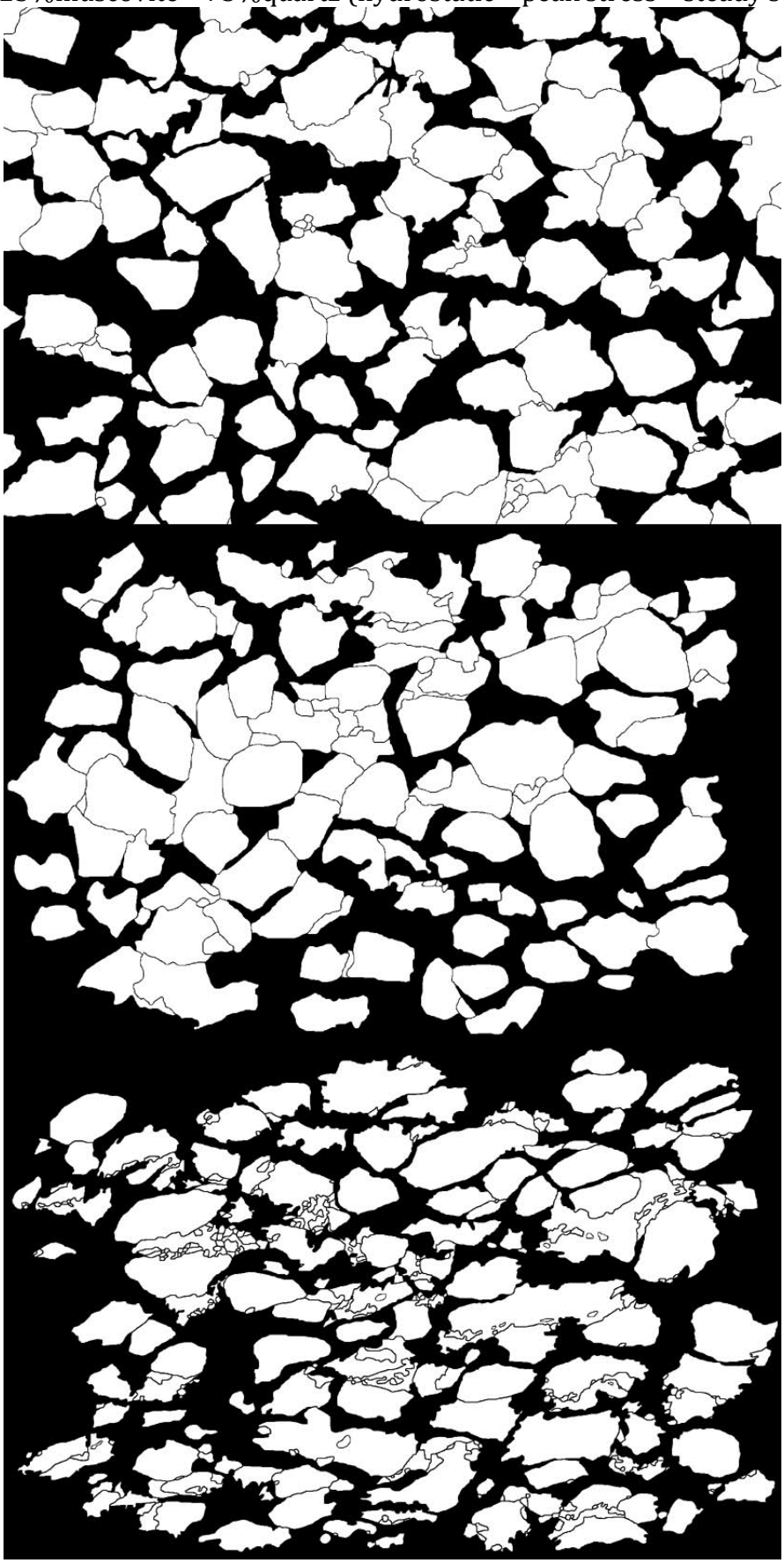

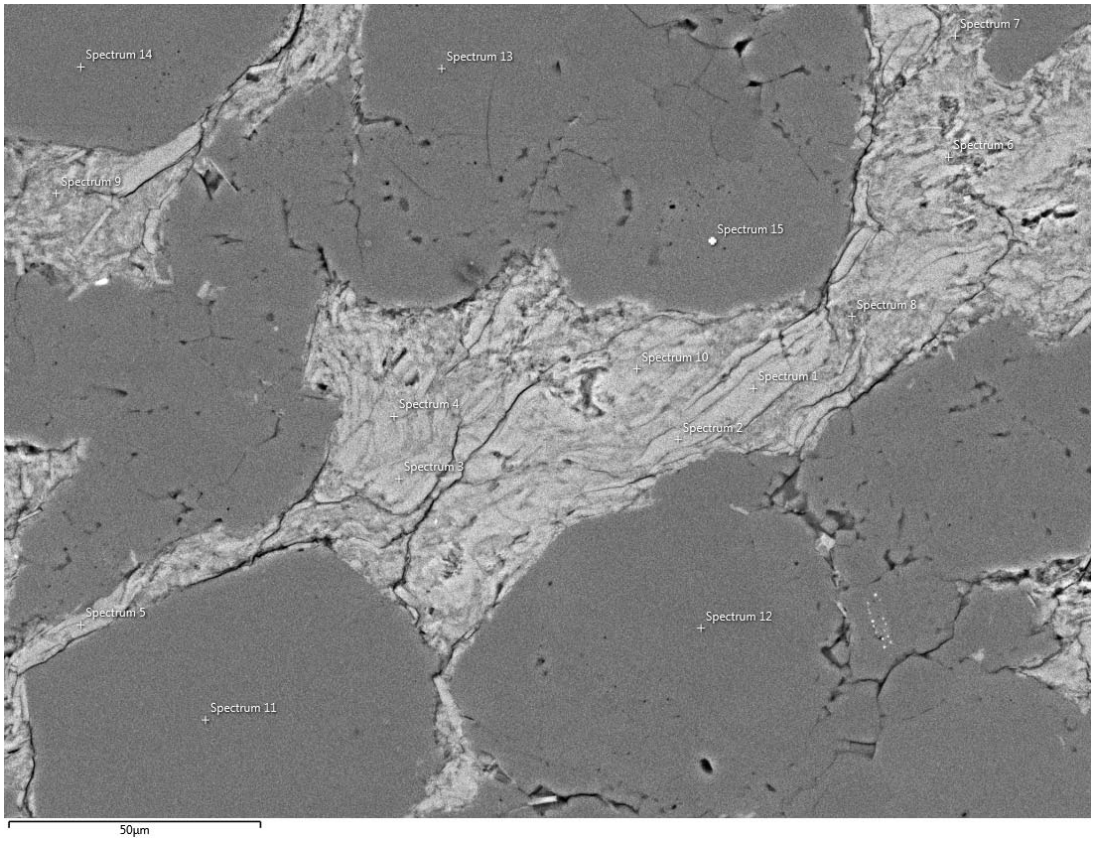

Figure B1. Electron back-scatter image of Quartz and muscovite. Quartz is defined by the dark grey material and muscovite is defined by the light grey material. Spectrum analyses from 1-10 represent muscovite and 11-15 represent quartz.

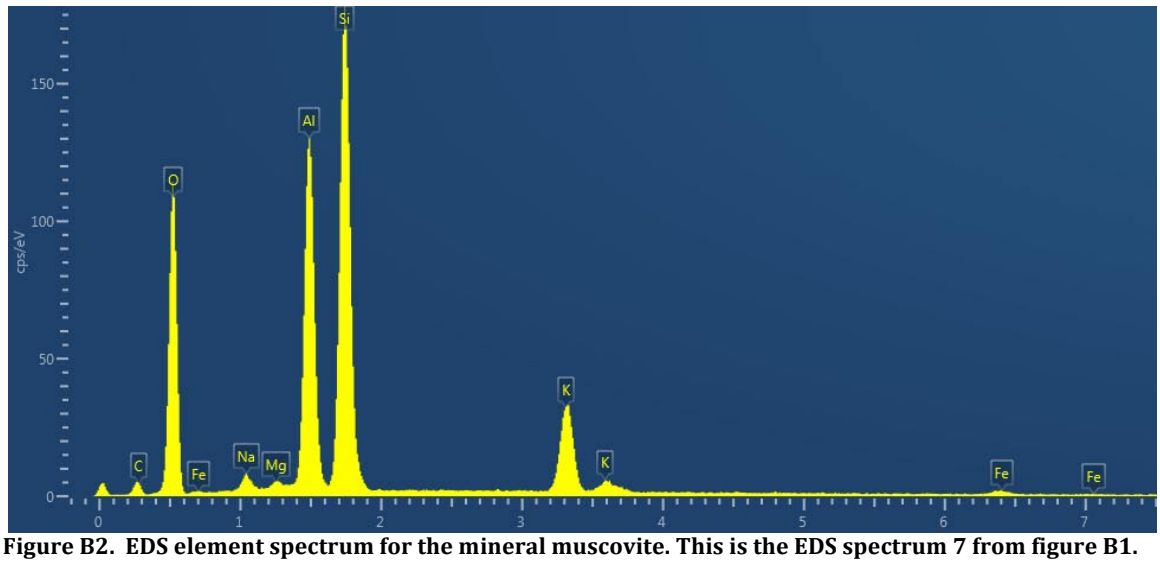

Figure B2. EDS element spectrum for the mineral muscovite. This is the EDS spectrum 7 from figure B1.

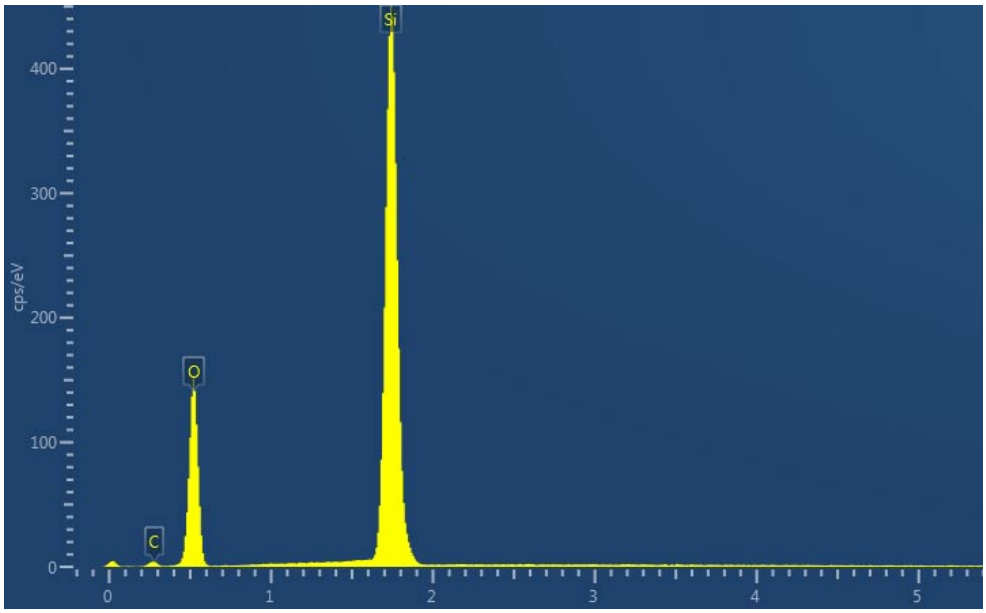

Figure 3. EDS element spectrum for the mineral quartz. This is the EDS spectrum 11 from figure B1.

Table B1 *Geochemical data for muscovite and quartz from EDS measurements*

	O	Na	Mg	Al	Si	K	Fe	Ta
Spectrum 1	45.78	0.46	0.30	19.42	22.55	10.24	1.25	-
Spectrum 2	45.75	0.45	0.33	19.58	22.37	10.21	1.32	-
Spectrum 3	45.83	0.57	0.39	19.63	22.40	9.96	1.23	-
Spectrum 4	46.06	0.60	0.33	19.17	23.06	9.59	1.19	-
Spectrum 5	47.94	0.47	0.31	13.71	29.54	7.09	0.94	-
Spectrum 6	46.22	0.70	0.31	18.71	23.62	9.40	1.05	-
Spectrum 7	47.23	1.04	0.34	16.49	26.49	7.52	0.89	-
Spectrum 8	46.27	0.78	0.35	17.94	24.22	9.49	0.96	-
Spectrum 9	46.44	0.95	0.27	17.76	24.56	8.85	1.17	-
Spectrum 10	45.73	0.63	0.28	19.44	22.45	10.26	1.19	-
Spectrum 11	53.15	-	-	-	46.85	-	-	-
Spectrum 12	51.15	-	-	-	43.92	-	-	4.87
Spectrum 13	53.24	-	-	-	46.71	-	0.03	-
Spectrum 14	53.25	-	0.02	-	46.73	-	-	-
Spectrum 15	51.44	-	0.02	0.10	44.23	-	0.06	4.14

Table B2 *Grain size measurements taken from the high, medium, and low zones for Model 1*

Low Strain Grain size (μm)	Med. Strain Grain size (μm)	High Strain Grain size (μm)
8.00	5.00	2.50
6.00	4.00	3.00
5.50	4.00	3.50
6.00	4.50	3.00
6.50	3.50	3.00
7.00	4.00	3.00
7.00	6.00	3.00
5.50	4.50	2.50
6.50	3.50	3.50
8.50	4.00	4.00
10.00	6.00	4.00
5.50	6.50	2.50
5.00	5.00	2.50
6.00	4.00	2.50
6.00	5.50	3.00
7.00	4.00	4.00
5.50	4.00	3.50
8.00	4.50	3.00
7.00	3.50	3.00
5.50	4.00	3.50
G_{ave}=6.60	G_{ave}=4.50	G_{ave}=3.13

Table B3 *Grain size measurements taken from the four different zones for Model 2*

Z1 Grain size (μm)	Z2 Grain size (μm)	Z3 Grain size (μm)	Z4 Grain size (μm)
8.00	7.00	6.00	4.00
9.00	10.00	5.00	3.00
8.00	6.00	7.00	3.50
6.00	7.00	6.00	2.00
9.00	6.00	5.00	2.50
6.00	8.00	6.50	3.00
11.00	9.00	6.50	4.00
11.00	7.00	5.00	5.00
9.00	6.00	6.00	3.50
11.00	6.00	6.00	3.50
8.00	6.00	8.00	3.00
8.00	8.00	6.00	2.50
14.00	7.00	8.00	4.00
6.00	6.00	6.00	4.50
7.00	6.50	6.00	3.50
6.00	8.00	4.00	2.50
6.00	5.50	5.00	4.00
8.00	9.00	7.00	3.00
7.00	7.00	6.00	4.50
6.00	7.00	5.00	3.50
G_{ave}=8.30	G_{ave}=7.10	G_{ave}=6.00	G_{ave}=3.45